Title: Novel quantal analysis method reveals conservation of average charge injected by excitatory synapses across cortical neurons of different sizes

Author Names and Affiliations: Martynas Dervinis[1], Guy Major[1]

[1]: Cardiff University, Cardiff, Wales, CF10 3AT, UK

Corresponding author email address: martynas.dervinis@gmail.com

Number of pages: 46

Number of figures: 9

Number of words

Abstract: 270

Body text excluding Materials and Methods: 3937

Conflict of interest statement: The authors declare no competing financial interests.

Acknowledgements: Cardiff University (GM, MD), The Medical Research Council of the UK (MD PhD). Neural activity simulations were performed on the Cardiff School of Biosciences' Biocomputing Hub HPC/Cloud infrastructure.

Abstract

In chemical synapses of the central nervous system (CNS), information is transmitted via the presynaptic release of a vesicle (or 'quantum') of neurotransmitter, which elicits a postsynaptic electrical response with an amplitude termed the 'quantal size'. This key determinant of neural computation is hard to measure reliably due to its small size and the multiple sources of noise within neurons and electrophysiological recordings. Measuring amplitudes of miniature postsynaptic currents (mPSCs) or potentials (mPSPs) at the cell soma is generally thought to offer a technically straightforward way to estimate quantal sizes, as each of these miniature responses (or 'minis') is generally thought to be elicited by the spontaneous release of a single neurotransmitter vesicle. However, a somatically recorded mini is typically massively attenuated compared with at its input site, and a significant fraction are indistinguishable from (or cancelled out by) background noise fluctuations. Here, as part of patch clamp data analysis software called 'minis', we describe a novel quantal analysis method that estimates the 'electrical size' of the synapse by combining somatic recordings of background physiological noise with and without minis with simulations. With the help of a genetic algorithm, simulations are successfully used to infer the combined amplitude and rise time distribution of minis that would otherwise be inaccessible due to low signal-to-noise ratios. The estimated distributions reveal a striking inverse dependence of mean minis' amplitudes on cell's total capacitance (proportional to cell size, more exactly, extracellular membrane surface area) that firmly supports the conservation of the average 'electrical size' (in terms of injected charge) of excitatory cortical synapses in rats, across neocortical pyramidal neurons of very different sizes.

45 # Abbreviations

46 ABF – Axon Binary File

47 aCSF – artificial cerebrospinal fluid

48 AMPA – α-amino-3-hydroxy-5-methyl-4-isoxazolepropionic acid

49 AMPAR – α-amino-3-hydroxy-5-methyl-4-isoxazolepropionic acid receptor

50 ANN – artificial neural network

51 AP – action potential

52 CPP – (*RS*)-3-(2-carboxypiperazin-4-yl)-propyl-1-phosphonic acid

53 EPSC – excitatory postsynaptic current

54 EPSP – excitatory postsynaptic potential

55 GA – genetic algorithm

56 GABA – gamma-aminobutyric acid

57 IC50 – Half-maximal inhibitory concentration

58 IPSC – inhibitory post-synaptic current

59 IPSP – inhibitory post-synaptic potential

60 MAD – maximal absolute deviation

61 mEPSC– miniature excitatory post-synaptic current

62 mEPSP– miniature excitatory post-synaptic potential

63 mIPSP– miniature inhibitory post-synaptic potential

64 mPSC – miniature post-synaptic current

65 mPSP – miniature post-synaptic potential

66 NBQX – 2,3-dioxo-6-nitro-1,2,3,4-tetrahydrobenzo[*f*]quinoxaline-7-sulfonamide

67 NMDA – N-methyl-D-aspartate

68 NMDAR - N-methyl-D-aspartate receptor

69 SAD – sum of absolute deviations

70 SD – standard deviation

71 smEPSP – simulated mEPSP

72 SSD – sum of signed deviations

73 SSE – sum of squared errors

74 TTX – tetrodotoxin

75 V_m – membrane potential

76

Introduction

Synaptic transmission in the CNS occurs in 'quanta' (Forti et al., 1997; Hardingham et al., 2010; Isaacson and Walmsley, 1995; Jonas et al., 1993; Kraszewski and Grantyn, 1992; Kullmann and Nicoll, 1992; Kuno, 1964; Larkman et al., 1991; Sahara and Takahashi, 2001; Stern et al., 1992; Wall and Usowicz, 1998) usually thought to correspond to the release of a single neurotransmitter vesicle (Heuser et al., 1979). The amplitude of the postsynaptic response to a quantum of transmitter, the quantal size, is a key parameter defining the efficacy of synaptic transmission (Katz, 1969; Vere-Jones, 1966) and, therefore, an important determinant of neural computation.

Quantal size measurements in the CNS are difficult due to multi-synaptic contacts, limited accessibility, significant quantal variance, temporal non-stationarity of synaptic properties, and low signal-to-noise ratios of somatic electrophysiological recordings of quantal events (Bekkers, 1994; Korn and Faber, 1991). For these reasons classical quantal analysis as done at the neuromuscular junction has run into problems in central synapses. More recent methods such as noise deconvolution, Variance-Mean analysis, and optical quantal analysis have not fared much better either (Biró et al., 2005; Clamann et al., 1991; Clements, 2003; Clements and Silver, 2000; Edwards et al., 1976; Enoki et al., 2009; Jack et al., 1981; Liu et al., 2022; Oertner et al., 2002; Peled and Isacoff, 2011; Redman, 1990; Reid and Clements, 1999; Silver, 2003; Yuste et al., 1999).

A complementary method of assessing synaptic function is to measure properties of mPSCs. Miniature PSC amplitude measurements are often taken as quantal size estimates across the population of active synapses onto a neuron, as the mPSC (under voltage clamp) or mPSP (under voltage recording) likely correspond to the response to a spontaneous release of a single neurotransmitter vesicle (Brown et al., 1979; del Castillo and Katz, 1954; Fatt and Katz, 1952; Isaacson and Walmsley, 1995; Wall and Usowicz, 1998). Measurements of mPSC amplitudes are

102 routine in the literature. However, they are likely overestimates due to small amplitude events being
103 difficult to detect and largely being missed.
104
105 The use of voltage clamp can be a major reason why mPSCs “go missing”. Theoretical studies (Major,
106 1993a; Rall and Segev, 1985; Spruston et al., 1993) predicted and experimental findings (Williams
107 and Mitchell, 2008) confirmed that voltage clamp fails to clamp extended dendrites, and to capture
108 the current flowing in at electrically remote synapses. Amplitude attenuation can also be caused if
109 series resistance is not compensated (Williams and Mitchell, 2008). These issues can be somewhat
110 sidestepped by switching to voltage recording.
111
112 However, most mPSCs go undetected because of the electrophysiology of the neuron itself. Distal
113 minis leak charge via the dendritic membrane, but an even more significant amplitude attenuation,
114 40-fold or more, is inflicted by charging the membrane capacitance of the entire dendritic arbour
115 (Larkum et al., 2009; Major et al., 2013a; Nevian et al., 2007; Stuart and Spruston, 1998; Williams
116 and Mitchell, 2008; Williams and Stuart, 2002). Such amplitudes, at the soma, are often
117 indistinguishable from noise fluctuations (approximately 97 µV on average in layer 5 neurons
118 (Nevian et al. 2007)). Recording from thin dendrites close to synaptic input sites is technically
119 challenging (Nevian et al. 2007). Therefore, a reliable yet widely accessible quantal analysis method,
120 based on somatic whole-cell patch recording, would require taking account of the background noise
121 component in addition to measuring putative mPSPs (or mPSCs).
122
123 Here we describe such a method based on separate recordings of excitatory mPSPs (mEPSPs) in the
124 presence of background physiological noise (‘noise with minis’ recording) and of noise alone after
125 blocking mEPSPs pharmacologically (‘noise-alone’ recording). To detect mEPSP-like events in these
126 recordings we used a newly developed algorithm called ‘minis’ which is described in our companion
127 article (Dervinis and Major, 2023). Because of larger minis overshadowing smaller potentials by

128 summating them on rise phases and reducing their amplitudes on decay phases of larger minis
129 (discussed in length in our companion article (Dervinis and Major, 2023)), events detected in the
130 'noise-alone' recording cannot be used to account for the noise component in the 'noise with minis'
131 recording. Instead, simulated minis must be used by superimposing them on the 'noise-alone'
132 recording until the 'noise with simulated minis' voltage trace closely matches the 'noise with real
133 minis' recording in terms of amplitude and rise time distributions of detected events. Therefore, we
134 augmented 'minis' software with a genetic optimisation algorithm (GA) that automatically adjusts
135 amplitude and rise times of simulated minis. The novel quantal analysis method produced an
136 unbiased quantal size estimate for excitatory synapses in the CNS which was approximately equal to
137 32 pC and was conserved across pyramidal cells of all sizes in cortical layers 2/3 and 5. 'Minis' thus
138 provides a straightforward quantal analysis method of detecting mPSPs and mPSCs in somatic
139 recordings and separating smaller of these events from background noise fluctuations.
140

141 # Materials and Methods

142 **Animals and electrophysiology**

143 All experimental procedures were carried out in accordance with the UK Animals (Scientific
144 Procedures) Act 1986 at the Cardiff University under Home Office personal and project licenses. The
145 full description of electrophysiology procedures is provided in our companion article (Dervinis and
146 Major, 2023). Briefly, coronal somatosensory cortical slices obtained from 19- to 27-day old Wistar
147 rats (RRID:RGD_13508588; n = 11) of either sex were used to obtain whole-cell recordings (n = 14) of
148 mEPSPs in the background of physiological noise ('noise with minis' condition) by applying artificial
149 cerebrospinal fluid (aCSF) solution added with an action potential (AP) and inhibitory postsynaptic
150 potential (IPSP) blockers. Following this phase, the recordings were continued further after adding
151 excitatory postsynaptic potential (EPSP) blockers ('noise-alone' condition).
152

153 Passive membrane time constant, total capacitance, and cell's input resistance (the bridge balance
154 error) were estimated by injecting current pulses as described in (Major et al., 1993).
155
156 **Experimental design**
157 The goal of the study was to design a quantal analysis method based on somatic recordings of minis.
158 Due to low signal to noise ratio, simulations of minis were used to infer the signal component and to
159 eliminate the noise component in these recordings.
160
161 The experimental design of this study was similar to the one described in our companion article
162 (Dervinis and Major, 2023). As described in the previous section, whole-cell recordings were
163 obtained where first mEPSPs were recorded in the background of physiological noise followed by
164 blocking them pharmacologically to record 'pure' noise in the absence of minis. Simulated mEPSPs
165 (smEPSPs) were then added to the noise traces and the 'minis' algorithm was applied to this 'noise
166 with simulated minis' voltage trace. The resulting distribution of detected events in terms of their
167 amplitudes and 10-90% rise times was compared to the equivalent distribution based on 'noise with
168 real minis' recording. Discrepancy between the two distributions was used to inform the GA which
169 would then adjust the distribution of smEPSPs and generate new 'noise with simulated minis'
170 voltage traces and compare them again to the equivalent distribution based on 'noise with real
171 minis' recording. This procedure was repeated multiple times (in the order of tens to hundreds of
172 generations with 260 examples per generation) until the two distributions were closely matched,
173 within the bounds of chance statistical errors. At the end of this process the minis' distribution used
174 for simulating a closely matched recording was deemed to be the inference of the true minis'
175 distribution underlying the 'noise with real minis' recording.
176
177 **Detection of miniature postsynaptic potentials**

178 Detection of real and simulated mEPSPs was carried out using 'minis' software. The detailed
179 description of this detection algorithm is provided in our companion article (Dervinis and Major,
180 2023). We used the same detection algorithm parameters as described in that article except for the
181 amplitude range which was set to 0.02-10 mV.
182
183 **Selection of recordings for fitting distributions of detected real minis-like events**
184 Prior to carrying out any estimation of minis' distribution, segments of 'noise with real minis' and
185 'noise-alone' recordings were carefully selected. Segments containing unusual amount of noise or V_m
186 glitches were rejected. Parts of recording showing instability or drift of recording parameters were
187 also rejected to ensure that only good quality data was used. We called this a preprocessing stage
188 and data analyses we performed at this stage were inbuilt into 'minis' software.
189
190 As part of the preprocessing stage 'minis' produced 7 graphs showing the evolution of various
191 recording parameters across the entire duration of a single recording. An example is provided in
192 Figure 1 showing these graphs as individual panels of the figure for the longest obtained recording.
193 Figure 1A shows the evolution of V_m from the very beginning of the recording obtained in the regular
194 aCSF with APs present to the very end of the recording where APs and mIPSPs as well as mEPSPs
195 were blocked for some time ('noise-alone' recording phase). The data is shown, after removing V_m
196 segments containing responses to injected current pulses, with a total duration of 8520 s.
197 Throughout the entirety of this recording the baseline V_m varied between –70 and –67 mV and, thus
198 remained relatively stable.
199
200 There are three time markers that extend across all figure panels marking the time when the aSCF
201 containing TTX, gabazine, and CGP55845A was infused to block APs and IPSPs (the first marker), the
202 time when APs were observed to cease (the second marker), and the time when the aCSF containing
203 NBQX and CPP was infused to block remaining EPSPs (the third marker). The recording segment

204 between the second and the third markers constituted the 'noise with minis' recording, while the
205 segment following the third marker when mEPSPs were eventually blocked constituted the 'noise-
206 alone' recording. The shaded regions that also extend across all panels of Figure 1 mark files that
207 were selected for subsequent minis' distribution fitting analyses.
208
209 The remaining panels of Figure 1 were used to guide the data selection for subsequent analyses. The
210 standard deviation (SD) of the V_m (Figure 1B) was useful in determining the borders of different
211 recording types. Stable prolonged decreases in SD reliably indicated when APs or minis were
212 effectively blocked by corresponding pharmacological agents. Sudden brief increases in SD flagged
213 problematic recording segments containing higher levels of noise or V_m glitches. Gradual increases in
214 SD suggested the ensuing gradual deterioration of the recording quality.
215
216 Similar information was also provided by the evolution of amplitudes of the top 10% (amplitude-
217 wise) of all detected minis-like events in a single sweep (Figure 1C). Prolonged drop in the
218 amplitudes marked borders between recording types, while sudden jumps were indicative of V_m
219 instabilities. Finally, effective decay time constants of the same top 10% (by amplitude) of detected
220 events (Figure 1D) could be used as an indicator for the presence/absence of minis. Blocking minis
221 resulted in time constants becoming large and fluctuating unstably, indicating that only noise
222 fluctuations were being detected that did not possess typical decay dynamics common to PSPs.
223
224 Further insights into the recording quality over time were provided by impulse based measures.
225 Passive membrane time constant measurements over time (Figure 1E) were expected to remain
226 stable. Deviations from this expectation could signal a change in passive membrane properties and
227 the degradation in the recording quality. Total membrane capacitance (Figure 1F) was also expected
228 to be stable over time. Change in the capacitance could indicate tear of the membrane or loss of
229 part of the cell or some substantial uncontrolled destabilisation of the recording. Finally, change in

input resistance (detected from a change in the bridge balance error; Figure 1G) was not permitted to exceed the estimate obtained at the beginning of the recording by more than twice. Violation of this rule of thumb indicated a deterioration in the recording quality potentially resulting from debris accumulating in the recording pipette, movement of the pipette tip or the recorded cell body, partial formation of a membrane 'tube' (similar to what would happen in the process of producing an outside-out patch by slowly retracting the pipette), or other reasons.

We obtained the above-discussed 7 longitudinal recording state/quality indicators for all our recordings. Multipaneled graphs showing these indicators for each individual recording separately are provided in Supplementary Figures 1-13.

Simulations

Simulating distributions of miniature excitatory postsynaptic potentials with a range of amplitudes and rise times

All simulations were carried out using 'minis' software developed in Matlab (Mathworks; RRID:SCR_001622) and performed on Cardiff School of Biosciences' Biocomputing Hub HPC/Cloud infrastructure. Simulation of minis-like events was based on an analytical solution to the passive cable equation for a transient current (Rall, 1977) using 100 lumped terms with a double exponential synaptic current with τ_1= 0.15-3 ms (optimised) and τ_2 = 2 ms (Major et al., 1993). The detailed description of how arbitrary shape PSPs were obtained is provided in our companion article (Dervinis and Major, 2023).

A pool of simulated events was generated combining 4 bivariate (amplitude and 10-90% rise time) normal distributions. 6 parameters described each distribution: amplitude mean μ_X and standard deviation σ_X, 10-90% rise time mean μ_Y and standard deviation σ_Y, a correlation (or rotation) factor ρ, and a scale factor n:

$$f(x,y) = \frac{n}{2\pi\sigma_X\sigma_Y\sqrt{1-\rho^2}} e^{-\frac{1}{2(1-\rho^2)}\left(\left(\frac{x-\mu_X}{\sigma_X}\right)^2 - 2\rho\left(\frac{x-\mu_X}{\sigma_X}\right)\left(\frac{y-\mu_Y}{\sigma_Y}\right) + \left(\frac{y-\mu_Y}{\sigma_Y}\right)^2\right)}.$$

All distribution parameters were controlled by the GA.

Fitting distributions of detected real minis-like events

Matlab's ga() function was used to control 24 parameters describing 4 bivariate normal distributions (6 parameters per distribution). Additional controlled parameters were the synaptic rise time constant τ_1 which ranged between 0.15 and 3 ms and the passive membrane time constant τ_m. The range for the latter constant was taken to be between 0.95 times and 1.05 times the initial estimate based on the average waveform of all minis-like events detected in the 'noise with real minis' recording. Thus, there were 26 parameters in total controlled by the GA.

The GA would start by generating multiple distributions of smEPSPs (i.e., 'individuals'; we used 260 individuals per 'generation'). Events would be drawn pseudo-randomly from a distribution and then simulated events of the right shape (in terms of amplitude and 10-90% rise time) would be superimposed on the 'noise-alone' recording at time points that were chosen pseudo-randomly (Figure 2). For generating the initial set of individuals ('population'), the GA chose parameters pseudo-randomly within prescribed ranges. For each of the four bivariate normal distributions the parameter ranges were as follows: μ_X (-0.1-1 mV), σ_X (0.01-1 mV), μ_Y (-1-10 ms), σ_Y (0.25-10 ms), ρ (-1 to 1), and n (0-10000 for the first distribution and –10000 to 10000 for the remaining three distributions). Any negative count bins within the resulting final distribution were zeroed out. Any events with amplitudes below the simulation threshold (varying positive value) or negative rise times were excluded.

In the next step the GA assessed the fitness of each individual in the generation by using the cost function (explained in the next subsection). The top 5% of the most fit individuals survived to the

281 next generation without change while individual crossover, genetic migration, and other GA
282 parameters were set to default values of the Matlab's ga() function except for the mutation function
283 type which was set to 'mutationadaptfeasible'. A new evolved generation of individuals was then
284 created. Which then served as the basis for yet another generation. This process was repeated until
285 an individual with the lowest cost (highest fitness value) possible was created, there was no
286 improvement in the fitness for 100 consecutive generations, or the number of generations reached
287 1000.
288
289 In the case when the GA terminated without attaining the highest possible fitness value, distribution
290 fitting procedure was reinitiated using the most fit individual as a seed. The population genetic
291 diversity was reset by setting the GA-controlled parameter ranges to ±5% of the original ranges
292 relative to the seed parameters. The rerunning of distribution fitting was repeated until the GA
293 generated the most fit individual possible, an acceptable level of fitness was reached (defined in the
294 next subsection), or there was no improvement in fitness compared to the previous run for three
295 consecutive repeats. In the latter case, the entire distribution fitting procedure could be repeated
296 starting with a high simulated amplitude lower threshold (e.g., 200 μV) with the threshold being
297 gradually lowered until a 'good enough' fit was attained. This 'backwards' fitting procedure was
298 required for several recordings due to them having large mean amplitude and, therefore, failing to
299 converge on an acceptable solution with a realistic minis source distribution using a low simulated
300 amplitude lower threshold.
301
302 If the most fit individual was within acceptable levels of fitness values, the lower threshold on
303 smEPSP amplitude was increased by 0.005 mV (or lowered in certain cases) and the entire fitting
304 procedure rerun from the beginning till the end. This procedure was repeated until the GA stopped
305 converging on a solution with acceptable fitness values. The reason for attempting to push up the
306 lower limit of the amplitudes of the smEPSPs is that GA-generated solutions are not unique.

307 Matching ‘noise with real minis’ recording can generally be achieved by using a distribution of fewer
308 relatively large amplitude smEPSPs or more numerous smaller amplitude smEPSPs, or some
309 distribution between these extremes. There is an infinite number of such distributions with ever
310 decreasing amplitudes of smEPSPs (in theory, all the way down to events resulting from arbitrarily
311 brief single AMPAR or NMDAR channel sub-conductance state openings injecting arbitrarily small
312 amounts of charge). Therefore, the GA with the thresholding procedure described above has no
313 guaranteed way of arriving at the proven true distribution of minis, only at a distribution giving an
314 approximate *upper limit* on the *mean* (or median) mini amplitude (the upper amplitude tail of the fit
315 would be more reliable though, just as with detecting those events manually).
316
317 *Cost function*
318 The goal of the minis’ distribution fitting procedure was to match ‘noise with simulated minis’ and
319 ‘noise with real minis’ recordings as close as possible in terms of the distribution of amplitudes and
320 10-90% rise times of detected minis-like events in the two types of V_m recording traces (‘simulated’
321 vs. ‘real’ distributions), in the process ‘cancelling out’ any systematic errors in amplitudes or shapes
322 introduced by the detection algorithm or the superposition of events. This was achieved by
323 minimising the cost function using the GA. The cost function was composed of four types of
324 components: shape constraints on the simulated minis distribution, sums of absolute deviations
325 (SADs) between ‘simulated’ and ‘real’ distributions, sums of signed deviations (SSDs) between
326 ‘simulated’ and ‘real’ distributions, and maximal absolute deviations (MADs) between ‘simulated’
327 and ‘real’ distributions. We avoided using the sum of squared errors (SSE) because it is sensitive to
328 outliers.
329
330 We calculated the typical ranges of SADs and MADs for each of the 14 recordings by taking the
331 individual ‘noise with real minis’ recording and dividing it into smaller files (range was 15-606 files)
332 the size of the single recording sweep (a typical sweep lasted 20 s). Each file in this set was subjected

to minis detection procedure resulting in a set of 'real' distributions. They were then subtracted from each other, and corresponding SAD (sum of absolute deviations) and MAD (maximum absolute deviation) scores were calculated for each of the possible n*(n-1)/2 file pairings (range 105 to 183315, corresponding to 15 to 606 available files). 6 different SAD- and MAD-based scores (12 altogether) were calculated based on: distributions of (1) amplitudes of *all* detected events, (2) amplitudes of top 50% largest detected events, (3) amplitudes of top 10% largest detected events, (4) amplitudes of top 2% largest detected events, (5) distribution of all 10-90% rise times, and (6) a joint amplitude and 10-90% rise time distribution. Moreover, 3 different SSD-based scores were calculated based on: (1) amplitudes of top 50% largest detected events, (2) amplitudes of top 10% largest detected events, and (3) amplitudes of top 2% largest detected events. These latter scores constrained high-amplitude tails of 'simulated' distributions to have sufficient counts to avoid negative distribution deviations in the tails. Similarly to the lower simulated amplitude limit, these three scores served to constrain the non-uniqueness of simulated minis distributions caused by the lower amplitude end of the distribution.

The smallest percentile that guaranteed to include half of all file combinations with all their 15 respective SAD,MAD, and SSD score values falling below this percentile threshold simultaneously ('15-score combined 50th centile'; Tables 1 and 2) was used to determine which SAD or MAD cutoff values (*all* SAD and MAD scores for 'noise with simulated minis' traces had to fall below these values) should be used for all 15 types of scores to construct the cost function (SSD scores had to be simply positive; Figure 3). As described above, the centile value was estimated based on single sweep files. The same centile value was then used to work out SAD and MAD scores for larger size files (typically the size of 5 recording sweeps to match the size of the 'noise-alone' recording file) that were used during the GA-controlled fitting procedure.

The cost function was constructed of 6 types of SAD scores and 6 types of MAD scores estimated using the '15-score combined 50th centile' procedure and 3 types of positive SSD scores. These 15 scores were used to evaluate how close the 'simulated' distribution was to the single selected 'real' distribution that was deemed to be of the best quality by a human observer. Typically, it was a file close to the end of the 'noise with minis' recording epoch, therefore, being the most similar file, in terms of recording quality parameters, to the 'noise-alone' recording epoch (which was generally the first good-quality epoch after pharmacological blockade of neurotransmission was deemed complete). Additional corresponding 15 'deviation' scores (same as SADs, MADs, and SSDs but comparing to all available data distributions at once) were calculated assessing how much each 'real' or 'simulated' distribution deviated from the full set consisting of all 'real' distributions and the single 'simulated' distribution. To be designated a good enough fit, the 'simulated' distribution was expected to have lower deviation scores than the worst performing 'real' distribution (so the simulated distribution's histograms would not be picked as the 'worst outlier' by a double-blind observer). 'Simulated' distributions were further penalised if their underlying 'simulated minis' distribution violated the 10-90% rise time skewness constraint which stipulated that the mean 10-90% rise time of simulated minis should exceed the median at least by a half of the standard deviation. Finally, 'simulated' distributions were also penalised if their underlying 'simulated minis' amplitude distribution had a sharp cliff at its lower end. Hence, there were 32 fitness components in total (15 + 15 + 1 + 1 = 32).

If all amplitude SAD, MAD, SSD, and deviation scores for comparing the 'simulated' distribution to the 'real' distribution were satisfied (≤ 15-score 50th centile SAD and MAD values and ≥ 0 SSD values) at the end of the fitting procedure, the fit was deemed to be 'good enough'. Alternatively, the fit could also be deemed good enough if all amplitude and 10-90% rise time 'file population' deviation scores (all 15) were satisfied (excluding SAD, MAD, and SSD scores).

Final distribution fit acceptance

The notion of a 'good enough' fit is somewhat arbitrary. Once the fitting procedure was completed, we set out to test whether the final fit was acceptable using statistical tests. We divided 'noise with real minis' recordings into smaller files of the same length as the 'noise-alone' recording and constructed a set of 'real' distributions by running 'minis' detection algorithm on these files. We then compared these individual 'real' distributions to each other by subtracting their amplitude and 10-90% rise time distributions from each other, taking absolute value of the difference, and summing over all bins. Finally, we selected the worst and the best performing 'real' distributions in terms of their sums of absolute distribution bin deviations (SADs).

We also compared the 'good enough' 'noise with simulated minis' distribution to the set of normalised 'real' distributions. The comparison yielded another set of sums of normalised absolute distribution bin deviations (SADs). The mean of this set was then compared to the means of the worst and best performing 'real' sets using Wilcoxon-Mann-Whitney test. If the 'simulated' set mean was significantly larger than the worst 'real' set mean, the 'simulated' distribution was deemed to be an underfit and, therefore, rejected and the fitting procedure was continued. In contrast, if the 'simulated' set mean was significantly smaller than the best 'real' set mean, the 'simulated' distribution was deemed to be a likely overfit. The 'good enough' fit was accepted if the 'simulated' set mean was not significantly larger than the worst 'real' set mean.

Statistical analyses

Parametric inferential statistics tests were used for minis' incidence rates, mean amplitudes, and cell's total capacitance as quartile-quartile plots indicated that these measures were normally distributed. Sums of absolute distribution bin deviations (SADs) were often not normally distributed and, therefore, were tested using a nonparametric Wilcoxon-Mann-Whitney test.

Data accessibility

All data analysed in this study are publicly available (GIN DOI will appear in version 2 of the manuscript). The available data include 'noise with minis' and 'noise-alone' whole-cell patch membrane potential recordings that were used in computer simulations and minis' distribution fitting. All electrophysiological recordings were stored in Axon Binary File (ABF) format.

Code accessibility

All analyses were carried out in Matlab and the analysis code is publicly available on GitHub (DOI will appear in version 2 of the manuscript). The code is complete with instructions on how to reproduce all figures reported in this study.

Software accessibility

The present study reported the use of a novel quantal analysis method that is part of 'minis' software available on GitHub (Dervinis, 2022).

Results

Estimating quantal size by direct subtraction of noise component

We have analysed 'noise with minis' recordings and 'noise-alone' recordings with the 'minis' detection algorithm. Detected mEPSP-like events had a particular shape amplitude and 10-90% rise time distributions that resembled log-normal or gamma distributions (Figure 4), left skewed with a long tail on the right. In the amplitude domain the lower end of the distribution contains a mixture of real minis and noise fluctuations that were misidentified as real events (but missing small minis due to them being cancelled out by noise, summating with larger minis, or failing to be detected due to being on a decay phase of a big preceding mini – the 'overshadowing' effect).

We (naively) argued that if the noise component could be reliably estimated based on the 'noise-alone' recording where synaptic activity has been pharmacologically blocked, it could be directly subtracted from the 'noise with minis' distribution yielding an estimate of the pure minis' component. Figure 4A shows both 'noise with minis' and 'noise-alone' detected event amplitude distributions superimposed over each other. After subtracting the 'noise-alone' distribution from the 'noise with minis' distribution there appear negative low amplitude bins in the resulting distribution (indicated by an arrowhead in Figure 4A). These missing low amplitude events are caused by a greater number of small false positive mini-like detections in the noise-alone traces, and larger minis overshadowing smaller minis and small amplitude noise fluctuations in the 'noise with minis' recording (we have discussed this phenomenon in great length in our companion article (Dervinis and Major, 2023)). Therefore, the direct subtraction approach can only provide a relatively crude 'first order' high-end upper limit on the mean of the minis' amplitude distribution. Nevertheless, this over-estimate is more reliable than a highly subjective approach of simply estimating the mean amplitude based on events detected using a high amplitude threshold.

Estimating quantal size by simulating excitatory postsynaptic potential source distribution

An alternative and more reliable way of estimating the quantal size in our recordings is to estimate the minis component directly using simulations. This relies on 'minis' optimisation algorithm (GA) being able to closely match a 'noise with simulated minis' voltage trace (Figure 2) with 'noise with real minis' recordings in terms of amplitude and 10-90% rise time distributions of minis-like events detected within these traces. We were able to successfully do that for all our recordings (see Figure 5 and Supplementary Figures 14-26) with one particular example shown in Figure 5. In terms of the example shown in Figure 5, the overall amplitude SAD of the 'simulated' distribution was not underperforming the worst-performing 'real' distribution (unidirectional 'simulated' SAD > worst-performing 'real' SAD Wilcoxon-Mann-Whitney rank sum 'underfit' test $U = 406$, $p = 3.4 \times 10^{-9}$; downward arrow indicates 'simulated' SAD < 'real' SAD relationship in Figure 5) and was not

outperforming the best ‘real’ distribution (unidirectional ‘simulated’ SAD < best-performing ‘real’ SAD Wilcoxon-Mann-Whitney rank sum ‘overfit’ test U = 288, p = 0.72). Similarly, the ‘simulated’ 10-90% rise time distribution was also neither an underfit (unidirectional ‘simulated’ SAD > worst-performing ‘real’ SAD ‘underfit’ test U = 279, p = 0.41; upward arrow indicates ‘simulated’ SAD > ‘real’ SAD relationship in Figure 5) nor an overfit (unidirectional ‘simulated’ SAD < best-performing ‘real’ SAD ‘overfit’ test U = 275, p = 0.55).

All simulations produced ‘good enough’ matches showing amplitude and 10-90% rise time distributions of detected minis-like events being within the range of (and thus indistinguishable from) amplitude and 10-90% rise time count values measured in sets of ‘real event’ distributions (Supplementary Figures 14-26). None of the fits were performing worse than the worst-performing ‘real’ distribution qualifying them as ‘good enough’ fits. All resulting minis source distributions are displayed in Figure 6 and Supplementary Figures 27-39. An example in Figure 6 shows that the ‘real minis’ source distribution likely has a log-normal or gamma-like shape in both amplitude and rise time domains.

Incidence rates (frequencies of minis per second) estimated based on simulated minis source distributions ranged roughly between 10 and 100 minis/s (Figure 7). This estimate is an order of magnitude higher than the one based on the literature and significantly higher than the one based on the direct subtraction method ($t(13) = 3.37$, $p = 0.005$) and also higher than the estimate based on amplitudes higher than a chosen 0.8 mV threshold (unrealistically high threshold; $t(13) = 3.76$, $p = 0.002$). It is precisely within the range predicted in our companion article (Dervinis and Major, 2023). However, this range is possibly still somewhat of an underestimate as minis source distributions were often generated using a lower limit on simulated amplitudes to constrain the distribution non-uniqueness as discussed in the Methods subsection on the distribution fitting.

487 Mean amplitudes of minis derived using simulations ranged between 53 and 198.4 μV (overall mean
488 of 115.3 ± 5.7 μV, layer 2/3 mean of 137.3 ± 11.1 μV, and layer 5 mean of 93.4 ± 9.4 μV; Figure 8A).
489 When compared to capacitance estimates (or 1/capacitance), there was a strong inverse correlation
490 between the mean amplitude and cell's capacitance (which is proportional to the cell's size; r =
491 0.966, $p = 2.1x10^{-8}$, $R^2 = 0.933$, assuming capacitance per unit area is more or less a biological
492 constant for each cell class/type of membrane/density of channels with charged gates moving within
493 the membrane - increasing capacitance (Gentet et al., 2000)). That is, the larger the cell, the smaller
494 the amplitude of its somatically detected minis and vice-versa. This relationship is predicted by the
495 theory of capacitors (C = Q/V, where C stands for capacitance, Q stands for charge, and V stands for
496 voltage across the cell's membrane), and it is a direct demonstration of an attenuating effect of cell's
497 capacitance on the amplitude of somatically detected minis. If a direct line was drawn through the
498 data and the origin of the axes in Figure 8A, the slope of this line would provide a quantal size
499 estimate for excitatory synapses in the CNS in terms of 'injected' charge ($Q = \Delta V/ \Delta(1/C)$) which is
500 approximately equal to 32 fC in this case. The fact that the least square fitted line to the data alone
501 coincided with the line fitted to the data that also passed the origin and, therefore, had no intercept
502 term indicated that no active mechanism was in place to compensate for the attenuation of the
503 average minis' amplitude due to the size of the cell.
504
505 Another notable observation was that the mean amplitude estimates derived either by noise
506 subtraction or by minis source distribution simulation were correlated (r = 0.705, p = 0.005, R^2 =
507 0.498 Figure 8B). The equation of the line (1.18x – 39.3) fitted to this data provided a way to
508 approximate the mean amplitude of fitted minis' source distribution by subtracting the intercept
509 term (39 μV) from the means derived by 'naïve' noise subtraction.
510
511 *Generic miniature excitatory postsynaptic potential distribution in neocortex*

512 To construct a generic mEPSP distribution, we normalised amplitudes of simulated minis' source
513 distributions shown in Figure 6 and Supplementary Figures 27-39 by dividing them by their
514 respective means, taking the total average, smoothing the resulting distribution, and then scaling
515 the amplitudes to the overall mean (115.3 ± 5.7 μV). The resulting combined (amplitude and 10-90%
516 rise time) distribution is shown in Figures 9A and B. The corresponding marginal amplitude and 10-
517 90% rise time distributions are shown in Figures 9C and D, respectively. Both marginal distributions
518 have left-skewed log-normal-like or gamma-like distributions. This may be useful in neural network
519 simulations, or to potentially speed up (and constrain) fitting of simulated minis on noise to real
520 minis with noise, using the GA (e.g., limit the source distribution to one 2-D 'rotated' log-normal or
521 gamma distribution).
522

523 # Discussion

524 In this article we reported two major scientific advances. First, we described a novel quantal analysis
525 method that is based on sequential somatic recording, from a given neuron, of a) mEPSPs (after
526 blockade of action potential-mediated neurotransmission, and all inhibitory neurotransmission,
527 including miniature IPSPs) on a background of other physiological noise, and b) recordings of noise
528 alone, after subsequent additional pharmacological blockade of mEPSPs (all glutamatergic ionotropic
529 excitatory neurotransmission). The latter type of recording provides a means to estimate the
530 properties of the noise component which can then be used to take into account noise fluctuations in
531 the combined minis and noise recording. However, this was done not by a direct subtraction of the
532 histogram of amplitudes (and rise times) detected from the noise component, but rather by the
533 simulation of the underlying minis component and repeatedly superimposing the waveforms of
534 simulated minis onto the noise trace until the histograms detected from the 'noise with simulated
535 minis' voltage trace closely matched those detected from the 'noise with real minis' recording. The
536 key tool to achieving this match was the genetic algorithm that optimised the parameters of the 2-

537 dimensional simulated minis distribution in terms of amplitudes and 10-90% rise times,
538 simultaneously, to best fit the experimental data distributions.
539
540 The second major advance was the use case for the novel quantal analysis method that successfully
541 measured the mean 'electric charge injected' size of excitatory synapses of cortical pyramidal cells
542 which was shown to be approximately 32 fC, across the entire sample of neocortical pyramidal
543 neurons recorded. This number was inferred from the slope of the line fitting minis' mean amplitude
544 and cell's total capacitance data in accordance with the theory of capacitors. The fact that this line
545 had an intercept at the origin of the axes indicated that there was no biological compensation (other
546 than *number* of synapses) for the amplitude attenuation of minis due to cell size (i.e., total
547 capacitance). Indeed, cell capacitance played a major role affecting the *voltage* amplitude of mEPSPs
548 resulting in a large proportion of mEPSPs being otherwise indistinguishable from noise (as
549 independently found in numerous other studies, e.g., (Major et al., 2013b; Nevian et al., 2007),
550 summarised in (Major et al., 2013b)). The number of these 'missed' minis was so high that the
551 estimated minis' incidence rate (frequency) was in the order of 10-100 minis/s: an order of
552 magnitude higher than typically reported in the synaptic physiology literature (with the notable
553 exception of (Nevian et al., 2007), which predicted this result, by simultaneous dual somatic and
554 basal dendritic whole-cell patch recordings of mEPSPs, with dendritic detection, and simultaneous
555 somatic measurement). Finally, both the amplitude and 10-90% rise time distributions of minis had a
556 log-normal- or gamma-like shape.
557
558 These findings have a few major implications. First, the method, as used for estimating the mEPSPs'
559 distributions in cortical layers 2/3 and 5 of cells of various size and then using these distributions to
560 arrive at the electrical size of excitatory synapses serves as a proof of principle that it can be
561 successfully used to estimate PSP distributions of various types in the CNS. The next logical step of
562 this method is to extend its application to the estimation of amplitude and rise time distributions of

mIPSPs generated by different types of inhibitory synapses and, as a result, the electrical sizes of these different inhibitory synapses. Moreover, the ability to get relatively accurate quantal size estimates unobscured by physiological noise is important for constraining synaptic parameters in physiologically realistic simulations of neural activity. For example, now we should be able to estimate how many active synapses are needed to generate an NMDA spike within a single dendritic segment (Major et al., 2013b). The importance of these number estimates is not restricted to the domain of physiologically realistic simulations but also extends to more abstract computations that use NMDA spike-like mechanisms as coincidence detectors in the latest cortically inspired models of artificial intelligence (Hawkins et al., 2019). It is thus imperative to arrive at accurate estimates of synaptic transmission parameters.

These findings also draw attention to methodological issues in the field of synaptic physiology. As discussed in our companion article (Dervinis and Major, 2023), the commonly reported incidence rates for mEPSCs are well below 10 minis/s. Even if one is in doubt of the incidence rates that we arrived with the help of simulations that lie in the range of 10-100 minis/s, the range of incidence rates given by direct subtraction of the distribution of events detected in the 'noise-alone' recording from the distribution based on the 'noise with minis' recording is still within 5.9 and 26.7 minis/s which we know to be an underestimate. Therefore, reported minis' incidence rates below 10 minis/s are certainly underestimates. This may have multiple causes, including lower slice temperatures in the majority of studies (we used physiological, ca. 37 degC), and a significant temperature dependence of synaptic release, as well as differences in slice health and slicing angle (which can affect branch 'amputations'). Another big cause would be the use of voltage clamp, especially if the series resistance in not compensated fully, as this low-pass filters traces and obscures smaller minis. (e.g. trace in Supplemental?) As discussed earlier, these estimates could be improved by switching to voltage recording instead of using the voltage clamp (Major, 1993a; Rall and Segev, 1985; Spruston et al., 1993; Williams and Mitchell, 2008) but at the price of somewhat slower decay times of minis

589 (Major 1993), thus more temporal overlap and consequent difficulties detecting peaks. But more
590 importantly, a strong association between cell capacitance (i.e. surface area) and how much
591 somatically recorded minis' amplitudes are attenuated indicates that special care must be taken to
592 account for the effect of background noise fluctuations on the amplitude measurements as we have
593 done here. This association is yet another evidence supporting experimental observations of massive
594 mini amplitude attenuation as the PSP spreads from its dendritic source location to the soma
595 (Larkum et al., 2009; Major et al., 2013a; Nevian et al., 2007; Stuart and Spruston, 1998; Williams
596 and Mitchell, 2008; Williams and Stuart, 2002)., especially in cells with large dendritic arbours, hence
597 large surface areas and overall membrane capacitance. Dendritic spines and post-synaptic densities
598 (the specialised regions opposite release sites, containing tethered synaptic receptors) are not
599 grossly different between different classes of pyramidal neurons in the neocortex, although
600 significant differences exist between cortical layers, cortical areas, and animal species (Yuste, 2010).
601
602 It is also important to note that understanding the link between cell capacitance and somatically
603 recorded average mini amplitudes as well as knowing actual shapes of mini distributions in terms of
604 their amplitudes and rise times allows us to generate artificial data where ground truth is known.
605 Such labelled data could be used to train artificial neural networks (ANNs) which could then be used
606 develop next generation powerful quantal analysis methods allowing detection of minis directly in
607 mixed 'noise with minis' recordings. Perhaps such methods would not only do away with the need to
608 obtain relatively long voltage recordings with consecutive pharmacological phases but could
609 potentially fully automate the mini detection process. We are not the first to suggest the application
610 of ANNs to this issue (see (Pircher et al., 2022) and (Wang et al., 2024)). However, we are not aware
611 of attempts to use realistic mini distributions for this purpose.
612
613 Even though the novel quantal analysis method we present here is an important advance, it
614 nevertheless has limitations. One of them is the need for long duration recordings using different

615 pharmacological agents at various stages of recording. However, the somatic recording set up is not
616 as complicated and high-skill as an alternative multisite 2-photon targeted dendritic recording set up
617 would be ((Nevian et al., 2007), a heroic technique which has never been copied in another lab).
618 Experiments themselves could be further streamlined, as we did in some cases, by pre-blocking
619 action potentials before obtaining the whole-cell recordings. This is particularly useful for smaller
620 cells which are more prone to osmotic overloading or shrinkage and resulting recording instability
621 after a few tens of minutes (the pipette solution cannot exactly reproduce the cytoplasm, as it has
622 no proteins or macromolecules in it). Moreover, the distribution fitting procedure involving the GA
623 can be lengthy and computationally intensive. However, 'minis' software is parallelised at the PSP
624 detection level, as well as at the GA optimisation level making it particularly suitable to be executed
625 on multi-core computing clusters. Although 'minis' software combined with the two-stage recording
626 set up offers an unprecedented control for the background physiological noise, provided recording
627 stability is very good throughout, we understand that many researchers may not be persuaded to
628 adopt it themselves. The possibility of misleading fits if the recording noise became substantially
629 worse between 'noise with minis' and 'noise-alone' recording phases needs to be vigilantly excluded.
630 Therefore, the adoption of ANNs for the next generation of 'minis' software based on current
631 findings and future use-cases offers a way to simplify the current approach (including recording
632 stability quality control).
633
634 Some researchers may be critical of a method that does not rely on a direct measurement of minis
635 but rather on an approximation via indirect means using simulations. This is a valid criticism that
636 could be addressed in the future by using a method of repeatedly subjecting a voltage recording to
637 the minis detection procedure with an increasingly lower threshold while subtracting detected
638 events from the voltage recording. This approach potentially could recover most of the smaller minis
639 that are overshadowed by the larger ones (the so called 'negative bins' problem illustrated in Figure
640 4A), providing the waveforms were reasonably stereotyped in shape (not the case under voltage

641 clamp, (Major, 1993b)). Furthermore, other researchers may question the ability to
642 pharmacologically isolate the background physiological noise. Our 'noise with minis' recordings may
643 contain random openings of individual AMPA receptor (AMPAR) or NMDA receptor (NMDAR)
644 channels (possibly extra-synaptic) and our 'noise-alone' recordings may fail to fully eliminate channel
645 openings in the presence of quantal release of neurotransmitter (although we used high doses, well
646 above IC50s' (Lehmann et al., 1987; Randle et al., 1992) and rapid slice perfusion, to achieve quick
647 wash-in times). Background/physiological/electrical noise itself may be drifting between the two
648 conditions with the presence or absence of mEPSP pharmacological blockers. Although there may be
649 some reason to suspect that may be the case, occasionally, we rejected any recordings with such
650 instabilities. these factors are unlikely to have affected the results significantly due to small
651 amplitude nature of these membrane potential variations.
652
653 Despite some of the limitations discussed above, the method and its use case presented in this
654 article provide a major breakthrough in the field of synaptic physiology. Further research would
655 inevitably see the improvement of this method by developing the underlying algorithm in a few
656 promising directions with the application of ANNs being one of them. This should allow the
657 simplification of the minis recording procedure by eliminating the need for 'noise-alone' recording
658 epochs. Finally, the application of this novel quantal analysis method to describe the properties of
659 various types of inhibitory synapses in the neocortex would the next logical step leading to yet
660 another breakthrough.

References

Bekkers JM. 1994. Quantal analysis of synaptic transmission in the central nervous system. *Curr Opin Neurobiol* **4**:360–365. doi:https://doi.org/10.1016/0959-4388(94)90097-3

Biró ÁA, Holderith NB, Nusser Z. 2005. Quantal Size Is Independent of the Release Probability at Hippocampal Excitatory Synapses. *The Journal of Neuroscience* **25**:223–232. doi:10.1523/JNEUROSCI.3688-04.2005

Brown TH, Wong RKS, Prince DA. 1979. Spontaneous miniature synaptic potentials in hippocampal neurons. *Brain Res* **177**:194–199. doi:https://doi.org/10.1016/0006-8993(79)90931-4

Clamann HP, Rioult-Pedotti MS, Luscher HR. 1991. The influence of noise on quantal EPSP size obtained by deconvolution in spinal motoneurons in the cat. *J Neurophysiol* **65**:67–75. doi:10.1152/jn.1991.65.1.67

Clements JD. 2003. Variance–mean analysis: a simple and reliable approach for investigating synaptic transmission and modulation. *J Neurosci Methods* **130**:115–125. doi:https://doi.org/10.1016/j.jneumeth.2003.09.019

Clements JD, Silver RA. 2000. Unveiling synaptic plasticity: a new graphical and analytical approach. *Trends Neurosci* **23**:105–113. doi:10.1016/S0166-2236(99)01520-9

del Castillo J, Katz B. 1954. Quantal components of the end-plate potential. *J Physiol* **124**:560–573. doi:https://doi.org/10.1113/jphysiol.1954.sp005129

Dervinis M, Major G. 2023. A novel method for reliably measuring miniature and spontaneous postsynaptic potentials/currents in whole-cell patch clamp recordings in the central nervous system. *bioRxiv*. doi:10.1101/2022.03.20.485046

Edwards FR, Redman SJ, Walmsley B. 1976. Statistical fluctuations in charge transfer at Ia synapses on spinal motoneurones. *J Physiol* **259**:665–688. doi:https://doi.org/10.1113/jphysiol.1976.sp011488

Enoki R, Hu Y, Hamilton D, Fine A. 2009. Expression of Long-Term Plasticity at Individual Synapses in Hippocampus Is Graded, Bidirectional, and Mainly Presynaptic: Optical Quantal Analysis. *Neuron* **62**:242–253. doi:10.1016/j.neuron.2009.02.026

Fatt P, Katz B. 1952. Spontaneous subthreshold activity at motor nerve endings. *J Physiol* **117**:109–128.

Forti L, Bossi M, Bergamaschi A, Villa A, Malgaroli A. 1997. Loose-patch recordings of single quanta at individual hippocampal synapses. *Nature* **388**:874–878. doi:10.1038/42251

Gentet LJ, Stuart GJ, Clements JD. 2000. Direct Measurement of Specific Membrane Capacitance in Neurons. *Biophys J* **79**:314–320. doi:https://doi.org/10.1016/S0006-3495(00)76293-X

Hardingham NR, Read JCA, Trevelyan AJ, Nelson JC, Jack JJB, Bannister NJ. 2010. Quantal Analysis Reveals a Functional Correlation between Presynaptic and Postsynaptic Efficacy in Excitatory Connections from Rat Neocortex. *The Journal of Neuroscience* **30**:1441–1451. doi:10.1523/JNEUROSCI.3244-09.2010

698 Hawkins J, Lewis M, Klukas M, Purdy S, Ahmad S. 2019. A Framework for Intelligence and Cortical
699 Function Based on Grid Cells in the Neocortex. *Front Neural Circuits* **12**.
700 doi:10.3389/fncir.2018.00121

701 Heuser JE, Reese TS, Dennis MJ, Jan Y, Jan L, Evans L. 1979. Synaptic vesicle exocytosis captured by
702 quick freezing and correlated with quantal transmitter release. *Journal of Cell Biology* **81**:275–
703 300. doi:10.1083/jcb.81.2.275

704 Isaacson JS, Walmsley B. 1995. Counting quanta: Direct measurements of transmitter release at a
705 central synapse. *Neuron* **15**:875–884. doi:10.1016/0896-6273(95)90178-7

706 Jack JJ, Redman SJ, Wong K. 1981. The components of synaptic potentials evoked in cat spinal
707 motoneurones by impulses in single group Ia afferents. *J Physiol* **321**:65–96.
708 doi:https://doi.org/10.1113/jphysiol.1981.sp013972

709 Jonas P, Major G, Sakmann B. 1993. Quantal components of unitary EPSCs at the mossy fibre
710 synapse on CA3 pyramidal cells of rat hippocampus. *J Physiol* **472**:615–663.
711 doi:https://doi.org/10.1113/jphysiol.1993.sp019965

712 Katz B. 1969. The Release of Neural Transmitter Substances. Liverpool: Liverpool Univ. Press.

713 Korn H, Faber DS. 1991. Quantal analysis and synaptic efficacy in the CNS. *Trends Neurosci* **14**:439–
714 445. doi:https://doi.org/10.1016/0166-2236(91)90042-S

715 Kraszewski K, Grantyn R. 1992. Unitary, quantal and miniature gaba-activated synaptic chloride
716 currents in cultured neurons from the rat superior colliculus. *Neuroscience* **47**:555–570.
717 doi:https://doi.org/10.1016/0306-4522(92)90165-X

718 Kullmann DM, Nicoll RA. 1992. Long-term potentiation is associated with increases in quantal
719 content and quantal amplitude. *Nature* **357**:240–244. doi:10.1038/357240a0

720 Kuno M. 1964. Quantal components of excitatory synaptic potentials in spinal motoneurones. *J*
721 *Physiol* **175**:81–99. doi:https://doi.org/10.1113/jphysiol.1964.sp007504

722 Larkman A, Stratford K, Jack J. 1991. Quantal analysis of excitatory synaptic action and depression in
723 hippocampal slices. *Nature* **350**:344–347. doi:10.1038/350344a0

724 Larkum ME, Nevian T, Sandler M, Polsky A, Schiller J. 2009. Synaptic Integration in Tuft Dendrites of
725 Layer 5 Pyramidal Neurons: A New Unifying Principle. *Science (1979)* **325**:756–760.
726 doi:10.1126/science.1171958

727 Lehmann J, Schneider J, McPherson S, Murphy DE, Bernard P, Tsai C, Bennett DA, Pastor G, Steel DJ,
728 Boehm C. 1987. CPP, a selective N-methyl-D-aspartate (NMDA)-type receptor antagonist:
729 characterization in vitro and in vivo. *Journal of Pharmacology and Experimental Therapeutics*
730 **240**:737–746.

731 Liu Z, Lu X, Villette V, Gou Y, Colbert KL, Lai S, Guan S, Land MA, Lee J, Assefa T, Zollinger DR,
732 Korympidou MM, Vlasits AL, Pang MM, Su S, Cai C, Froudarakis E, Zhou N, Patel SS, Smith CL,
733 Ayon A, Bizouard P, Bradley J, Franke K, Clandinin TR, Giovannucci A, Tolias AS, Reimer J,
734 Dieudonné S, St-Pierre F. 2022. Sustained deep-tissue voltage recording using a fast indicator
735 evolved for two-photon microscopy. *Cell* **185**:3408-3425.e29. doi:10.1016/J.CELL.2022.07.013

736 Major G. 1993a. Solutions for transients in arbitrarily branching cables: III. Voltage clamp problems.
737 *Biophys J* **65**:469–491. doi:10.1016/S0006-3495(93)81039-7

Major G. 1993b. Solutions for transients in arbitrarily branching cables: III. Voltage clamp problems. *Biophys J* **65**:469–491. doi:10.1016/S0006-3495(93)81039-7

Major G, Evans JD, Jack JJ. 1993. Solutions for transients in arbitrarily branching cables: I. Voltage recording with a somatic shunt. *Biophys J* **65**:423–449. doi:10.1016/S0006-3495(93)81037-3

Major G, Larkum ME, Schiller J. 2013a. Active Properties of Neocortical Pyramidal Neuron Dendrites. *Annu Rev Neurosci* **36**:1–24. doi:10.1146/annurev-neuro-062111-150343

Major G, Larkum ME, Schiller J. 2013b. Active Properties of Neocortical Pyramidal Neuron Dendrites. *Annu Rev Neurosci* **36**:1–24. doi:10.1146/annurev-neuro-062111-150343

Nevian T, Larkum ME, Polsky A, Schiller J. 2007. Properties of basal dendrites of layer 5 pyramidal neurons: a direct patch-clamp recording study. *Nat Neurosci* **10**:206–214. doi:10.1038/nn1826

Oertner TG, Sabatini BL, Nimchinsky EA, Svoboda K. 2002. Facilitation at single synapses probed with optical quantal analysis. *Nat Neurosci* **5**:657–664. doi:10.1038/nn867

Peled ES, Isacoff EY. 2011. Optical quantal analysis of synaptic transmission in wild-type and rab3-mutant Drosophila motor axons. *Nat Neurosci* **14**:519–526. doi:10.1038/nn.2767

Pircher T, Pircher B, Feigenspan A. 2022. A novel machine learning-based approach for the detection and analysis of spontaneous synaptic currents. *PLoS One* **17**:1–16. doi:10.1371/journal.pone.0273501

Rall W. 1977. Core Conductor Theory and Cable Properties of Neurons In: Kandel ER, Brookhardt JM, Mountcastle VM, editors. Handbook of Physiology, Cellular Biology of Neurons. Bethesda, MD: American Physiological Society. pp. 39–97.

Rall W, Segev I. 1985. Space-clamp problems when voltage clamping branched neurons with intracellular microelectrodes In: T. G. Smith Jr, Lecar H, Redman SJ, Gage P, editors. Voltage and Patch Clamping with Microelectrodes. Bethesda, MD: American Physiological Society. pp. 191–215.

Randle JCR, Guet T, Cordi A, Lepagnol JM. 1992. Competitive inhibition by NBQX of kainate/AMPA receptor currents and excitatory synaptic potentials: importance of 6-nitro substitution. *Eur J Pharmacol* **215**:237–244. doi:https://doi.org/10.1016/0014-2999(92)90033-Z

Redman S. 1990. Quantal analysis of synaptic potentials in neurons of the central nervous system. *Physiol Rev* **70**:165–198. doi:10.1152/physrev.1990.70.1.165

Reid CA, Clements JD. 1999. Postsynaptic expression of long-term potentiation in the rat dentate gyrus demonstrated by variance-mean analysis. *J Physiol* **518**:121–130. doi:https://doi.org/10.1111/j.1469-7793.1999.0121r.x

Sahara Y, Takahashi T. 2001. Quantal components of the excitatory postsynaptic currents at a rat central auditory synapse. *J Physiol* **536**:189–197. doi:https://doi.org/10.1111/j.1469-7793.2001.00189.x

Silver RA. 2003. Estimation of nonuniform quantal parameters with multiple-probability fluctuation analysis: theory, application and limitations. *J Neurosci Methods* **130**:127–141. doi:https://doi.org/10.1016/j.jneumeth.2003.09.030

776 Spruston N, Jaffe DB, Williams SH, Johnston D. 1993. Voltage- and space-clamp errors associated
777 with the measurement of electrotonically remote synaptic events. *J Neurophysiol* **70**:781–802.
778 doi:10.1152/jn.1993.70.2.781

779 Stern P, Edwards FA, Sakmann B. 1992. Fast and slow components of unitary EPSCs on stellate cells
780 elicited by focal stimulation in slices of rat visual cortex. *J Physiol* **449**:247–278.
781 doi:https://doi.org/10.1113/jphysiol.1992.sp019085

782 Stuart G, Spruston N. 1998. Determinants of Voltage Attenuation in Neocortical Pyramidal Neuron
783 Dendrites. *The Journal of Neuroscience* **18**:3501–3510. doi:10.1523/JNEUROSCI.18-10-
784 03501.1998

785 Vere-Jones D. 1966. SIMPLE STOCHASTIC MODELS FOR THE RELEASE OF QUANTA OF TRANSMITTER
786 FROM A NERVE TERMINAL. *Australian Journal of Statistics* **8**:53–63.
787 doi:https://doi.org/10.1111/j.1467-842X.1966.tb00164.x

788 Wall MJ, Usowicz MM. 1998. Development of the quantal properties of evoked and spontaneous
789 synaptic currents at a brain synapse. *Nat Neurosci* **1**:675–682. doi:10.1038/3677

790 Wang N-S, Marino M, Malinow R. 2024. Detecting unitary synaptic events with machine learning.
791 *Proceedings of the National Academy of Sciences* **121**:e2315804121.
792 doi:10.1073/pnas.2315804121

793 Williams SR, Mitchell SJ. 2008. Direct measurement of somatic voltage clamp errors in central
794 neurons. *Nat Neurosci* **11**:790–798. doi:10.1038/nn.2137

795 Williams SR, Stuart GJ. 2002. Dependence of EPSP Efficacy on Synapse Location in Neocortical
796 Pyramidal Neurons. *Science (1979)* **295**:1907–1910. doi:10.1126/science.1067903

797 Yuste R. 2010. Dendritic Spines. The MIT Press. doi:10.7551/mitpress/9780262013505.001.0001

798 Yuste R, Majewska A, Cash SS, Denk W. 1999. Mechanisms of Calcium Influx into Hippocampal
799 Spines: Heterogeneity among Spines, Coincidence Detection by NMDA Receptors, and Optical
800 Quantal Analysis. *The Journal of Neuroscience* **19**:1976–1987. doi:10.1523/JNEUROSCI.19-06-
801 01976.1999

802

803

Figures

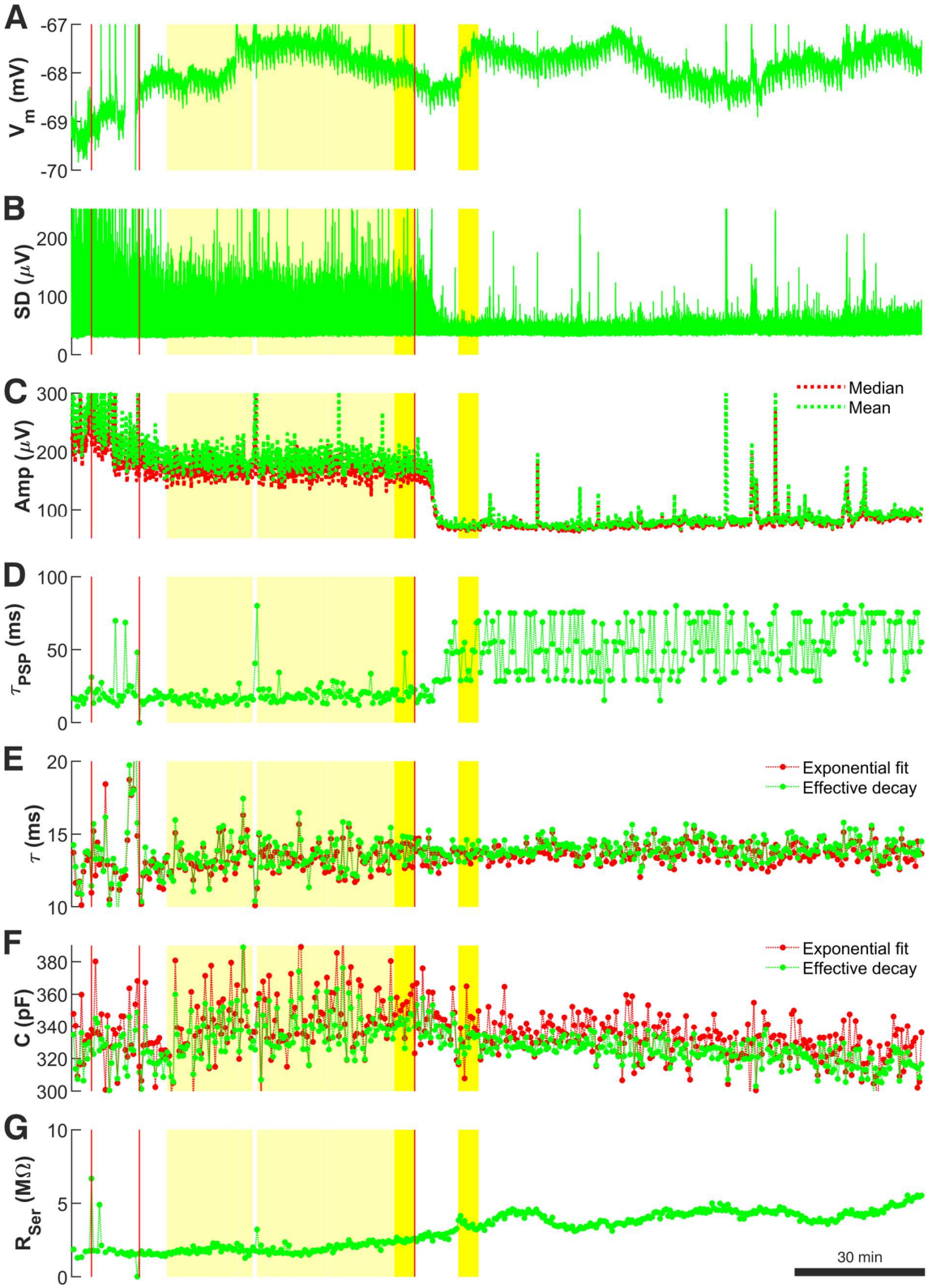

Figure 1: Recording quality measures used during the data preprocessing stage to select 'noise with minis' and 'noise-alone' recording sweeps for further data analysis for recording p103a (layer 5).

808 (A) Baseline V_m across the entire recording session. Stimulation pulses were excluded from the
809 display. The total recording duration (excluding pulse periods) was 8520 s. The first red vertical line
810 marks the time when pharmacological blockade of APs was initiated. The second red vertical line
811 marks the time when no more APs were observing in the recording. The third red vertical line marks
812 the time when pharmacological blockade of mEPSPs was initiated. Bright yellow periods mark 'noise
813 with minis' and 'noise-alone' recording segments selected as the main comparison file for the
814 distribution fitting. Light yellow marks all the remaining good quality 'noise with minis' recording
815 sweeps that were also included in the distribution fitting procedure for estimating target SAD, MAD,
816 and 'deviation' scores.
817 (B) V_m standard deviation measured over consecutive 15 ms windows over the same recording
818 session. The meaning of symbols is the same as in panel (A).
819 (C) Evolution of mean and median amplitudes of the top 10% (amplitude-wise) of all detected events
820 (including minis and noise events with similar rise times), averaged over single sweeps across the
821 entire recording session.
822 (D) Effective decay time constants (time to drop to 1/e of value) of the same top 10% (amplitude-
823 wise) of detected events as in panel (C) averaged over consecutive 20-second-long segments across
824 the same session. Once minis blocked pharmacologically, effective time constant of detected events
825 (now pure noise) increases, so this is another useful measure of when the block is complete.
826 (E) Evolution of passive membrane time constant over the entire recording session. Measurements
827 were averaged over consecutive 20-second-long segments. Measurements based on exponential
828 decay curve fit and on 'effective time constant' (time for V_m to drop to 1/e of a value just after
829 change in current (after pipette capacitance artefact and charge redistribution).
830 (F) Evolution of total cell membrane capacitance across the recording session. Measurements were
831 averaged over consecutive 20-second-long segments. Measurements based on exponential decay
832 curve fit and on effective time constant (time taken for V_m drop to 1/e of an initial value).

833 (G) Evolution of whole-cell pipette series resistance (bridge balance error) across the recording

834 session. Measurements were averaged over consecutive 20-second-long segments.

835

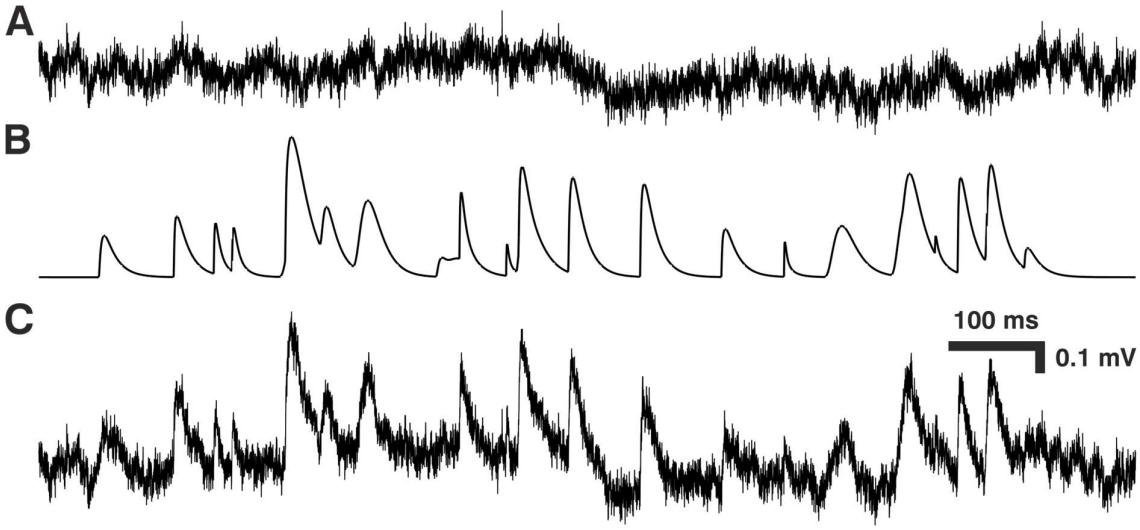

Figure 2: Constructing ’noise with simulated minis’ voltage trace.

(A) A segment of ‘noise-alone’ recording that was used to produce the voltage trace in (C). The noise recording was obtained from a cortical layer 2/3 pyramidal neuron (cell p131a).

(B) A voltage trace showing simulated mEPSPs only that were added to noise-alone recording in (A) to produce the ‘real noise with simulated mEPSPs’ voltage trace in (C).

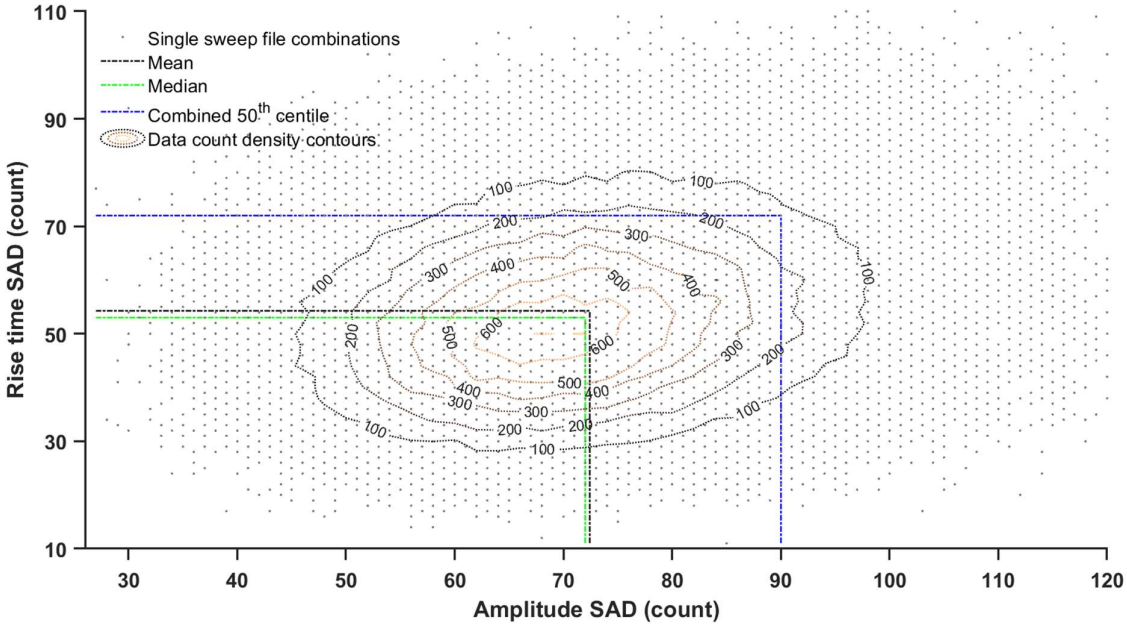

Figure 3: Amplitude and rise time scattergram (density plot) of sum of absolute deviation (SAD) scores between histograms from all possible pairs of 'noise with minis' single sweep files from a layer 5 pyramidal neuron (p103a) recording.

The line marking combined 50th centile cutoff is based on 15 different SAD, SSD, and MAD scores as explained in Tables 1 and 2 (it extends to the remaining 13 dimensions not shown here). '15-score combined 50th centile' sets a lower (more exacting) threshold for accepting distribution fits than the mean or the median would. This is justified because distribution fits need to satisfy all 15 SAD, SSD, and MAD scores simultaneously (e.g. to ensure that one of the tails of the distribution is not badly fit, as well as the remaining parts of the distribution).

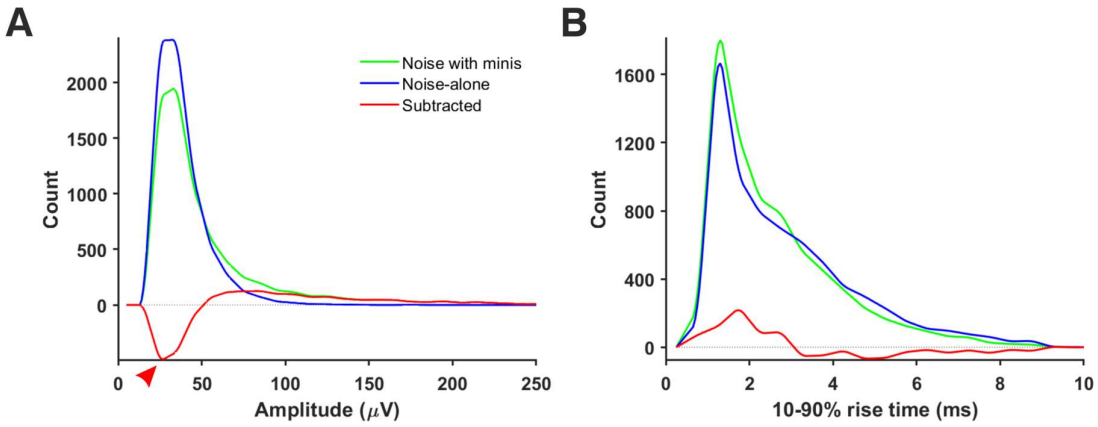

Figure 4: Amplitude and rise time distributions of detected minis-like events in ’noise with minis’ and ’noise-alone’ recordings.

(A) Amplitude distributions of detected minis-like events in ’noise with minis’ and ’noise-alone’ recordings (“thick” tufted neocortical layer 5 pyramidal neuron p108b). Red arrowhead indicates negative bins after subtracting ‘noise-alone’ distribution from ‘noise with minis’ distribution.

(B) 10-90% rise time distributions of detected minis-like events in ’noise with minis’ and ’noise-alone’ recordings.

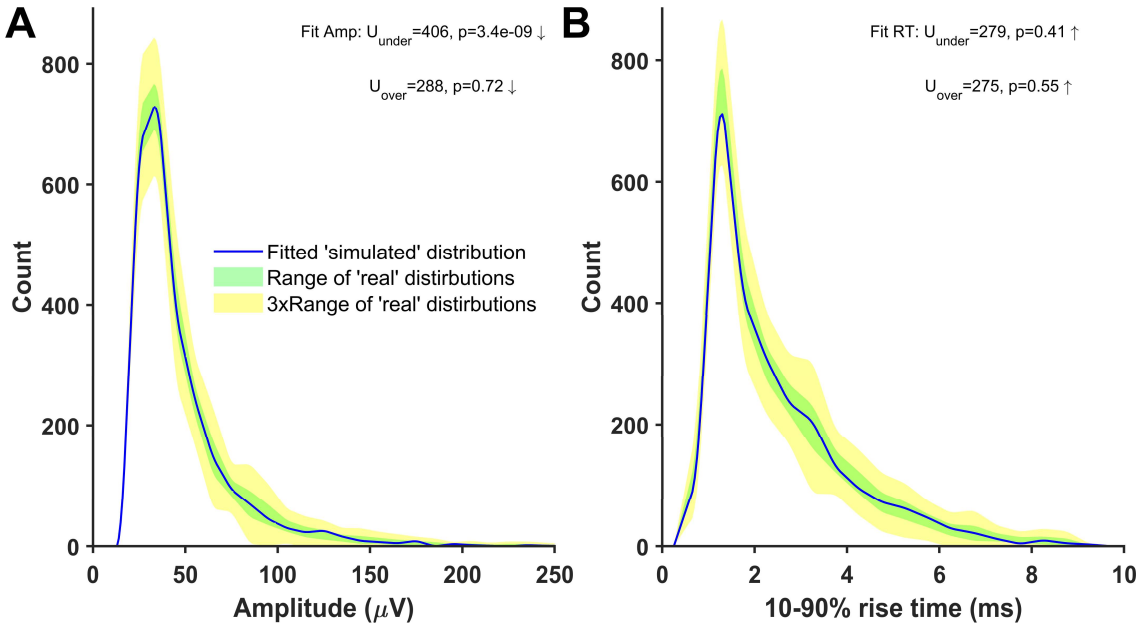

Figure 5: Distributions of minis-like events detected in a ’noise with simulated minis’ voltage trace closely matching ‘noise with real minis‘ recordings.

Parameters of simulated minis were controlled by the Genetic Algorithm; ‘noise with real minis’ and ’noise-alone’ recordings from neocortical layer 5 cell (p106b). Upward arrows indicate ‘simulated’ SAD > ‘real’ SAD relationship and downward arrows indicate ‘simulated’ SAD < ‘real’ SAD relationship. The underfit test involves a comparison with the worst-performing ‘real’ SAD, whereas the overfit test involves a comparison with the best-performing ‘real’ SAD.

(A) Amplitude and (B) 10-90% rise time distributions (blue) of minis-like events detected in a ’noise with simulated minis’ voltage trace.

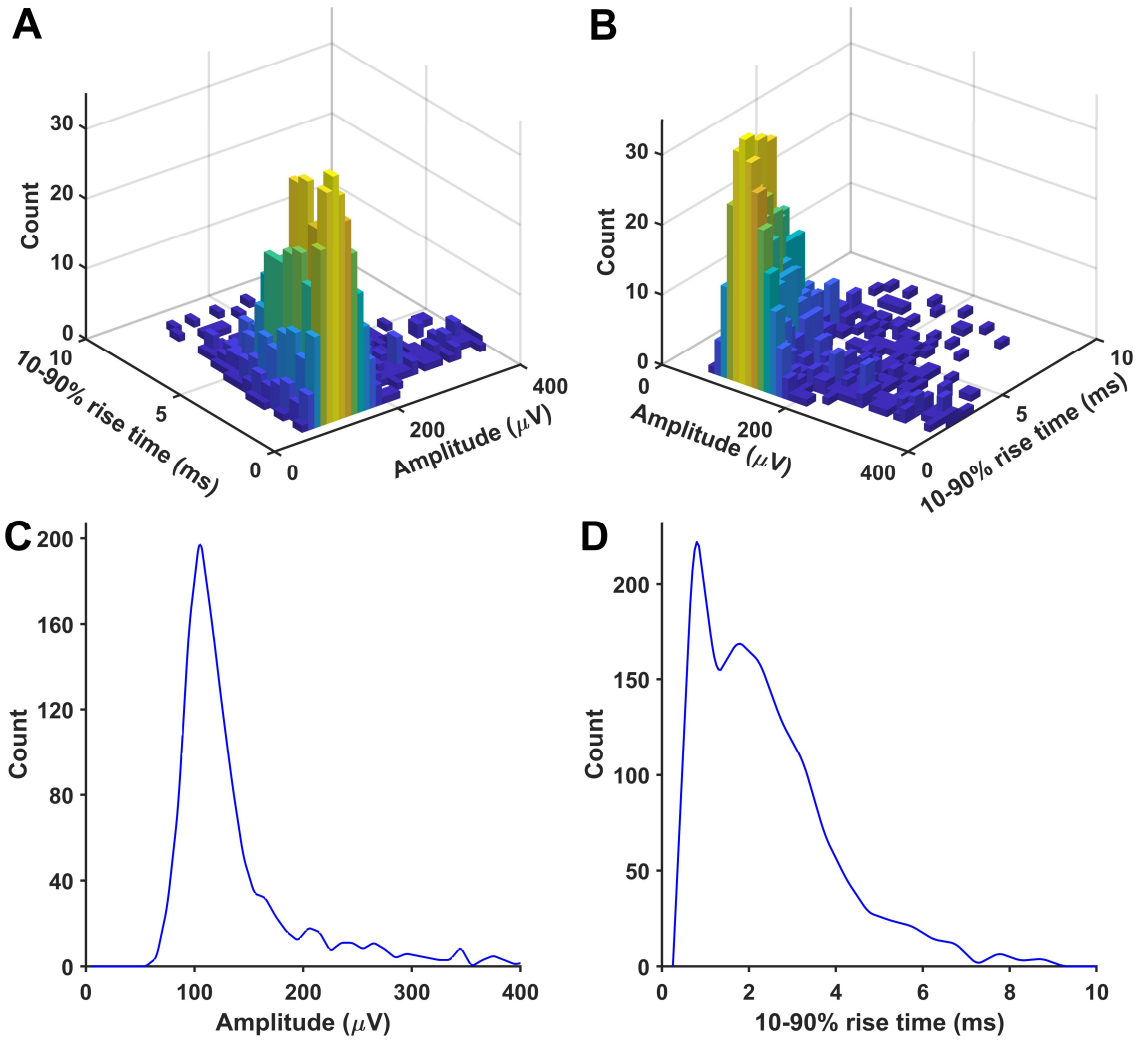

Figure 6: An example of simulated minis distribution that was used to produce a close match between distributions of detected minis-like events in a 'noise with simulated minis' voltage trace and a 'noise with real minis' recording for a neocortical layer 2/3 cell (p131c).

(A) Joint amplitude and 10-90% rise time distribution of simulated minis; (B) viewed from different angle.

(C) and (D) Corresponding marginal ('one-dimensional') amplitude and 10-90% rise time distributions.

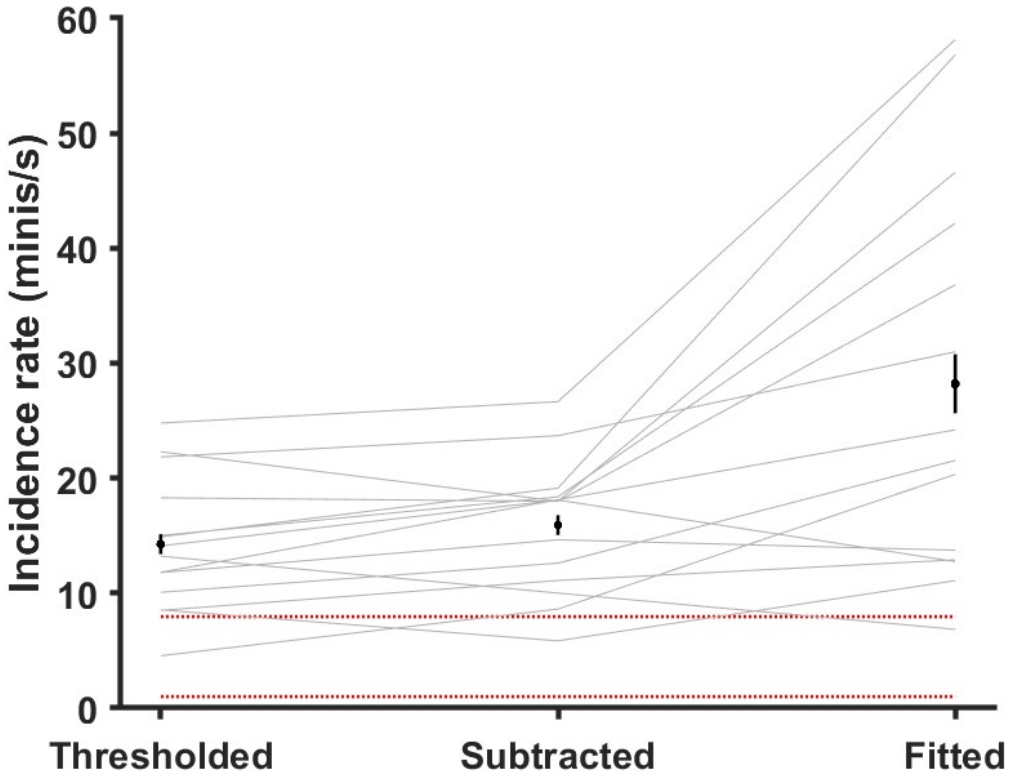

Figure 7: Estimated minis incidence rates using various methods (grey lines are individual cells). 'Thresholded' method: an 'unreasonably high' 0.8 mV detection threshold was applied to all 14 'noise with real minis' recordings and only events with larger amplitudes were included in the estimate.
'Subtracted' method: Distribution of minis-like events in the 'noise-alone' recording was subtracted from the distribution of minis-like events in the 'noise with real minis' recording and the incidence rate estimate was based on the remaining distribution.
'Fitted' method: Simulated minis distribution was used to estimate the minis' incidence rate (lowest acceptable rate consistent with the real experimental data).
Black markers and black vertical lines correspond to means and 95% confidence intervals. Red dotted lines mark the range of incidence rates typically reported in the literature and discussed in the companion article (Dervinis and Major, 2023).

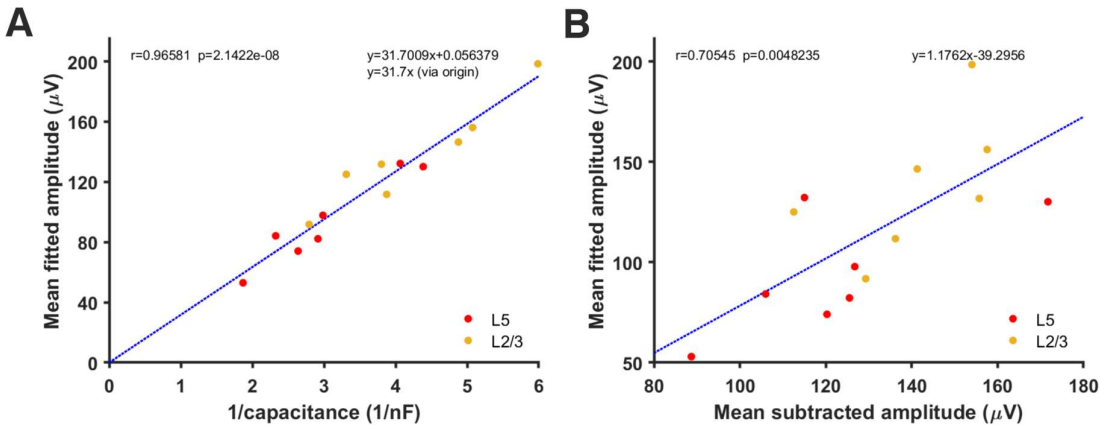

Figure 8: Relationship between cell's inverse total capacitance and estimated mean minis amplitude using simulations of minis and minis' distribution fitting.

(A) Correlation between mean minis amplitudes as derived using simulated minis' distribution fitting method and the inverse of cell's total capacitance. The blue line is the least square fit to the data while the black line is the fit to the data that passes through the origin of the axes.

(B) Correlation between the 'subtracted' mean minis amplitude as shown in Figure 4 and the 'fitted' mean minis amplitude.

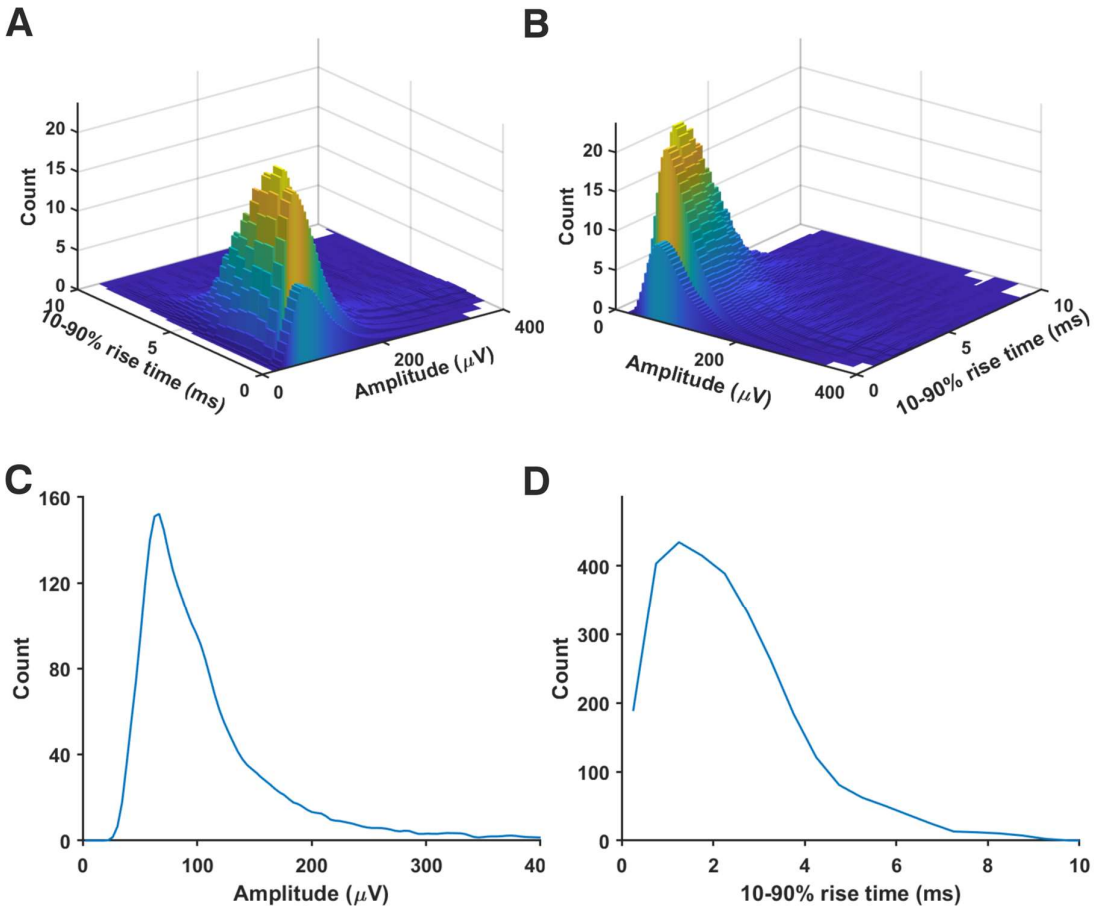

Figure 9: Generic 'averaged' mEPSP distribution from rat (somatosensory) neocortical pyramidal neurons.

Distributions resulting from all 14 recordings were averaged and the resulting distribution was smoothed. All minis' amplitudes were normalised by means of their respective source distributions.

(A) A joint amplitude and 10-90% rise time distribution of simulated minis.

(B) The same distribution but viewed from a different angle.

(C) Marginal (1-dimensional) amplitude distribution of the same distribution as in (A).

(D) Marginal 10-90% rise time distribution of the same distribution as in (A).

Tables

Amp SAD ≤56th centile?	Top 50% amp SAD ≤56th centile?	Top 10% amp SAD ≤56th centile?	Top 2% amp SAD ≤56th centile?	Top 50% amp SSD ≤0?	Top 10% amp SSD ≤0?	Top 2% amp SSD ≤0?	RT SAD ≤56th centile?	Joint SAD ≤56th centile?	Amp MAD ≤56th centile?	Top 50% amp MAD ≤56th centile?	Top 10% amp MAD ≤56th centile?	Top 2% amp MAD ≤56th centile?	RT MAD ≤56th centile?	Joint MAD ≤56th centile?
…	…	…	…	…	…	…	…	…	…	…	…	…	…	…
Yes	Yes	Yes	Yes	No	No	No	Yes	Yes	Yes	Yes	Yes	Yes	Yes	Yes
Yes	Yes	Yes	Yes	Yes	Yes	Yes	Yes	Yes	Yes	Yes	Yes	Yes	Yes	Yes
Yes	Yes	Yes	Yes	No	No	No	Yes	Yes	Yes	Yes	Yes	Yes	Yes	Yes
No	No	No	No	Yes	No	No	Yes	Yes	Yes	No	No	No	Yes	Yes
No	Yes	No	No	No	Yes	Yes	Yes	Yes	Yes	Yes	No	No	Yes	No
Yes	Yes	Yes	Yes	No	No	No	No	Yes	Yes	Yes	Yes	Yes	No	Yes
…	…	…	…	…	…	…	…	…	…	…	…	…	…	…

Table 1: Failed hypothetical attempt to use 56th centile as a basis for the combined '15-score 50th centile'.

The table shows representative portion of a much bigger table illustrating a hypothetical scenario where the 15 SAD, SSD, and MAD scores are arranged in columns and rows correspond to different two-file combinations (many other combinations above and below those portrayed for the sake of the argument). SAD, SSD, and MAD scores are calculated by subtracting one file distribution from another (see the text for a detailed explanation). In this example only a single file combination (green; 1/6 = 16.7%; row shaded in grey) satisfies the condition of having all SAD, SSD, and MAD values that are equal or below the 56th centile value of its respective SAD, SSD, and MAD scores (unique per column) *simultaneously* in all columns. Therefore, the 56th percentile of each SAD, SSD, and MAD score would be too small to serve as the basis for the composite, joint or combined '15-score 50th centile': we need half the rows to be green, i.e. to pass the test.

Amp SAD ≤90th centile?	Top 50% amp SAD ≤90th centile?	Top 10% amp SAD ≤90th centile?	Top 2% amp SAD ≤90th centile?	Top 50% amp SSD ≤0?	Top 10% amp SSD ≤0?	Top 2% amp SSD ≤0?	RT SAD ≤90th centile?	Joint SAD ≤90th centile?	Amp MAD ≤90th centile?	Top 50% amp MAD ≤90th centile?	Top 10% amp MAD ≤90th centile?	Top 2% amp MAD ≤90th centile?	RT MAD ≤90th centile?	Joint MAD ≤90th centile?
…	…	…	…	…	…	…	…	…	…	…	…	…	…	…
Yes	Yes	Yes	Yes	Yes	Yes	Yes	Yes	Yes	Yes	Yes	No	No	No	Yes
Yes	Yes	Yes	Yes	Yes	Yes	Yes	Yes	Yes	Yes	Yes	Yes	Yes	Yes	Yes
Yes	Yes	Yes	Yes	Yes	Yes	Yes	Yes	Yes	Yes	Yes	Yes	Yes	Yes	Yes
Yes	Yes	Yes	Yes	Yes	Yes	Yes	Yes	Yes	Yes	Yes	Yes	Yes	Yes	No
Yes	Yes	Yes	Yes	Yes	Yes	Yes	Yes	Yes	Yes	Yes	Yes	Yes	No	No
Yes	Yes	Yes	Yes	Yes	Yes	Yes	Yes	Yes	Yes	Yes	Yes	Yes	Yes	Yes
…	…	…	…	…	…	…	…	…	…	…	…	…	…	…

Table 2: Using 90th SAD centile as a basis for the combined '15-score 50th centile'.

The table shows an example where the 15 SAD, SSD, and MAD scores are arranged in columns and rows correspond to different 2-file combinations. SAD, SSD, and MAD scores are calculated by subtracting one file distribution from another (see the text for a detailed explanation). Now *three* of the six file combinations (half of them: green; rows shaded in grey) satisfy the condition of having all SAD, SSD, and MAD values that are equal or below the 90th centile value of its respective SAD, SSD, and MAD scores (unique per column) simultaneously in all columns. Therefore the 90th percentile works as the basis for the combined '15-score 50th centile'. Higher than 90 leads to more than half and lower than 90 leads to fewer than half of file pair combinations 'passing' all 15 tests simultaneously.

Supplementary Figures

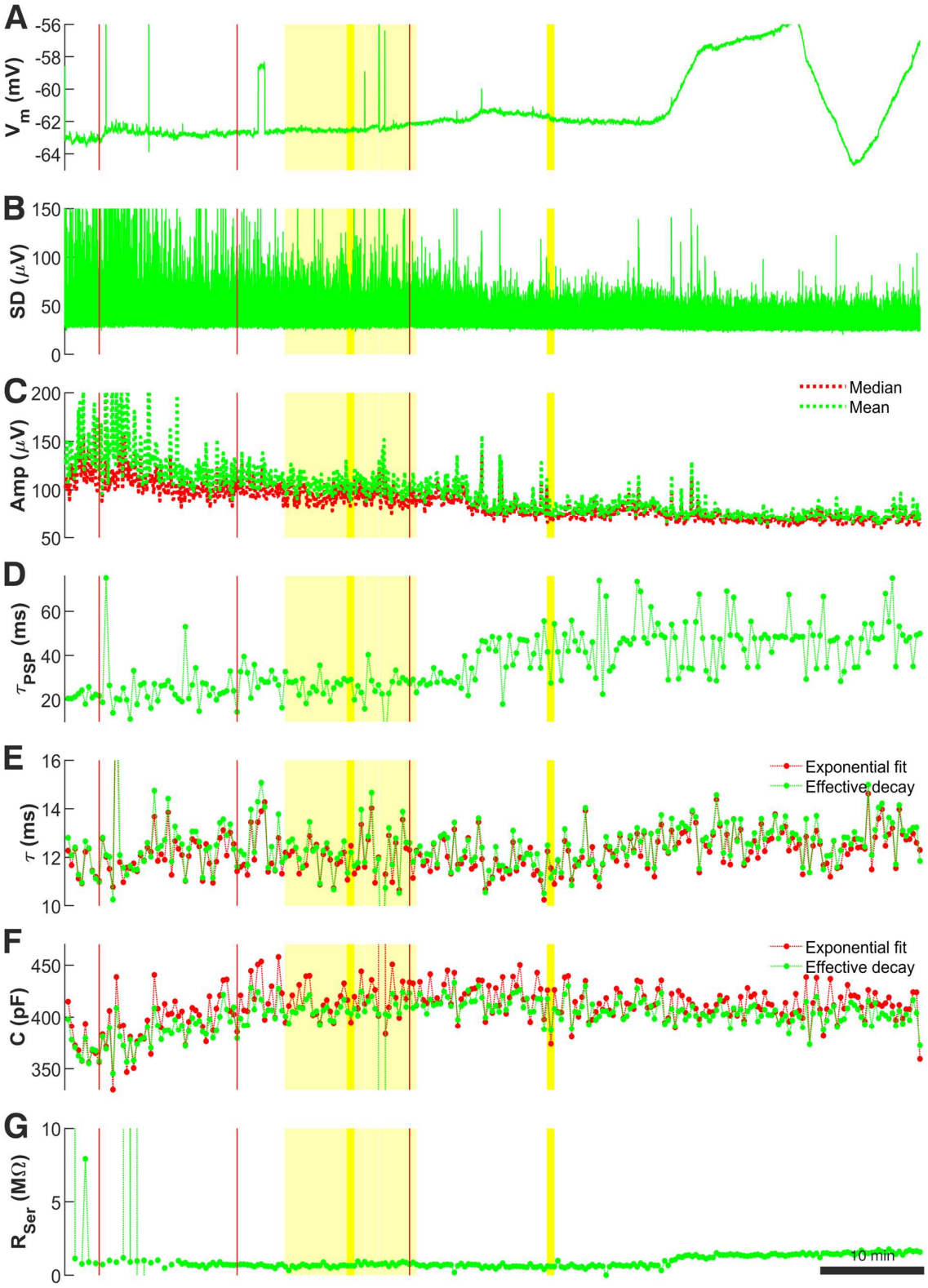

Supplementary Figure 1: Recording quality measures used during the data preprocessing stage to

935 select ’noise with minis’ and ’noise-alone’ recording sweeps for further data analysis for recording
936 p106b (layer 5).
937 (A) Baseline V_m across the entire recording session. The raw trace is very similar to the smoothed
938 one and, therefore, is occluded by the latter. Stimulation pulses were excluded from the display. The
939 total recording duration (excluding pulse periods) was 4960 s. The first red vertical line marks the
940 time when pharmacological blockade of APs was initiated. The second red vertical line marks the
941 time when no more APs were observing in the recording. The third red vertical line marks the time
942 when pharmacological blockade of mEPSPs was initiated. Bright yellow periods mark ‘noise with
943 minis’ and ‘noise-alone’ recording segments selected as the main comparison file for the distribution
944 fitting. Light yellow marks all the remaining good quality ‘noise with minis’ recording sweeps that
945 were also included in the distribution fitting procedure for estimating target SAD, MAD, and
946 ‘deviation’ scores.
947 (B) V_m standard deviation measured over consecutive 15 ms windows over the same recording
948 session. The meaning of symbols is the same as in panel (A).
949 (C) Evolution of mean and median amplitudes of the top 10% (amplitude-wise) of all detected minis-
950 like events averaged over single sweeps across the entire recording session.
951 (D) Effective decay (drop to 1/e of the peak value) time constants of the same top 10% (amplitude-
952 wise) of detected events as in panel (C) averaged over consecutive 20-second-long segments across
953 the same session.
954 (E) Evolution of passive membrane time constant over the entire recording session. Measurements
955 were averaged over consecutive 20-second-long segments. Both measurements based on
956 exponential decay curve fit and on effective V_m drop to 1/e of the initial value were calculated and
957 displayed.
958 (F) Evolution of total cell’s membrane capacitance across the recording session. Measurements were
959 averaged over consecutive 20-second-long segments. Both measurements based on exponential
960 decay curve fit and on effective V_m drop to 1/e of the initial value were calculated and displayed.

961 (G) Evolution of cell's input resistance (the bridge balance error) across the recording session.

962 Measurements were averaged over consecutive 20-second-long segments.

963

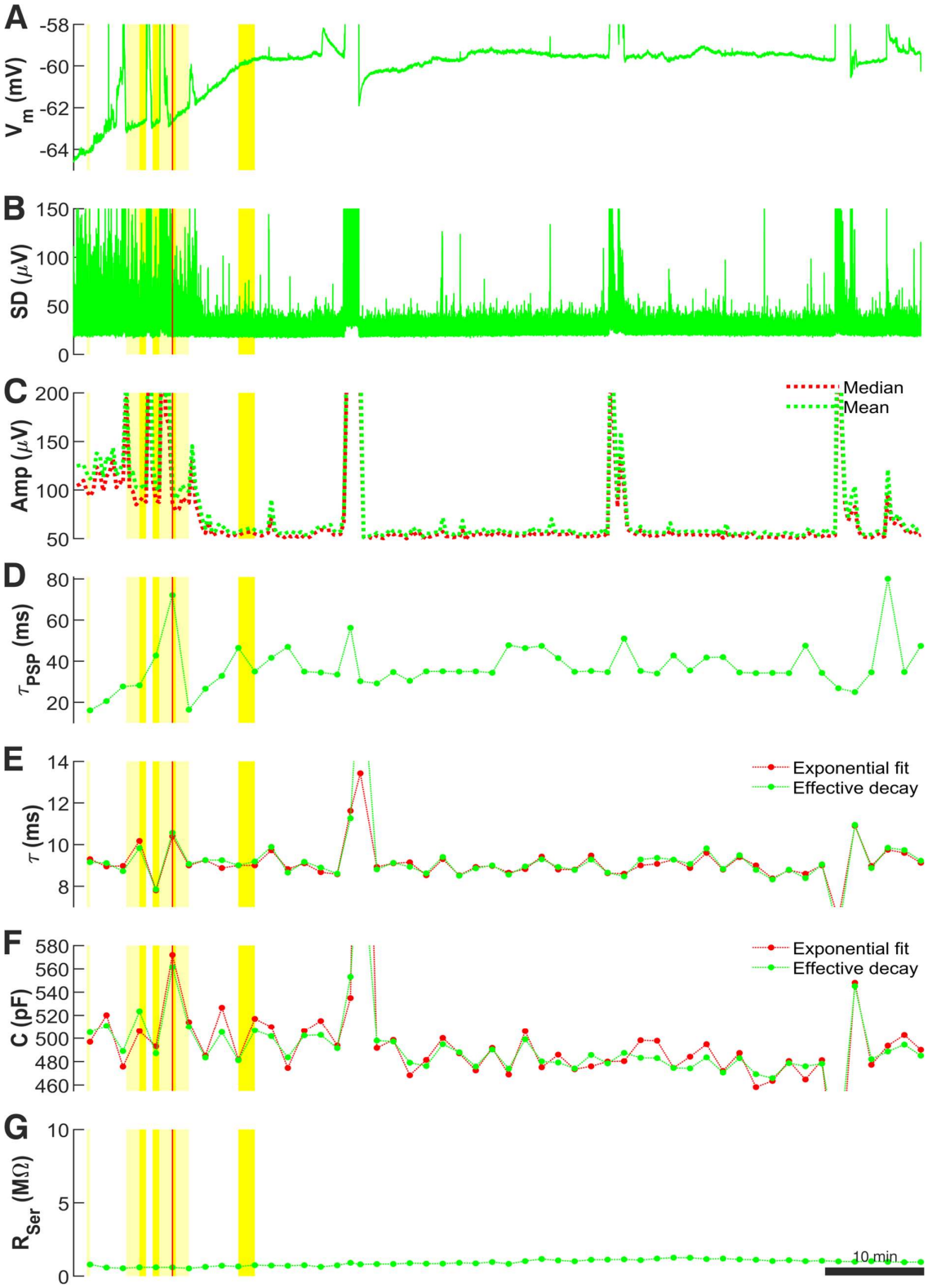

964

965 **Supplementary Figure 2:** Recording quality measures used during the data preprocessing stage to

select ’noise with minis’ and ’noise-alone’ recording sweeps for further data analysis for recording p108a (layer 5).

The meaning of panels A-G is explained in Supplementary figure 1 except for data being averaged over 100-second-long windows in panels D-G. The figure shows only part of the recording following the blockade of APs with only a single red vertical time marker visible indicating the time when pharmacological EPSP blockers were infused. The total duration of the recording shown in the figure was 5140 s.

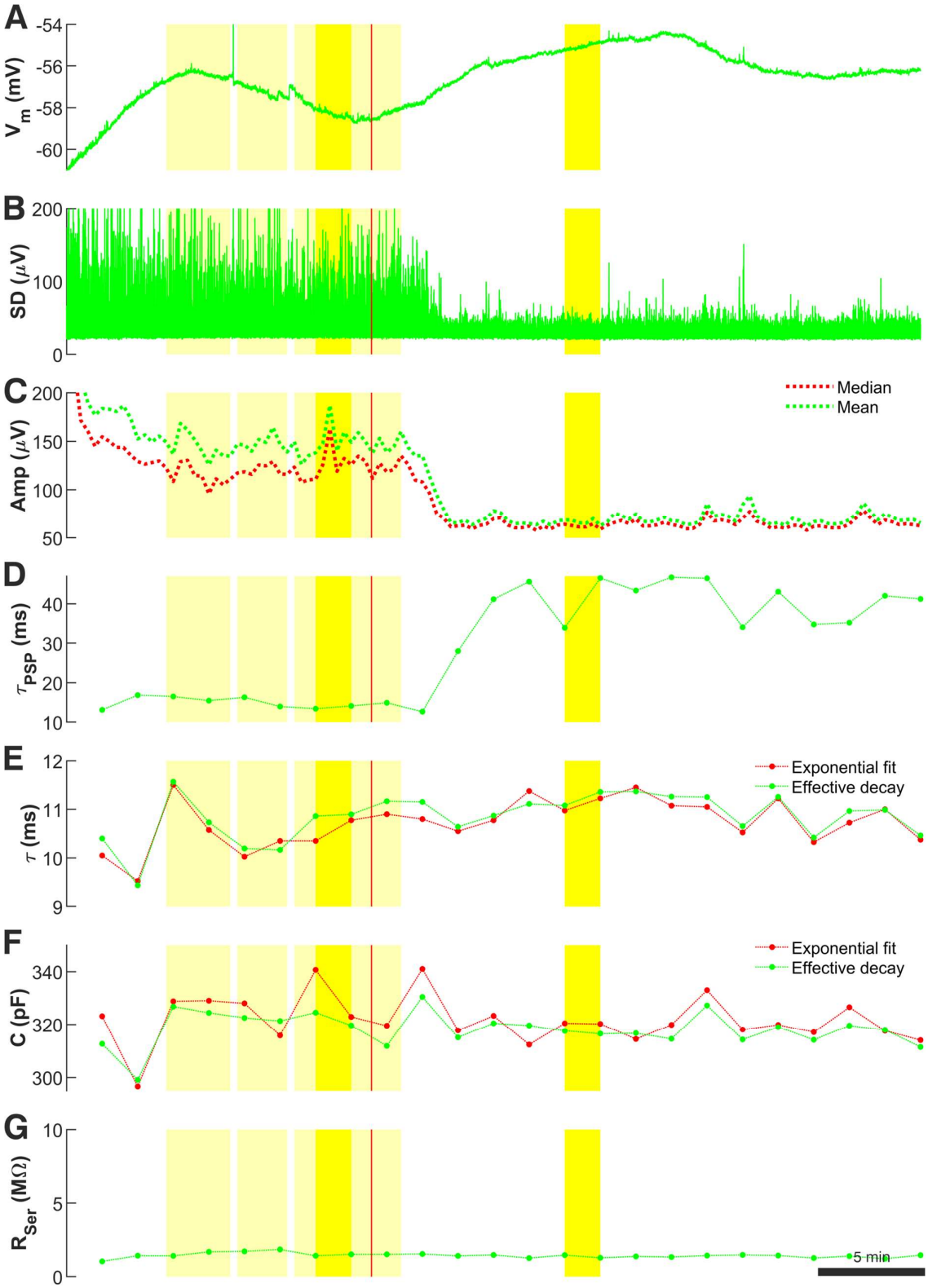

Supplementary Figure 3: Recording quality measures used during the data preprocessing stage to

select ’noise with minis’ and ’noise-alone’ recording sweeps for further data analysis for recording p108b (layer 5).

The meaning of panels A-G is explained in Supplementary figure 1 except for data being averaged over 100-second-long windows in panels D-G. The figure shows only part of the recording following the blockade of APs with only a single red vertical time marker visible indicating the time when pharmacological EPSP blockers were infused. The total duration of the recording shown in the figure was 2400 s.

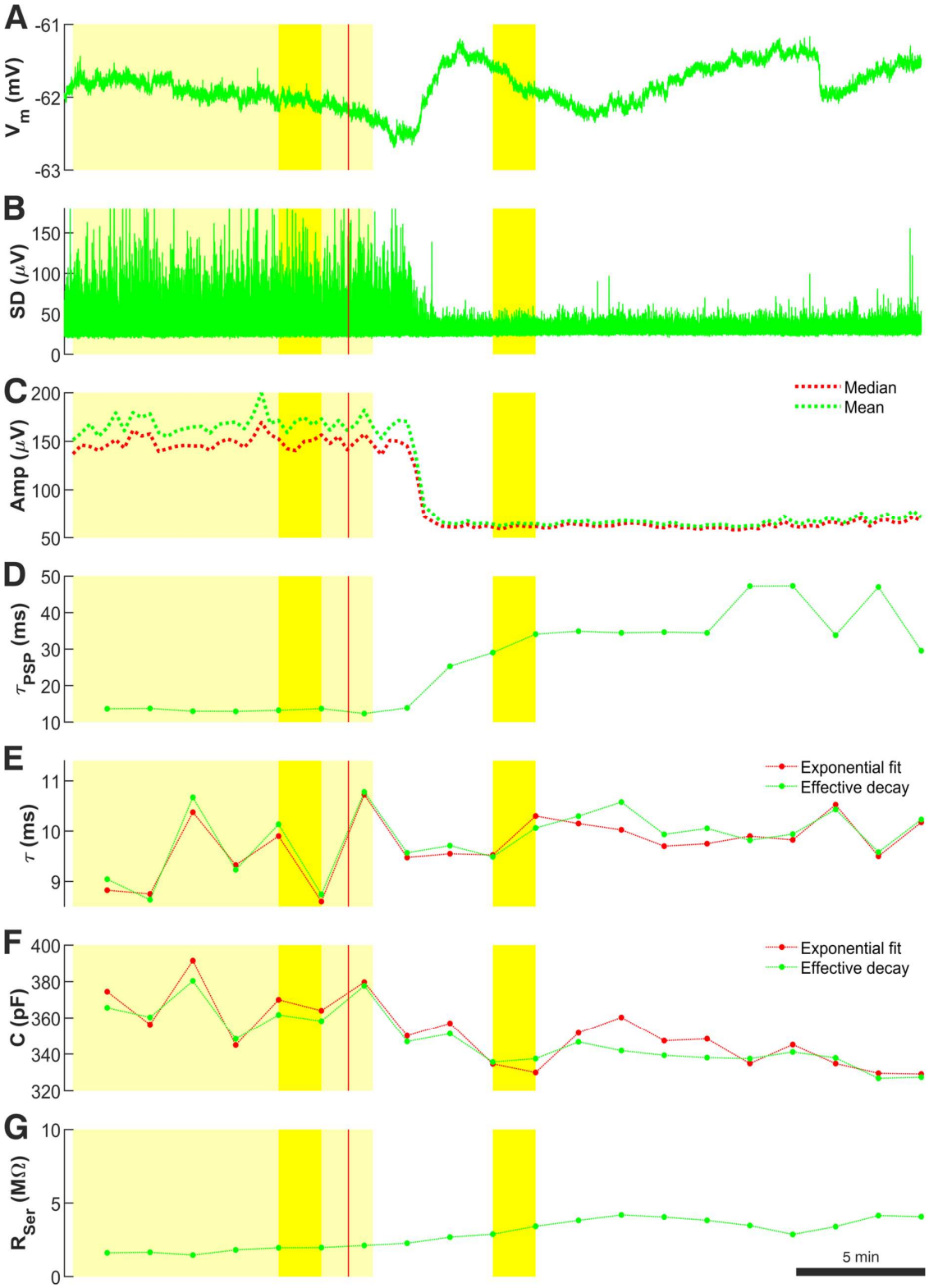

984

985 **Supplementary Figure 4:** Recording quality measures used during the data preprocessing stage to

select ’noise with minis’ and ’noise-alone’ recording sweeps for further data analysis for recording p108c (layer 5).

The meaning of panels A-G is explained in Supplementary figure 1 except for data being averaged over 100-second-long windows in panels D-G. The figure shows only part of the recording following the blockade of APs with only a single red vertical time marker visible indicating the time when pharmacological EPSP blockers were infused. The total duration of the recording shown in the figure was 2000 s.

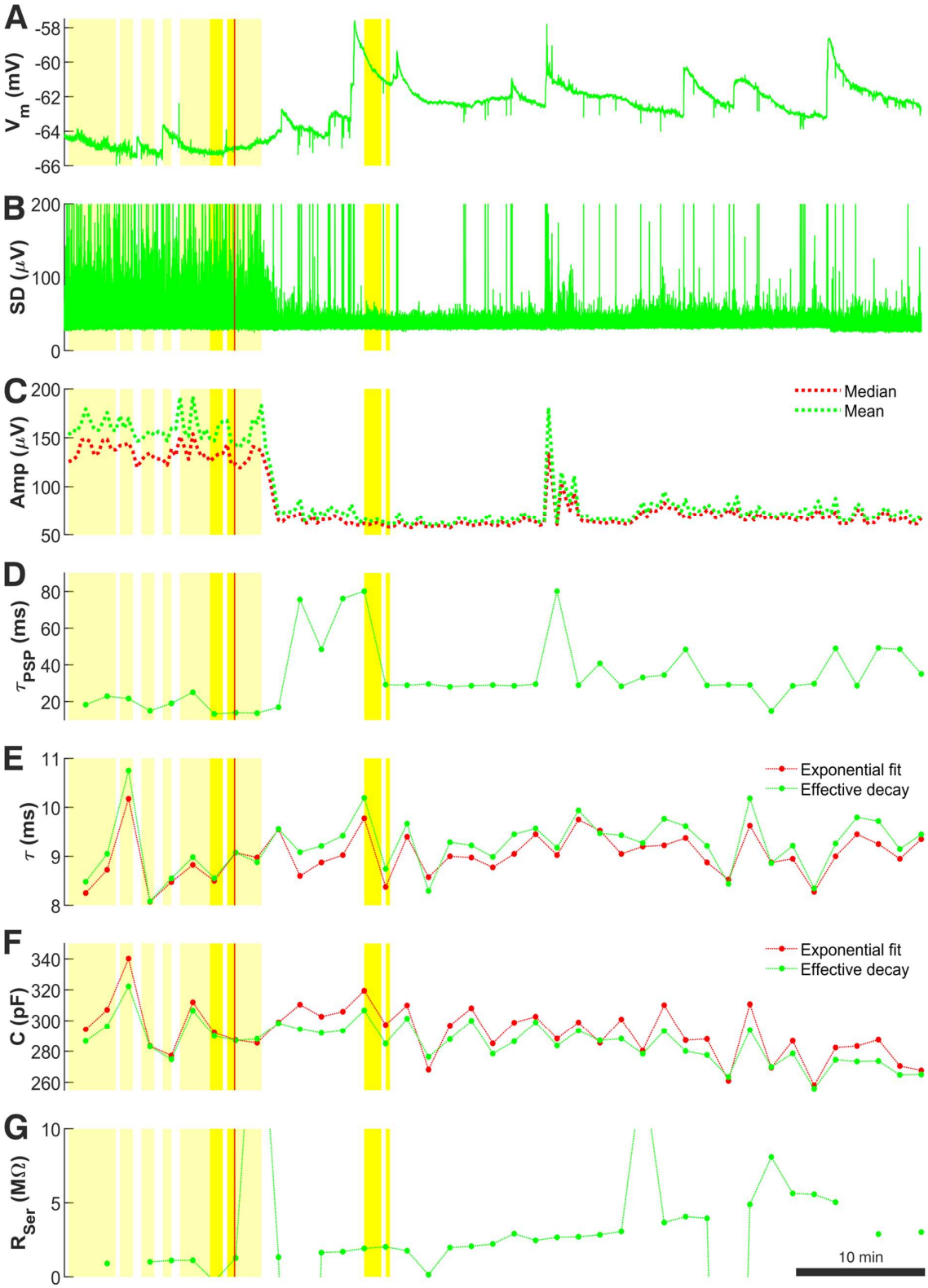

994

995 **Supplementary Figure 5:** Recording quality measures used during the data preprocessing stage to

select ’noise with minis’ and ’noise-alone’ recording sweeps for further data analysis for recording p120b (layer 2/3).

The meaning of panels A-G is explained in Supplementary figure 1 except for data being averaged over 100-second-long windows in panels D-G. The figure shows only part of the recording following the blockade of APs with only a single red vertical time marker visible indicating the time when pharmacological EPSP blockers were infused. The total duration of the recording shown in the figure was 4000 s.

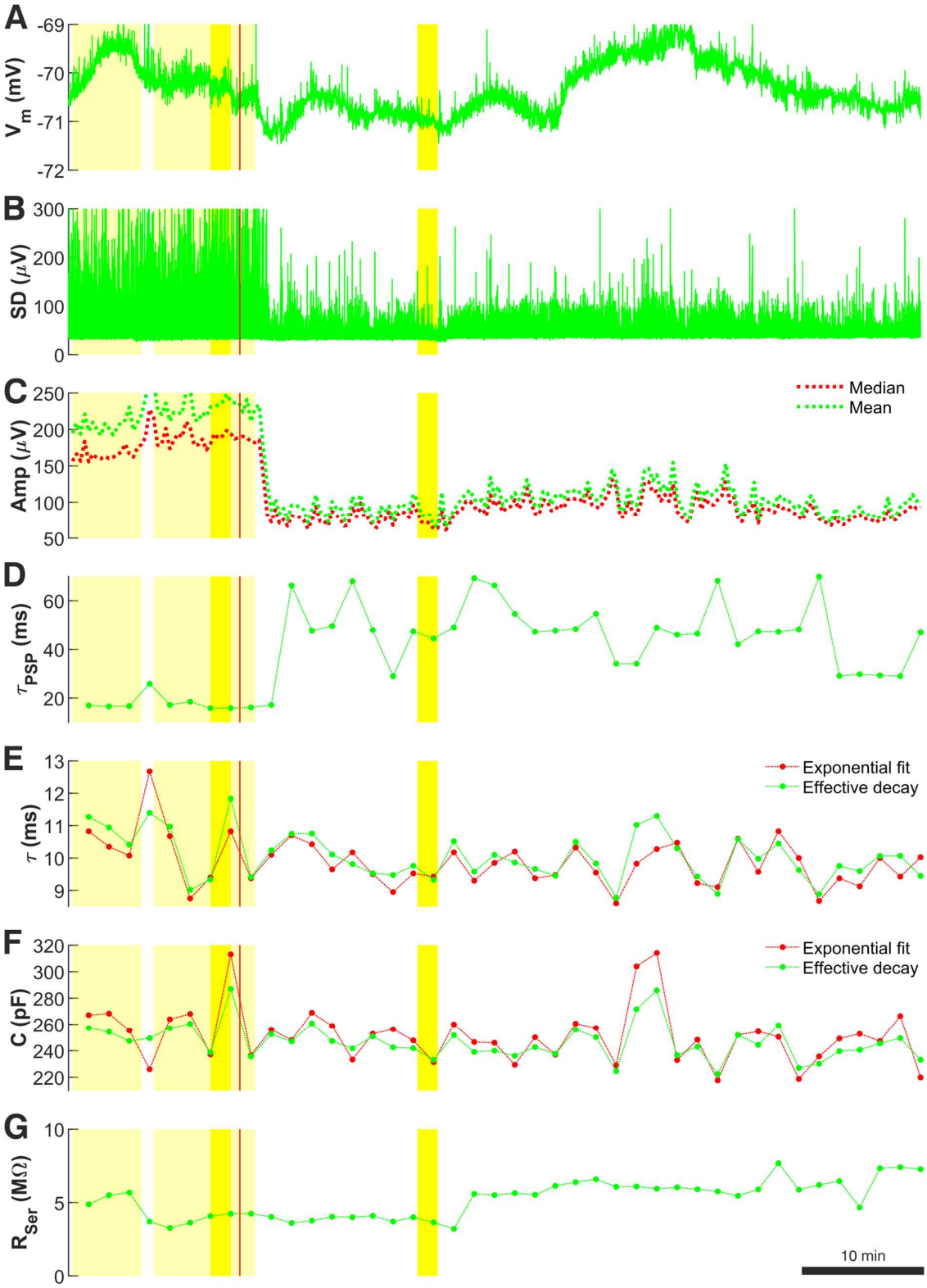

Supplementary Figure 6: Recording quality measures used during the data preprocessing stage to

1006 select ’noise with minis’ and ’noise-alone’ recording sweeps for further data analysis for recording
1007 p122a (layer 2/3).
1008 The meaning of panels A-G is explained in Supplementary figure 1 except for data being averaged
1009 over 100-second-long windows in panels D-G. The figure shows only part of the recording following
1010 the blockade of APs with only a single red vertical time marker visible indicating the time when
1011 pharmacological EPSP blockers were infused. The total duration of the recording shown in the figure
1012 was 4200 s.
1013

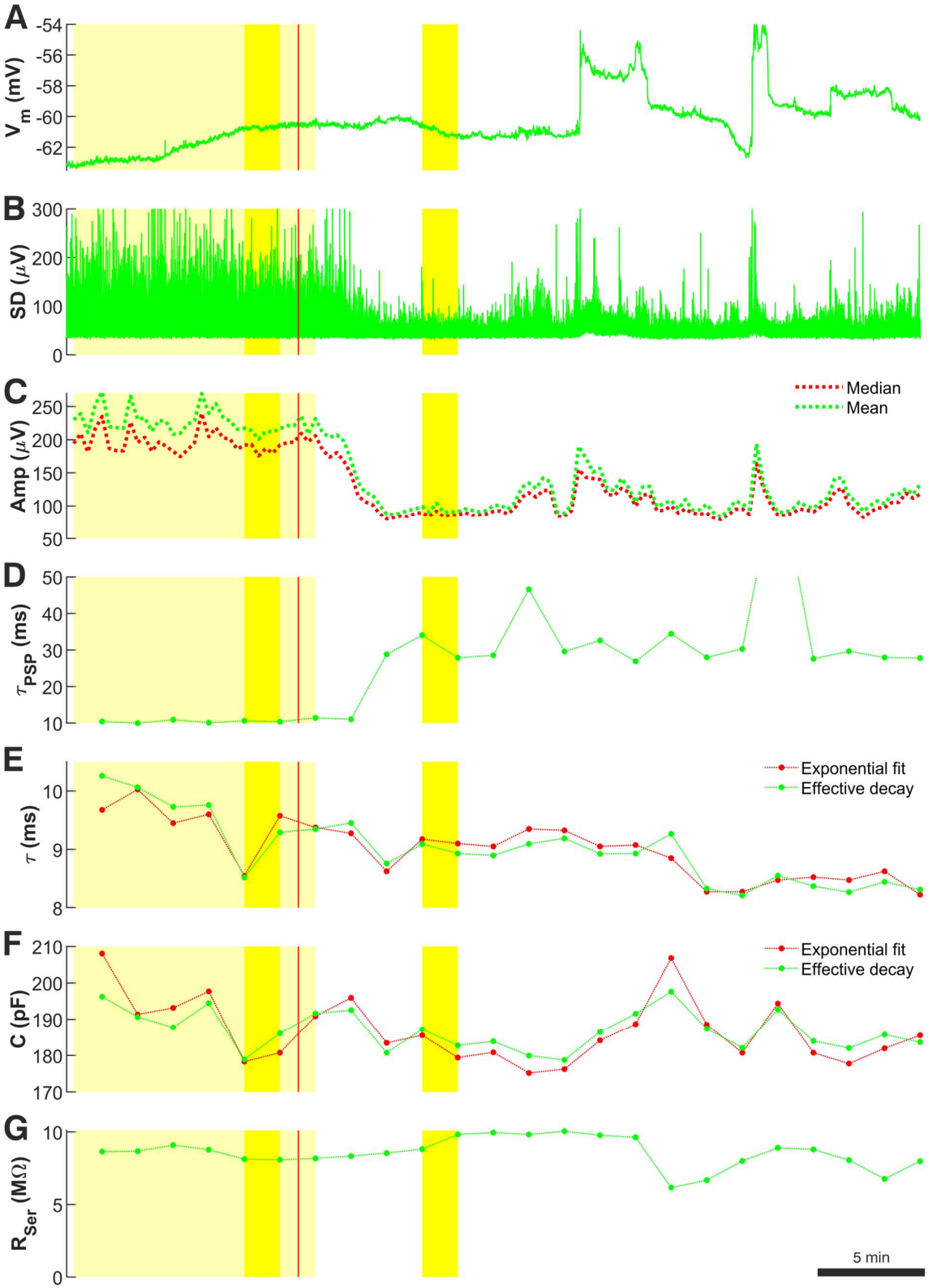

Supplementary Figure 7: Recording quality measures used during the data preprocessing stage to

1016 select ’noise with minis’ and ’noise-alone’ recording sweeps for further data analysis for recording
1017 p124b (layer 5).
1018 The meaning of panels A-G is explained in Supplementary figure 1 except for data being averaged
1019 over 100-second-long windows in panels D-G. The figure shows only part of the recording following
1020 the blockade of APs with only a single red vertical time marker visible indicating the time when
1021 pharmacological EPSP blockers were infused. The total duration of the recording shown in the figure
1022 was 2400 s.
1023

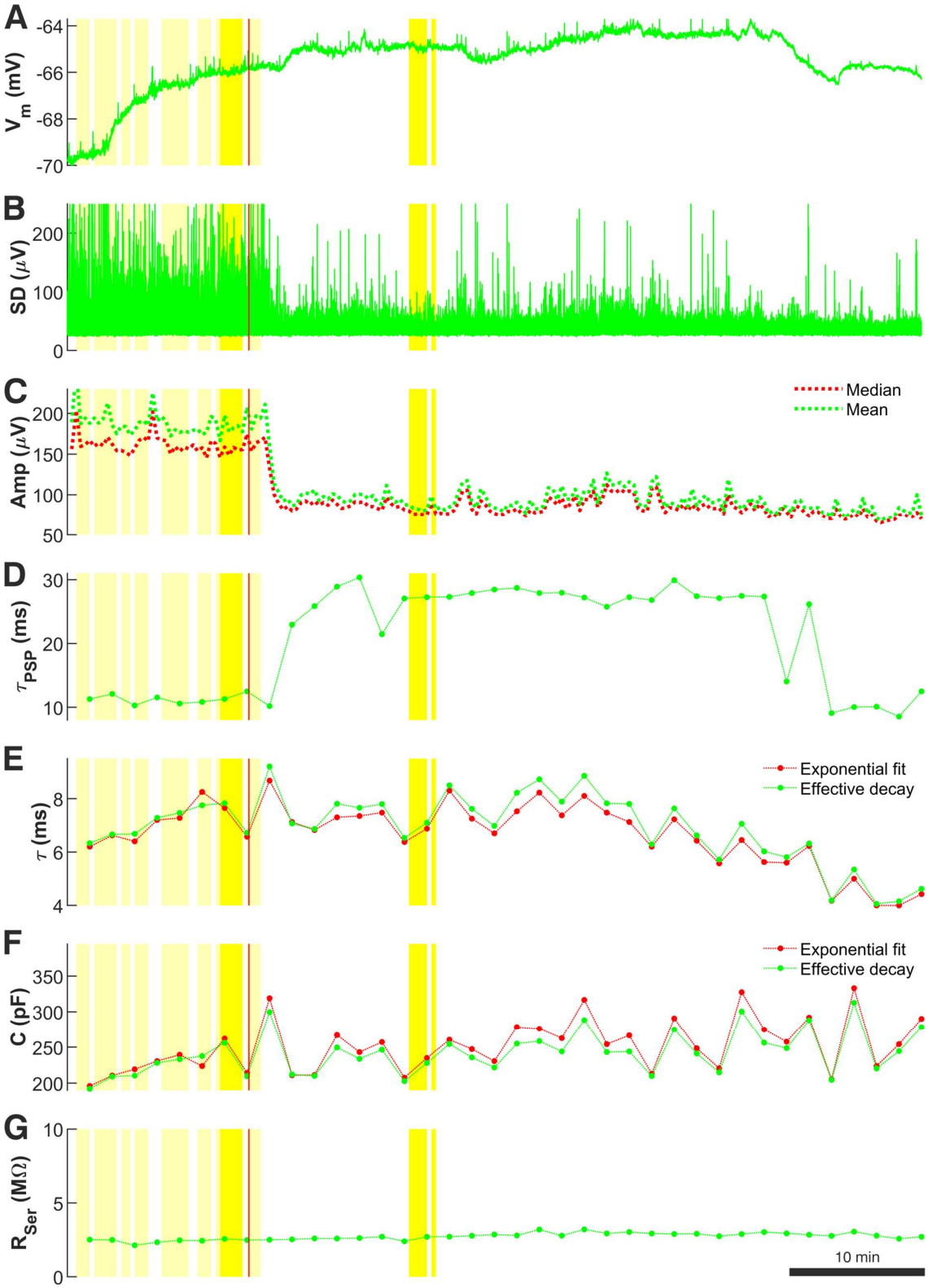

1024

1025 **Supplementary Figure 8:** Recording quality measures used during the data preprocessing stage to

1026 select ’noise with minis’ and ’noise-alone’ recording sweeps for further data analysis for recording
1027 p125a (layer 2/3).
1028 The meaning of panels A-G is explained in Supplementary figure 1 except for data being averaged
1029 over 100-second-long windows in panels D-G. The figure shows only part of the recording following
1030 the blockade of APs with only a single red vertical time marker visible indicating the time when
1031 pharmacological EPSP blockers were infused. The total duration of the recording shown in the figure
1032 was 3800 s.
1033

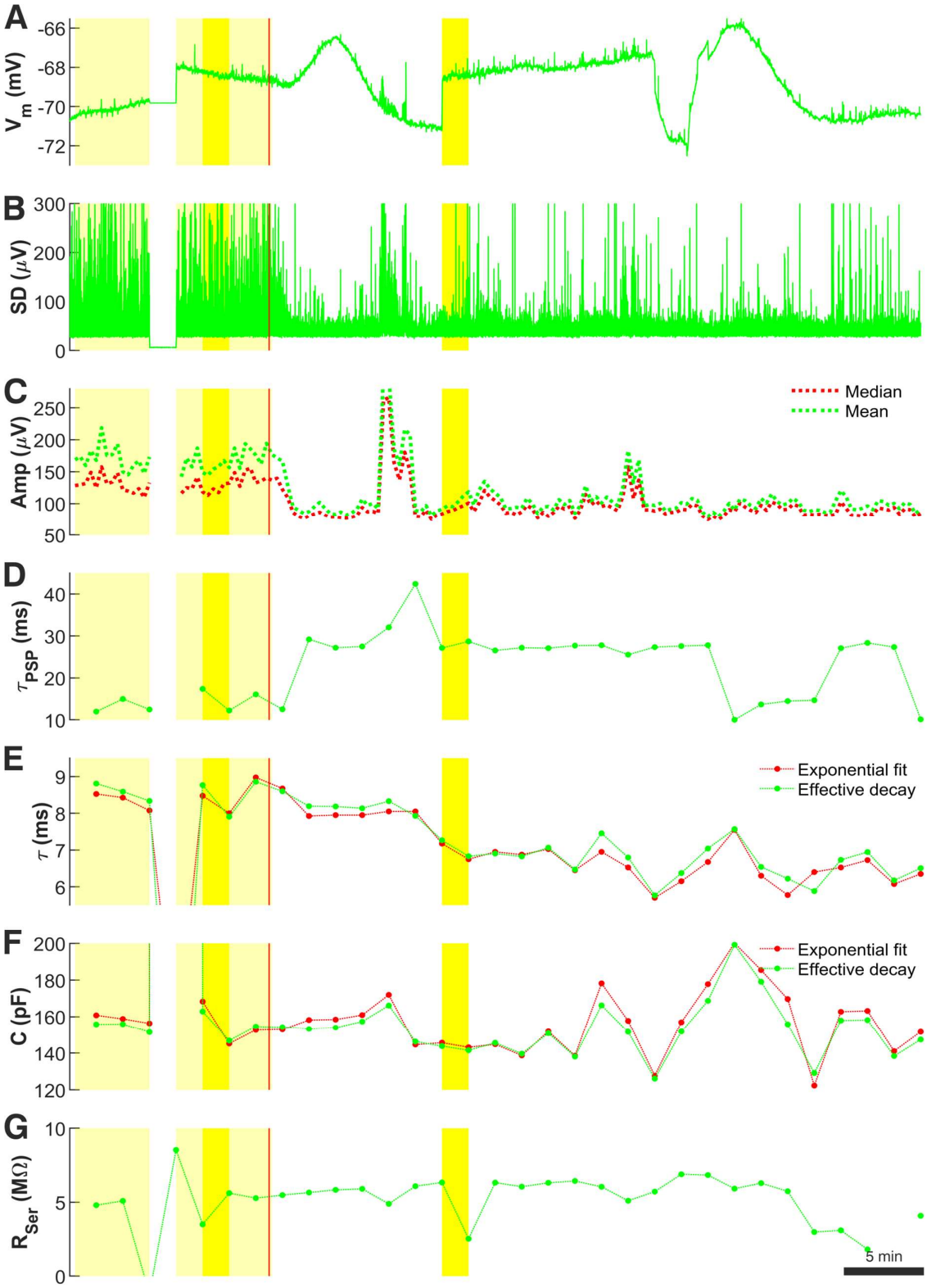

Supplementary Figure 9: Recording quality measures used during the data preprocessing stage to

1036 select ’noise with minis’ and ’noise-alone’ recording sweeps for further data analysis for recording
1037 p127c (layer 2/3).
1038 The meaning of panels A-G is explained in Supplementary figure 1 except for data being averaged
1039 over 100-second-long windows in panels D-G. The figure shows only part of the recording following
1040 the blockade of APs with only a single red vertical time marker visible indicating the time when
1041 pharmacological EPSP blockers were infused. The total duration of the recording shown in the figure
1042 was 3200 s.
1043

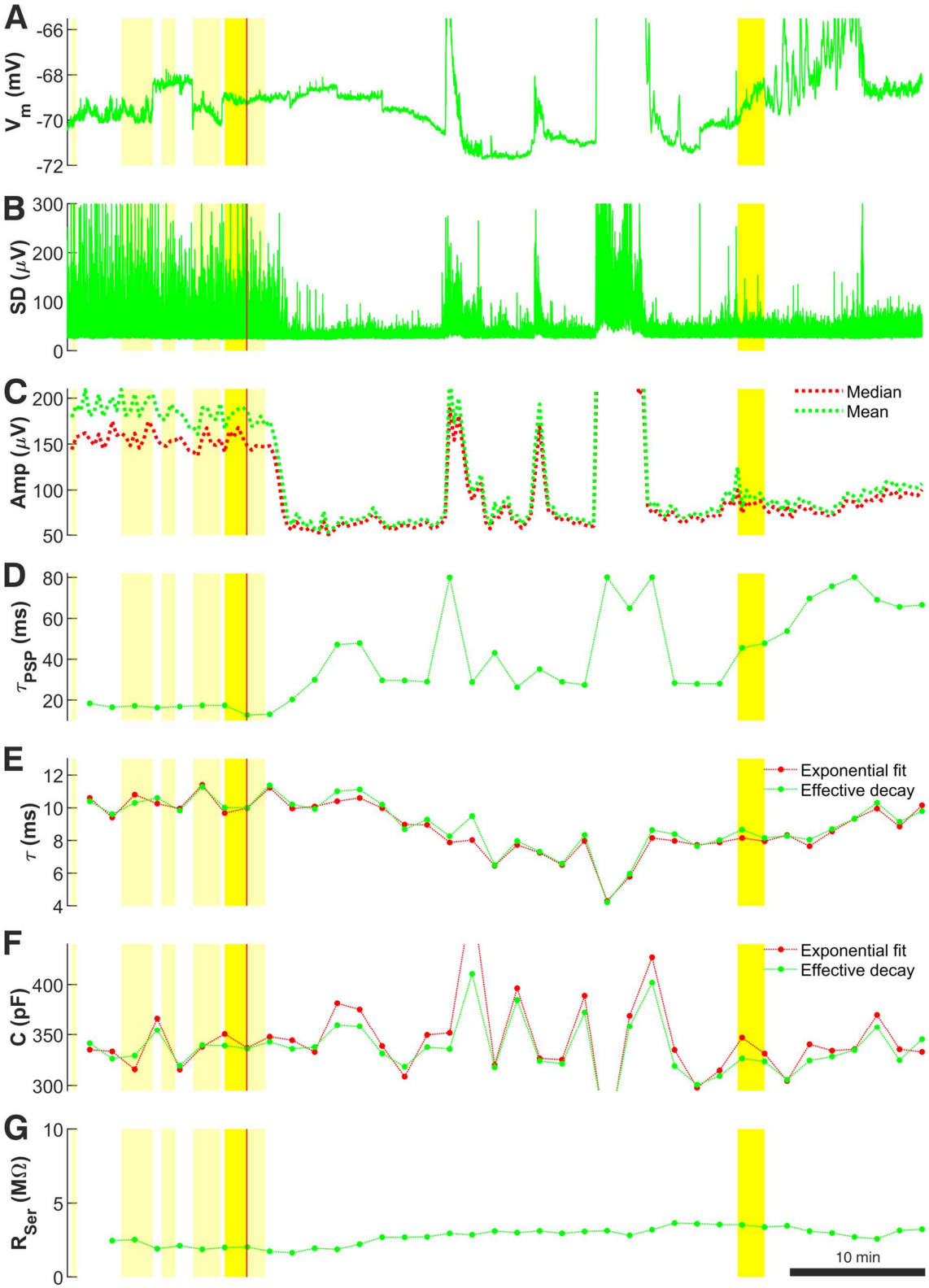
A
-66
-68
-70
-72
V_m (mV)
B
300
200
100
0
SD (μV)
C
200
150
100
50
Amp (μV)
Median
Mean
D
80
60
40
20
τ_{PSP} (ms)
E
12
10
8
6
4
τ (ms)
Exponential fit
Effective decay
F
400
350
300
C (pF)
Exponential fit
Effective decay
G
10
5
0
R_{Ser} (MΩ)
10 min

1044

1045 **Supplementary Figure 10:** Recording quality measures used during the data preprocessing stage to
1046 select 'noise with minis' and 'noise-alone' recording sweeps for further data analysis for recording
1047 p128c (layer 2/3).
1048 The meaning of panels A-G is explained in Supplementary figure 1 except for data being averaged
1049 over 100-second-long windows in panels D-G. The figure shows only part of the recording following
1050 the blockade of APs with only a single red vertical time marker visible indicating the time when
1051 pharmacological EPSP blockers were infused. The total duration of the recording shown in the figure
1052 was 3800 s.

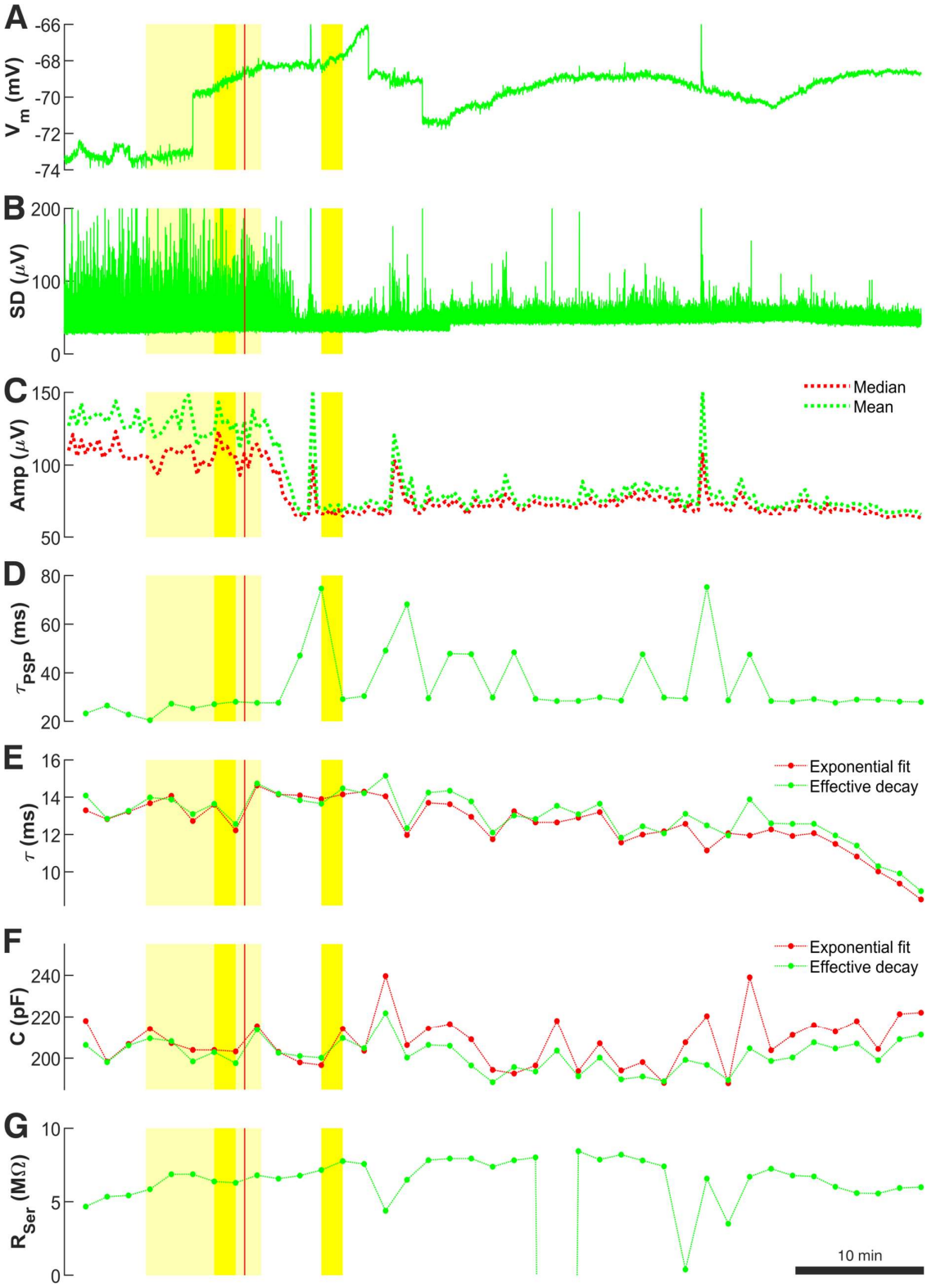

Supplementary Figure 11: Recording quality measures used during the data preprocessing stage to

1055 select ’noise with minis’ and ’noise-alone’ recording sweeps for further data analysis for recording
1056 p129a (layer 5).
1057 The meaning of panels A-G is explained in Supplementary figure 1 except for data being averaged
1058 over 100-second-long windows in panels D-G. The figure shows only part of the recording following
1059 the blockade of APs with only a single red vertical time marker visible indicating the time when
1060 pharmacological EPSP blockers were infused. The total duration of the recording shown in the figure
1061 was 4000 s.
1062

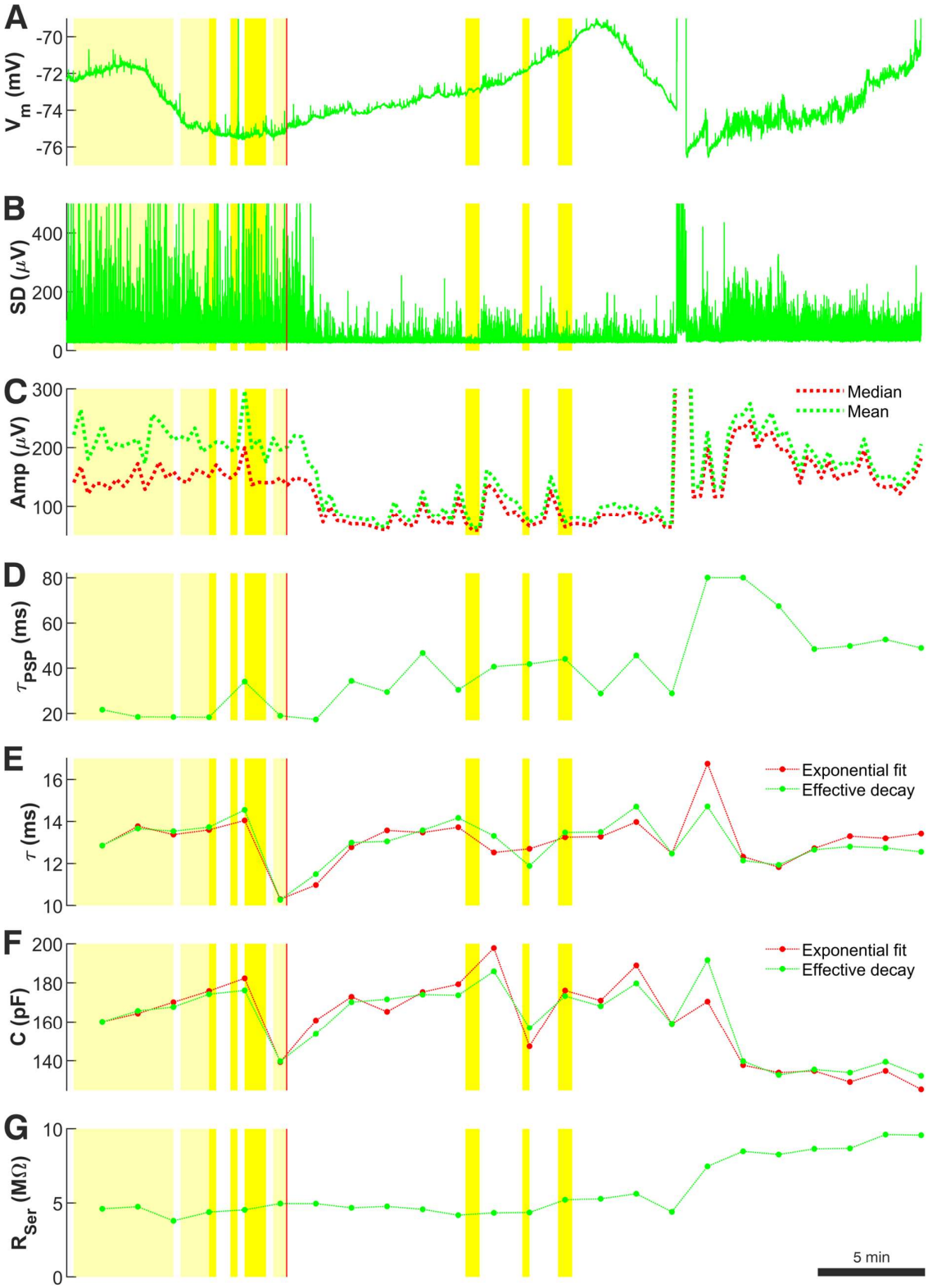

Supplementary Figure 12: Recording quality measures used during the data preprocessing stage to

1065 select ’noise with minis’ and ’noise-alone’ recording sweeps for further data analysis for recording
1066 p131a (layer 2/3).
1067 The meaning of panels A-G is explained in Supplementary figure 1 except for data being averaged
1068 over 100-second-long windows in panels D-G. The figure shows only part of the recording following
1069 the blockade of APs with only a single red vertical time marker visible indicating the time when
1070 pharmacological EPSP blockers were infused. The total duration of the recording shown in the figure
1071 was 2400 s.
1072

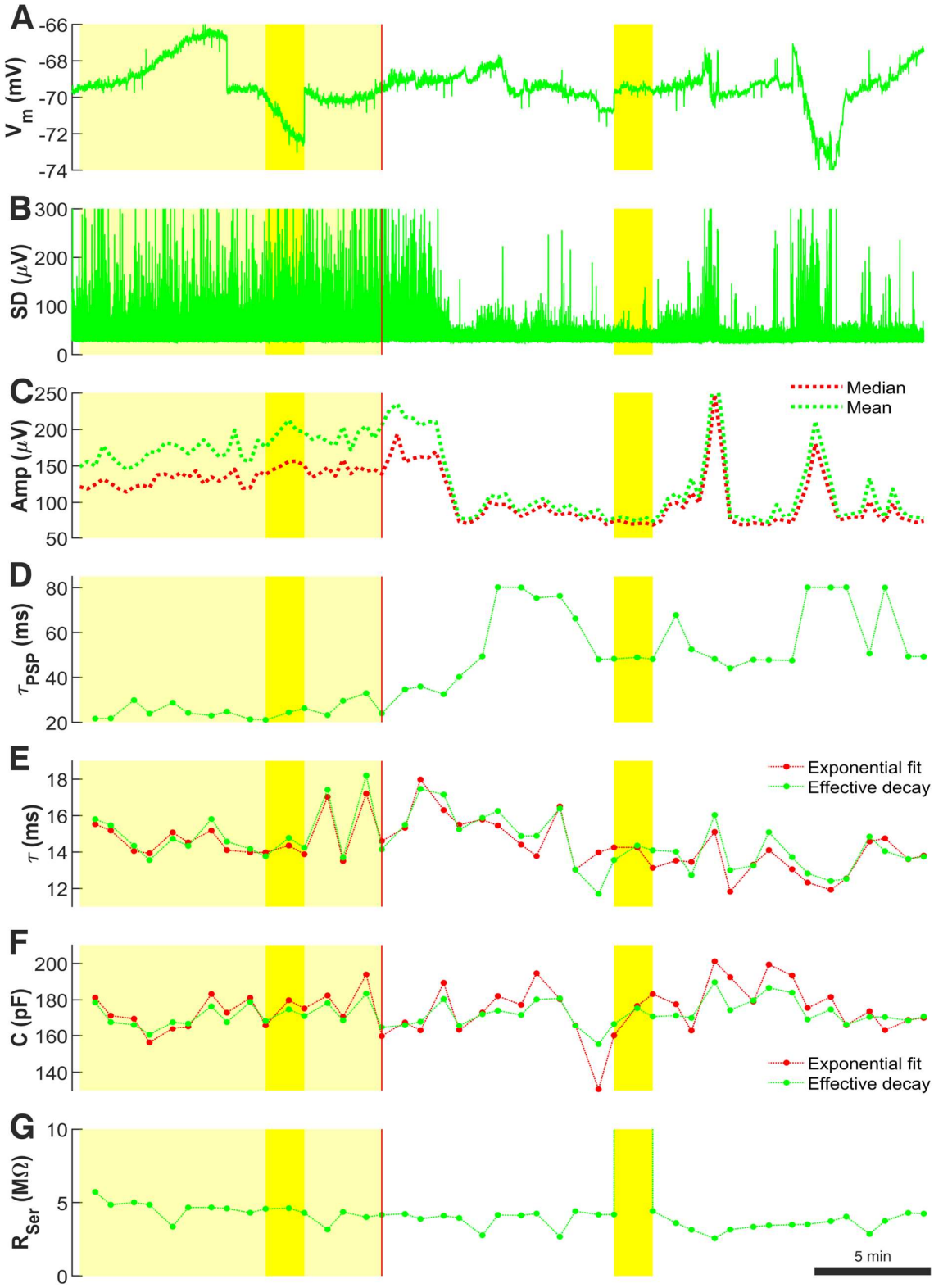

Supplementary Figure 13: Recording quality measures used during the data preprocessing stage to

1075 select ’noise with minis’ and ’noise-alone’ recording sweeps for further data analysis for recording
1076 p131c (layer 2/3).
1077 The meaning of panels A-G is explained in Supplementary figure 1 except for data being averaged
1078 over 100-second-long windows in panels D-G. The figure shows only part of the recording following
1079 the blockade of APs with only a single red vertical time marker visible indicating the time when
1080 pharmacological EPSP blockers were infused. The total duration of the recording shown in the figure
1081 was 2200 s.
1082

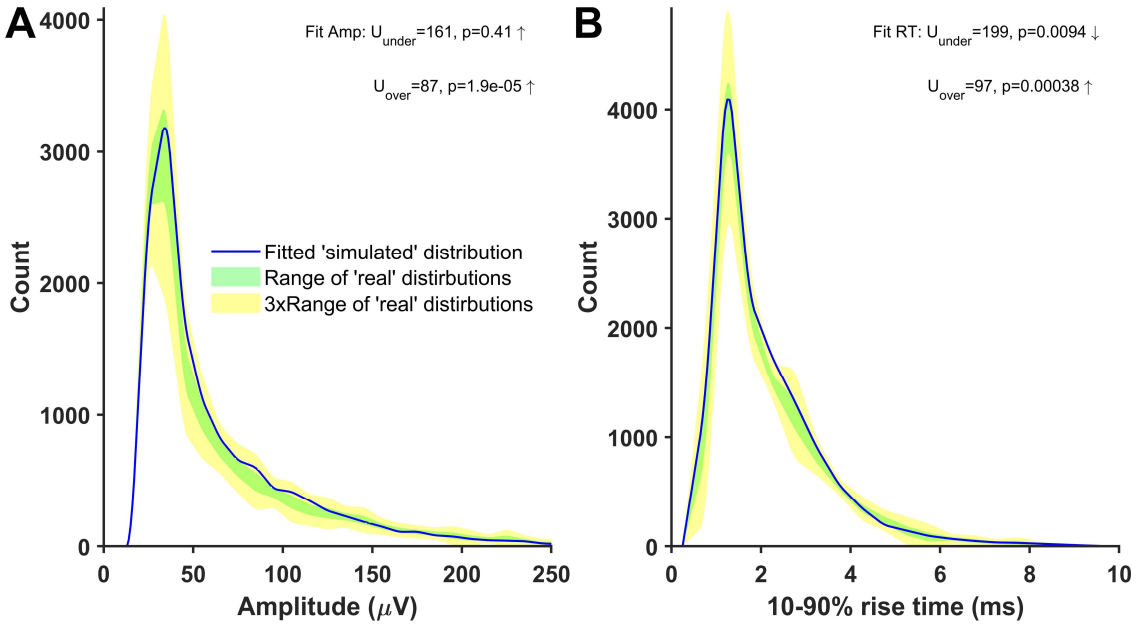

Supplementary figure 14: Distributions of minis-like events detected in a ’noise + simulated minis’ voltage trace that closely matched ‘noise + real minis‘ recordings.

Parameters of simulated minis were controlled by the GA, whereas the ’noise-alone’ recording was obtained in cell p103a of the cortical layer 5. Upward arrows indicate ‘simulated’ SAD > ‘real’ SAD relationship and downward arrows indicate ‘simulated’ SAD < ‘real’ SAD relationship. The underfit test involves a comparison with the worst-performing ‘real’ SAD, whereas the overfit test involves a comparison with the best-performing ‘real’ SAD.

(A) Amplitude distribution of minis-like events detected in a ’noise + simulated minis’ voltage trace (the blue curve).

(B) 10-90% rise time distribution of minis-like events detected in a ’noise + simulated minis’ voltage trace (the blue curve).

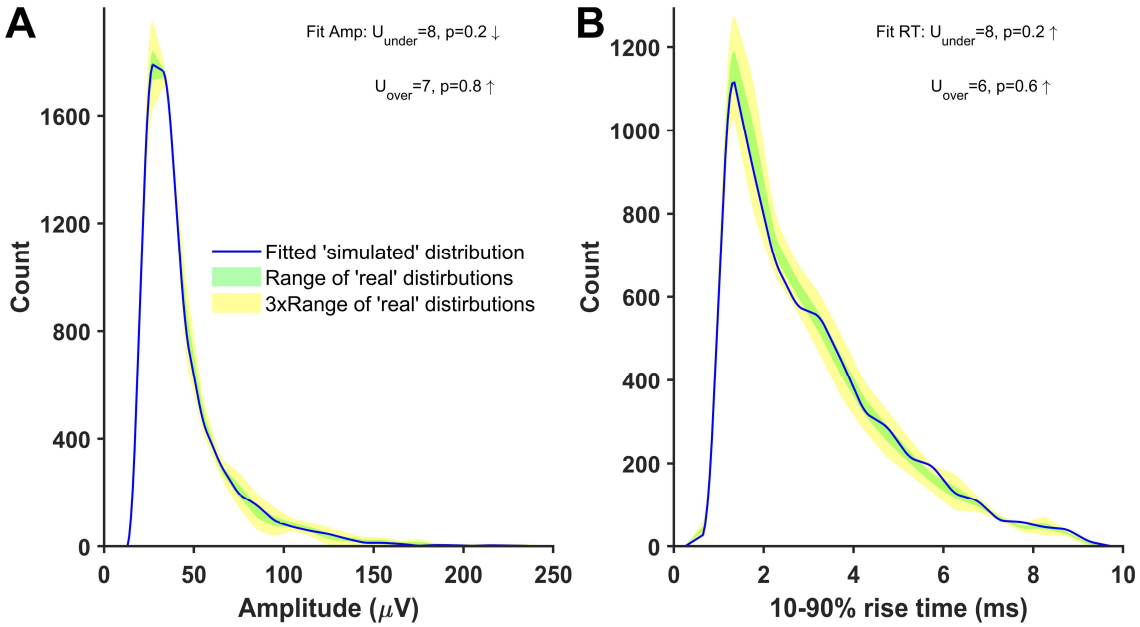

Supplementary figure 15: Distributions of minis-like events detected in a ’noise with simulated minis’ voltage trace that closely matched ‘noise with real minis‘ recordings. Parameters of simulated minis were controlled by the GA, whereas the ’noise-alone’ recording was obtained in cell p108a of the cortical layer 5. The meanings of the upward and downward arrows are explained in Supplementary figure 14.

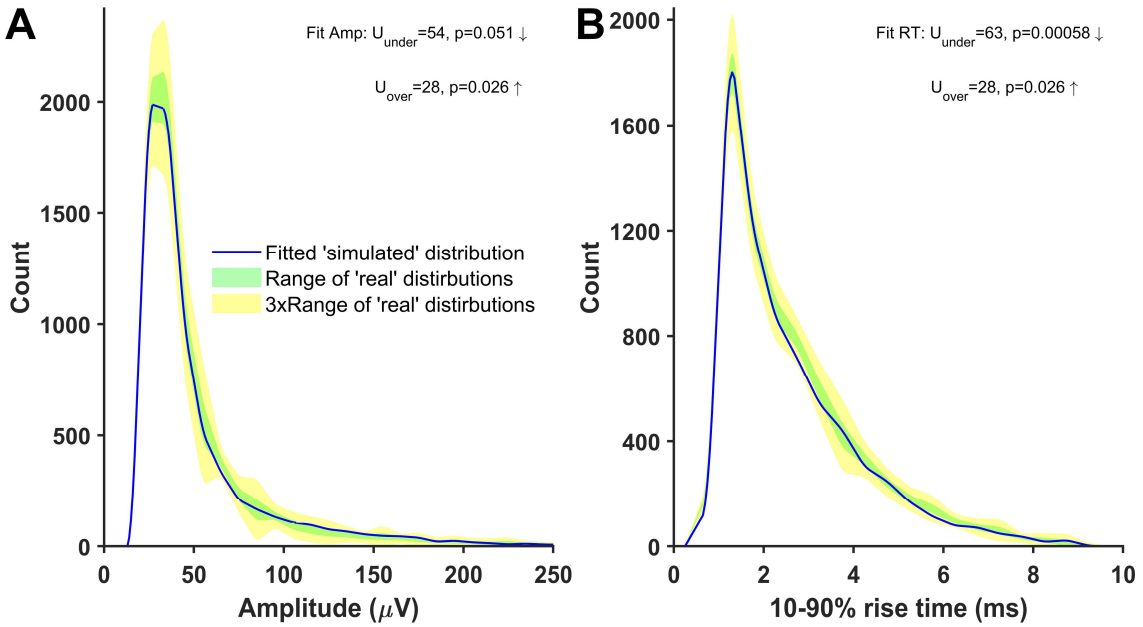

Supplementary figure 16: Distributions of minis-like events detected in a ’noise with simulated minis’ voltage trace that closely matched ‘noise with real minis‘ recordings. Parameters of simulated minis were controlled by the GA, whereas the ’noise-alone’ recording was obtained in cell p108b of the cortical layer 5. The meanings of the upward and downward arrows are explained in Supplementary figure 14.

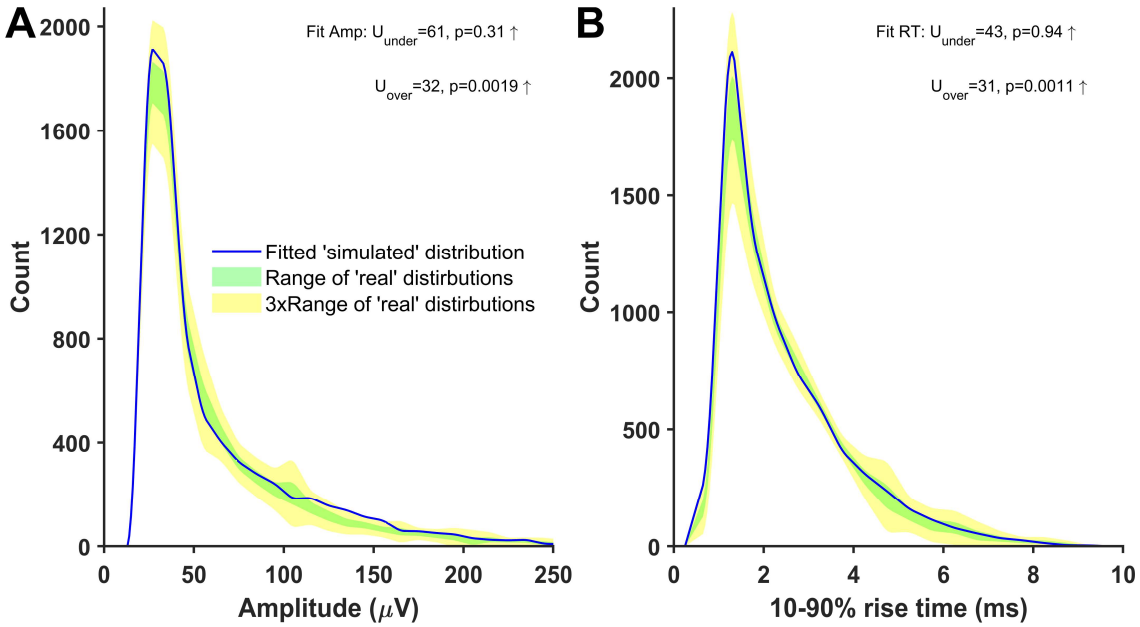

Supplementary figure 17: Distributions of minis-like events detected in a ’noise with simulated minis’ voltage trace that closely matched ‘noise with real minis‘ recordings. Parameters of simulated minis were controlled by the GA, whereas the ’noise-alone’ recording was obtained in cell p108c of the cortical layer 5. The meanings of the upward and downward arrows are explained in Supplementary figure 14.

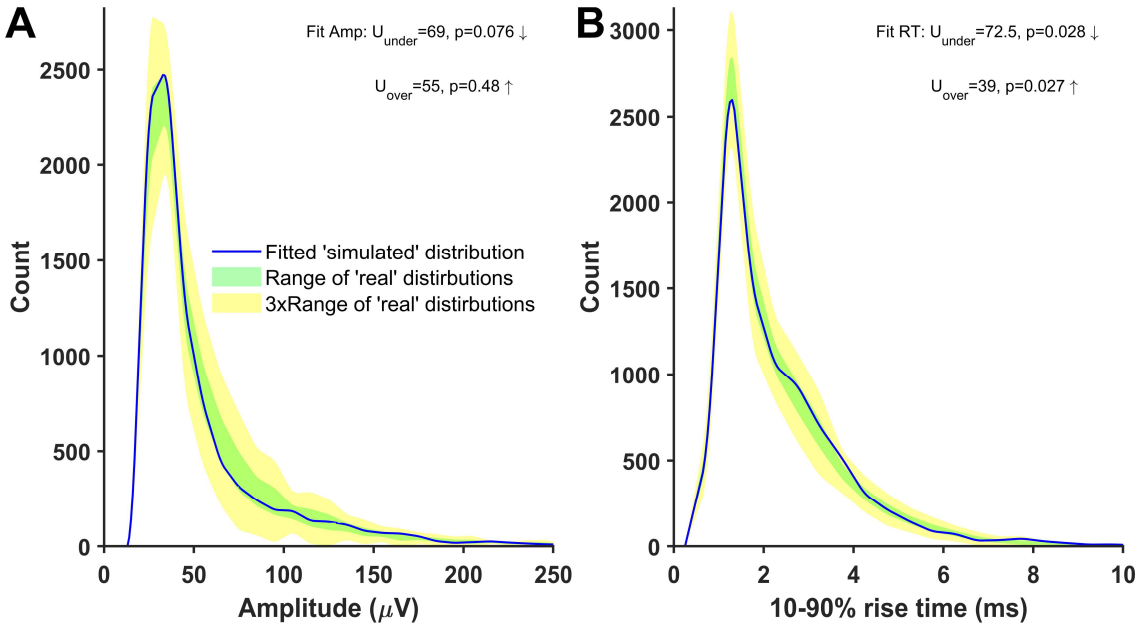

Supplementary figure 18: Distributions of minis-like events detected in a ’noise with simulated minis’ voltage trace that closely matched ‘noise with real minis‘ recordings. Parameters of simulated minis were controlled by the GA, whereas the ’noise-alone’ recording was obtained in cell p120b of the cortical layer 2/3. The meanings of the upward and downward arrows are explained in Supplementary figure 14.

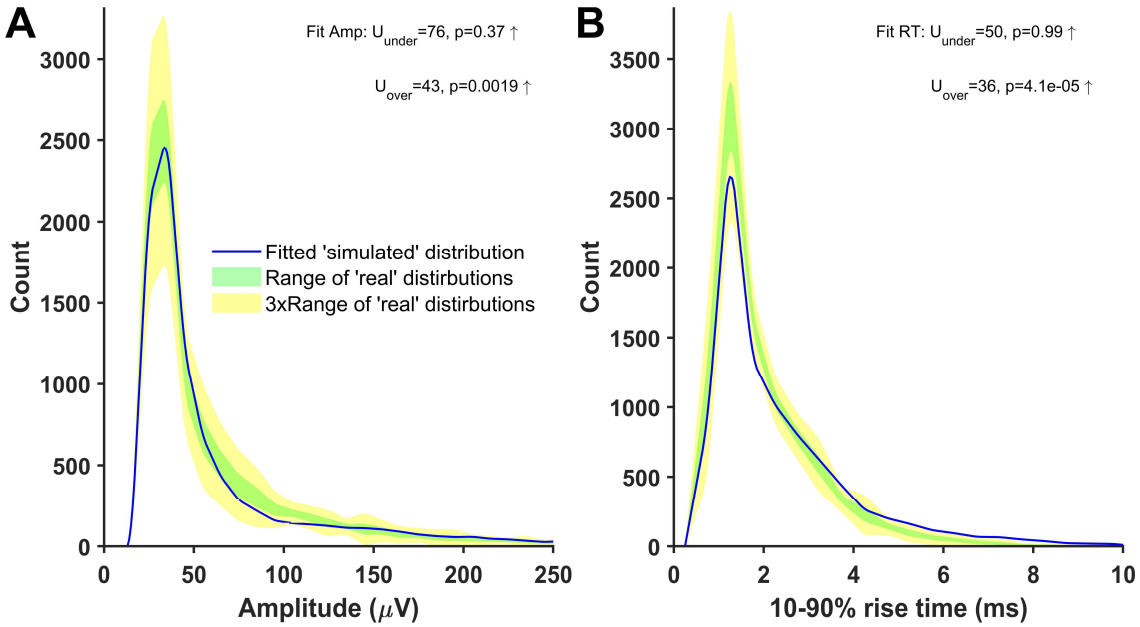

Supplementary figure 19: Distributions of minis-like events detected in a ’noise with simulated minis’ voltage trace that closely matched ‘noise with real minis‘ recordings. Parameters of simulated minis were controlled by the GA, whereas the ’noise-alone’ recording was obtained in cell p122a of the cortical layer 2/3. The meanings of the upward and downward arrows are explained in Supplementary figure 14.

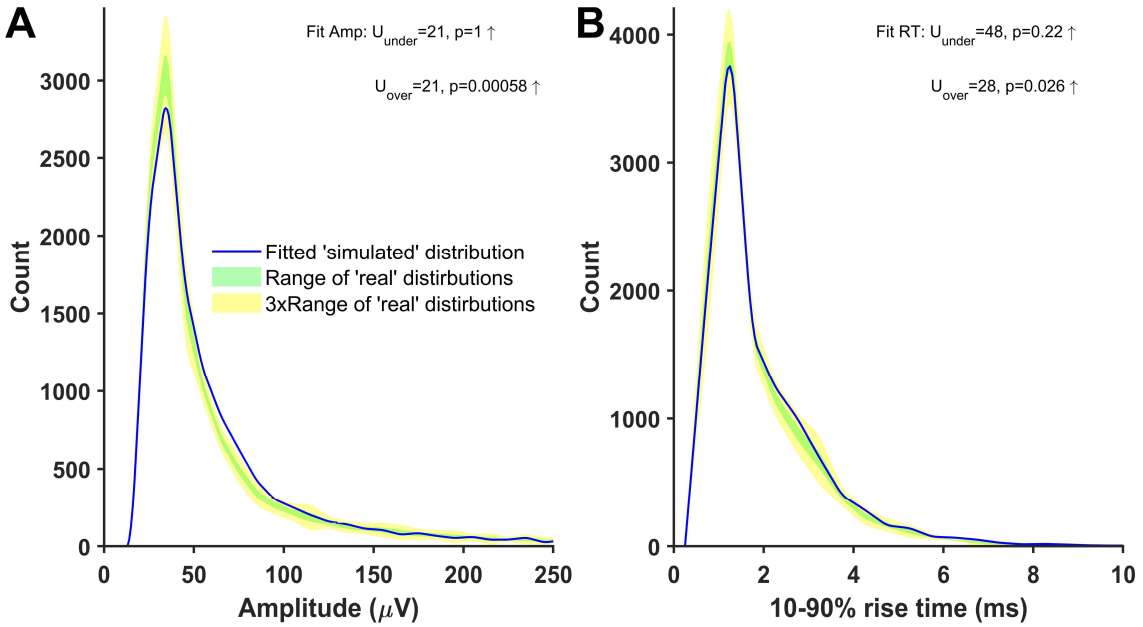

Supplementary figure 20: Distributions of minis-like events detected in a ’noise with simulated minis’ voltage trace that closely matched ‘noise with real minis‘ recordings. Parameters of simulated minis were controlled by the GA, whereas the ’noise-alone’ recording was obtained in cell p124b of the cortical layer 5. The meanings of the upward and downward arrows are explained in Supplementary figure 14.

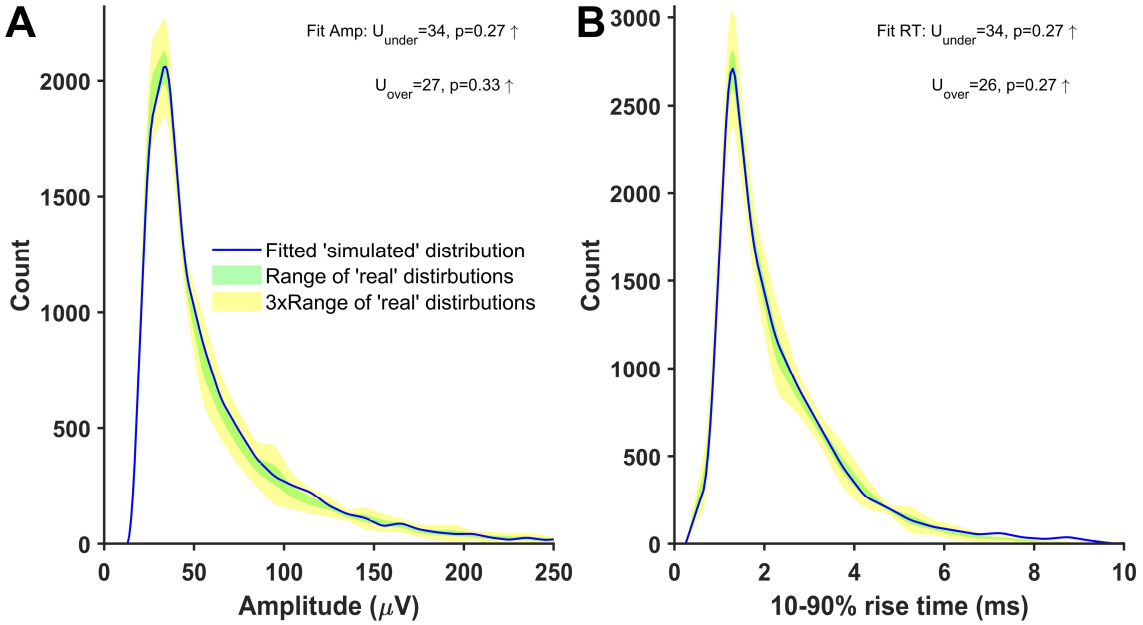

Supplementary figure 21: Distributions of minis-like events detected in a ’noise with simulated minis’ voltage trace that closely matched ‘noise with real minis‘ recordings. Parameters of simulated minis were controlled by the GA, whereas the ’noise-alone’ recording was obtained in cell p125a of the cortical layer 2/3. The meanings of the upward and downward arrows are explained in Supplementary figure 14.

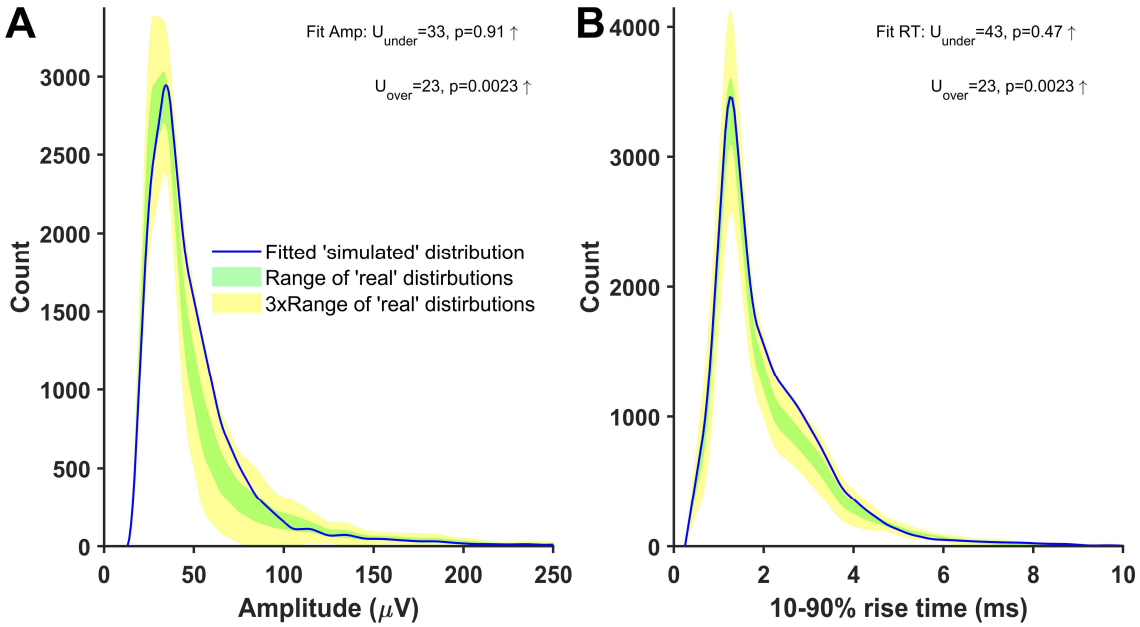

Supplementary figure 22: Distributions of minis-like events detected in a ’noise with simulated minis’ voltage trace that closely matched ‘noise with real minis‘ recordings. Parameters of simulated minis were controlled by the GA, whereas the ’noise-alone’ recording was obtained in cell p127c of the cortical layer 2/3. The meanings of the upward and downward arrows are explained in Supplementary figure 14.

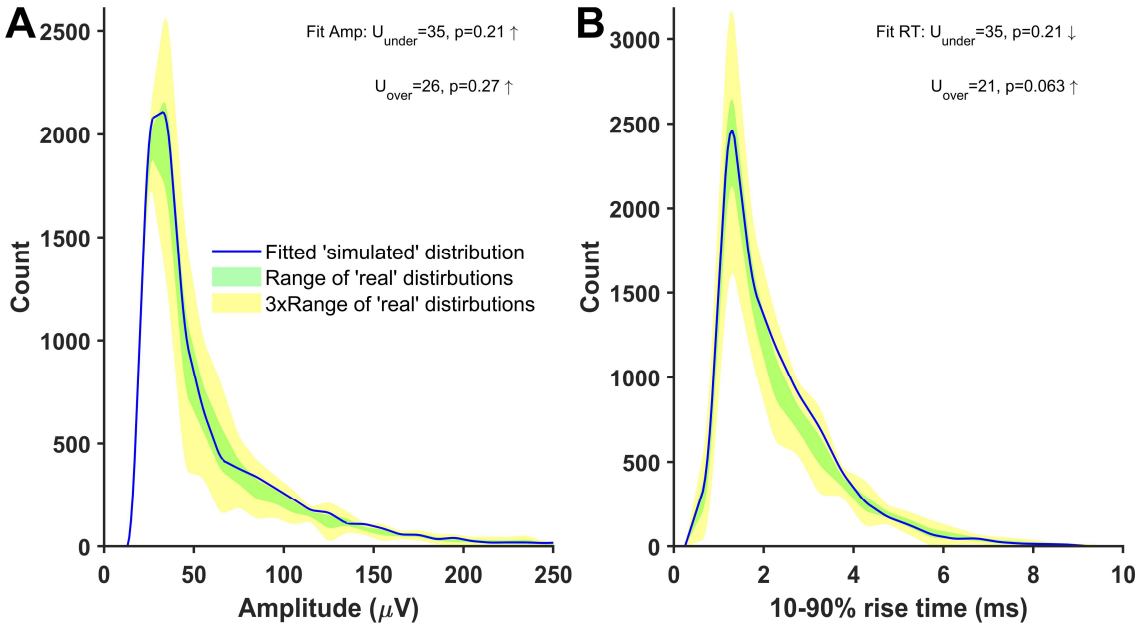

Supplementary figure 23: Distributions of minis-like events detected in a ’noise with simulated minis’ voltage trace that closely matched ‘noise with real minis‘ recordings. Parameters of simulated minis were controlled by the GA, whereas the ’noise-alone’ recording was obtained in cell p128c of the cortical layer 2/3. The meanings of the upward and downward arrows are explained in Supplementary figure 14.

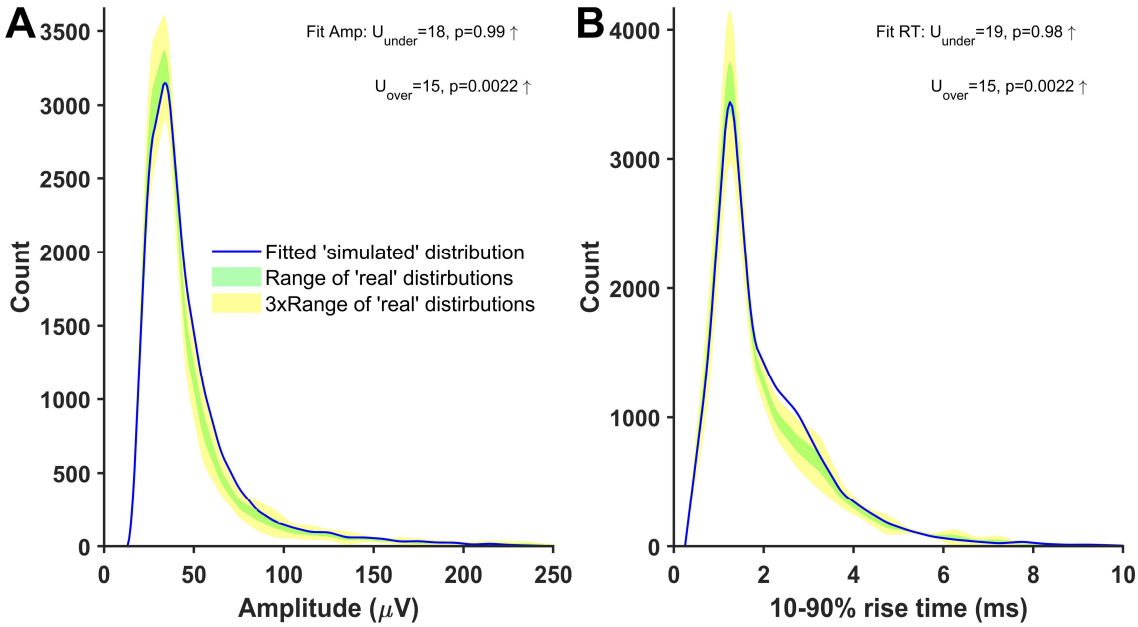

Supplementary figure 24: Distributions of minis-like events detected in a ’noise with simulated minis’ voltage trace that closely matched ‘noise with real minis‘ recordings. Parameters of simulated minis were controlled by the GA, whereas the ’noise-alone’ recording was obtained in cell p129a of the cortical layer 5. The meanings of the upward and downward arrows are explained in Supplementary figure 14.

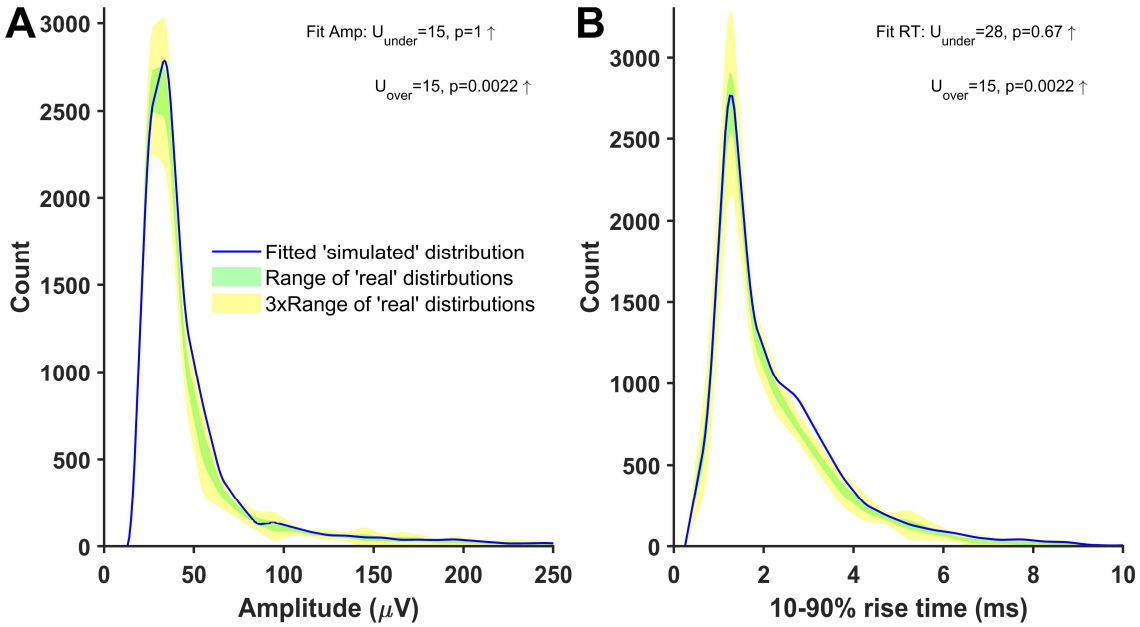

Supplementary figure 25: Distributions of minis-like events detected in a ’noise with simulated minis’ voltage trace that closely matched ‘noise with real minis‘ recordings. Parameters of simulated minis were controlled by the GA, whereas the ’noise-alone’ recording was obtained in cell p131a of the cortical layer 2/3. The meanings of the upward and downward arrows are explained in Supplementary figure 14.

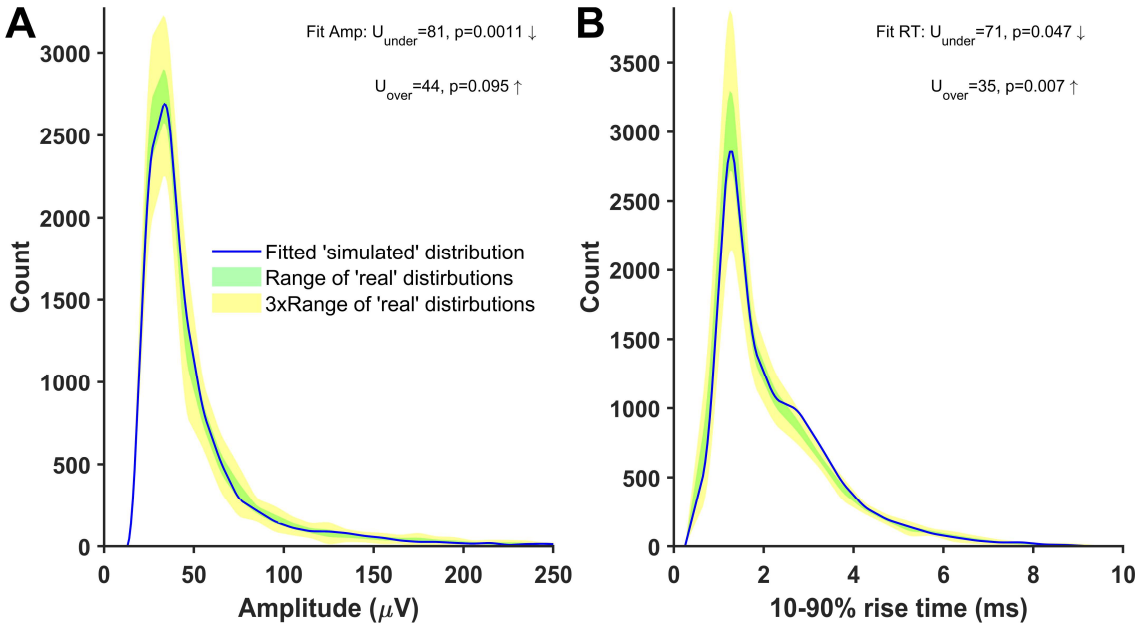

Supplementary figure 26: Distributions of minis-like events detected in a ’noise with simulated minis’ voltage trace that closely matched ‘noise with real minis‘ recordings. Parameters of simulated minis were controlled by the GA, whereas the ’noise-alone’ recording was obtained in cell p131c of the cortical layer 2/3. The meanings of the upward and downward arrows are explained in Supplementary figure 14.

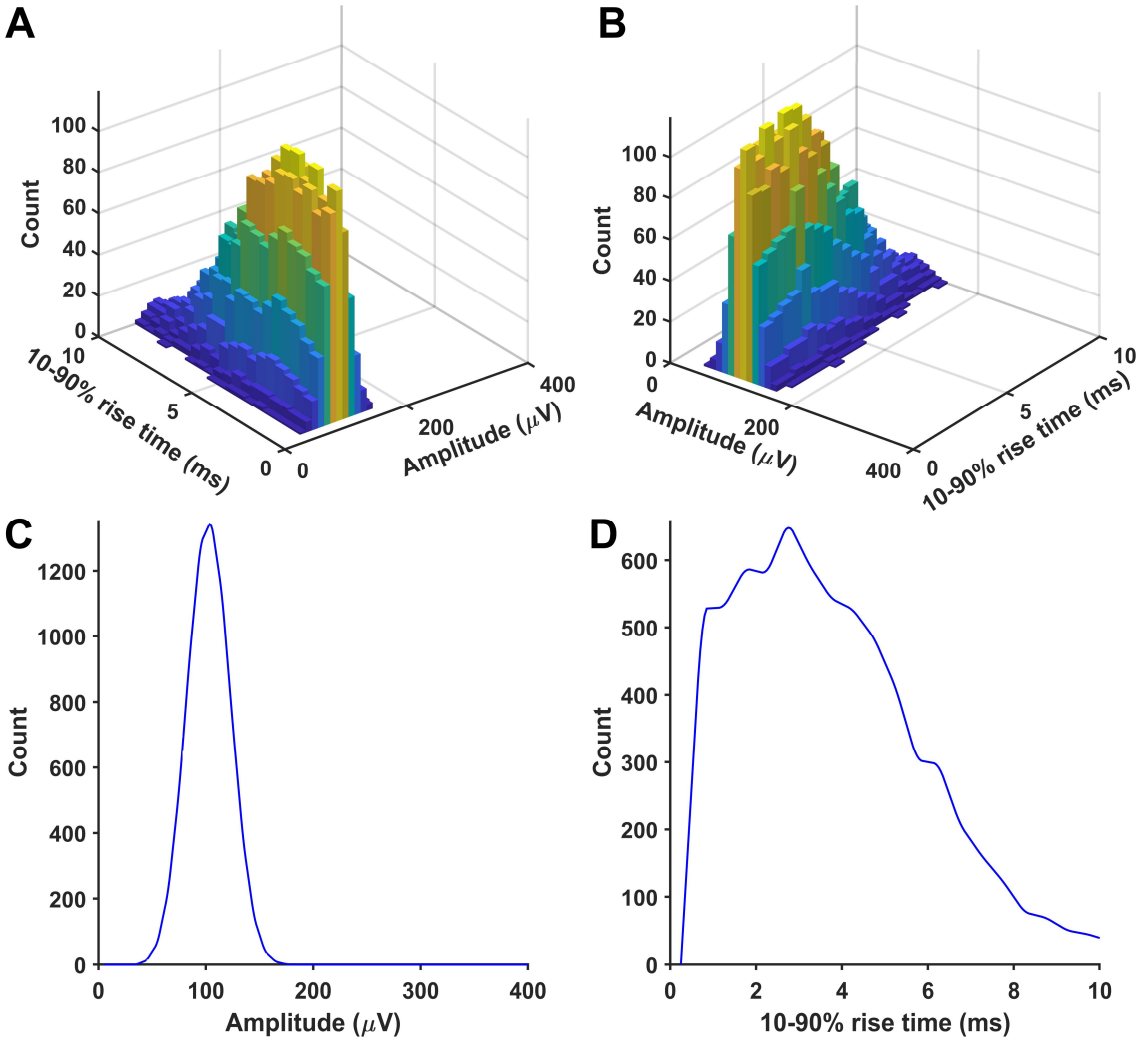

Supplementary figure 27: An example of simulated minis distribution that was used to produce a close match between distributions of detected minis-like events in a 'noise with simulated minis' voltage trace and in a 'noise with real minis' recording for a cell p103a of cortical layer 5.

(A) A joint amplitude and 10-90% rise time distribution of simulated minis.

(B) The same distribution but viewed from a different angle.

(C) Marginal amplitude distribution of the same distribution as in (A).

(D) Marginal 10-90% rise time distribution of the same distribution as in (A).

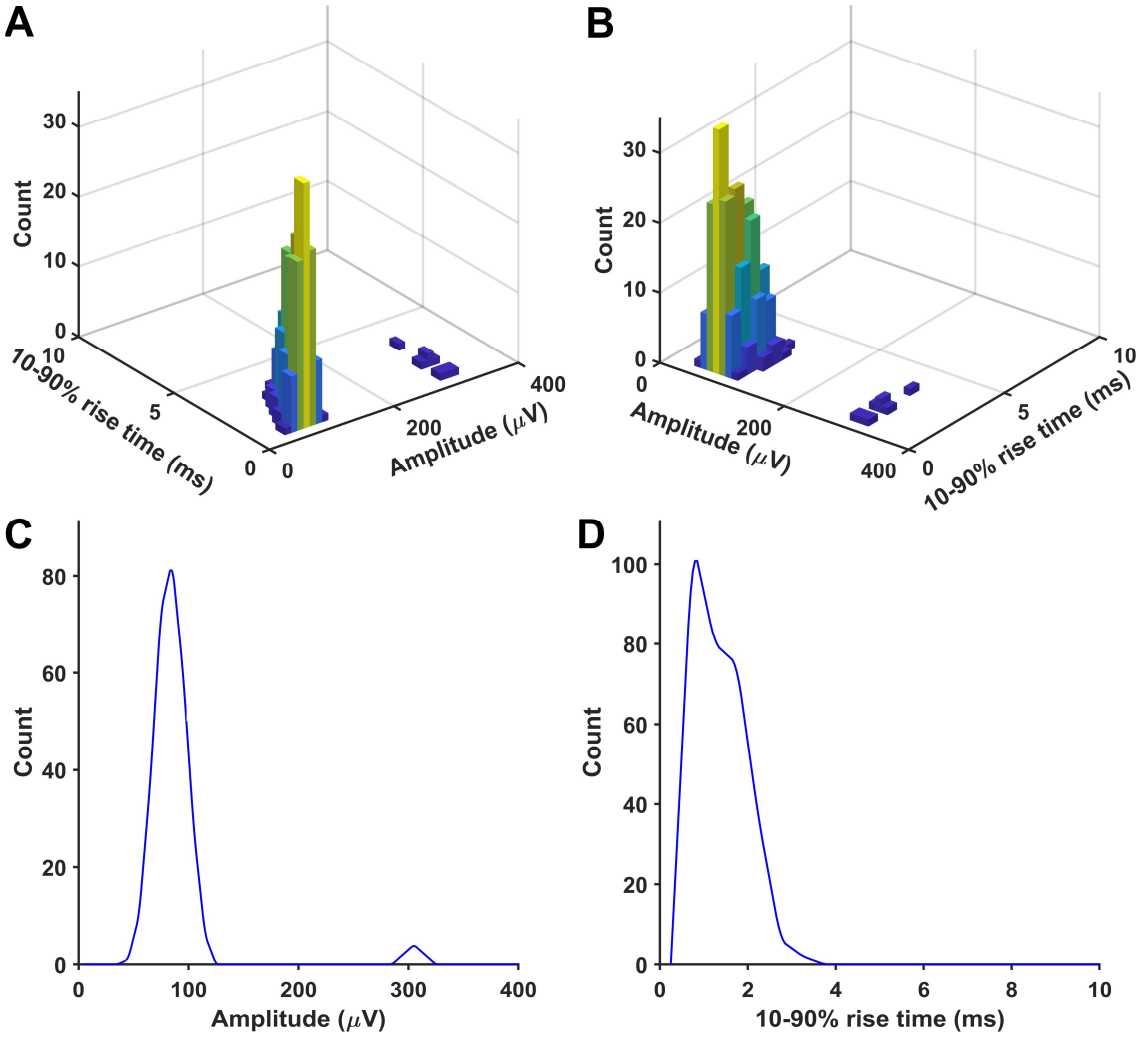

Supplementary figure 28: An example of simulated minis distribution that was used to produce a close match between distributions of detected minis-like events in a 'noise with simulated minis' voltage trace and in a 'noise with real minis' recording for a cell p106b of cortical layer 5. The meaning of different figure panels is explained in Supplementary figure 27.

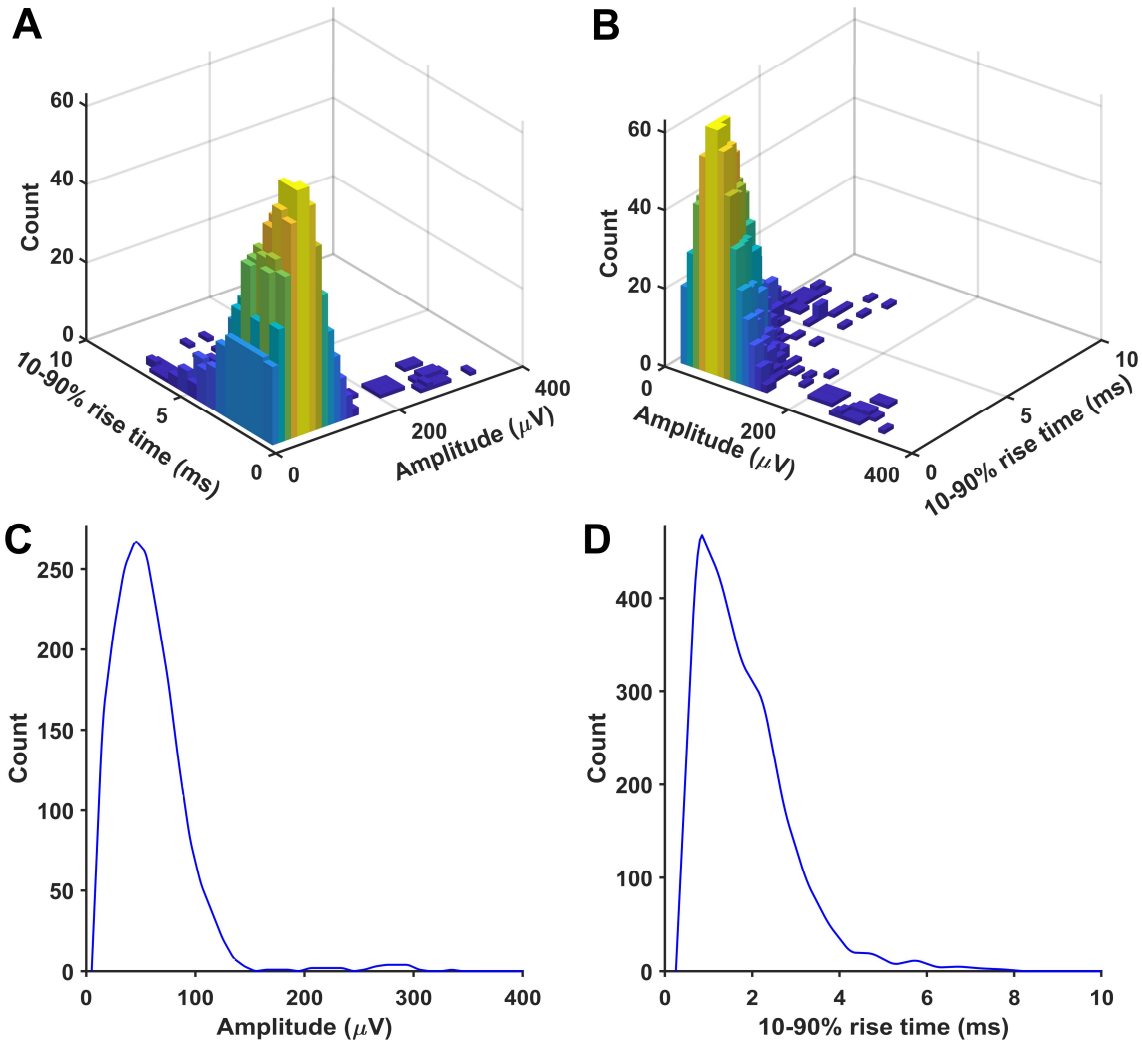

Supplementary figure 29: An example of simulated minis distribution that was used to produce a close match between distributions of detected minis-like events in a 'noise with simulated minis' voltage trace and in a 'noise with real minis' recording for a cell p108a of cortical layer 5. The meaning of different figure panels is explained in Supplementary figure 27.

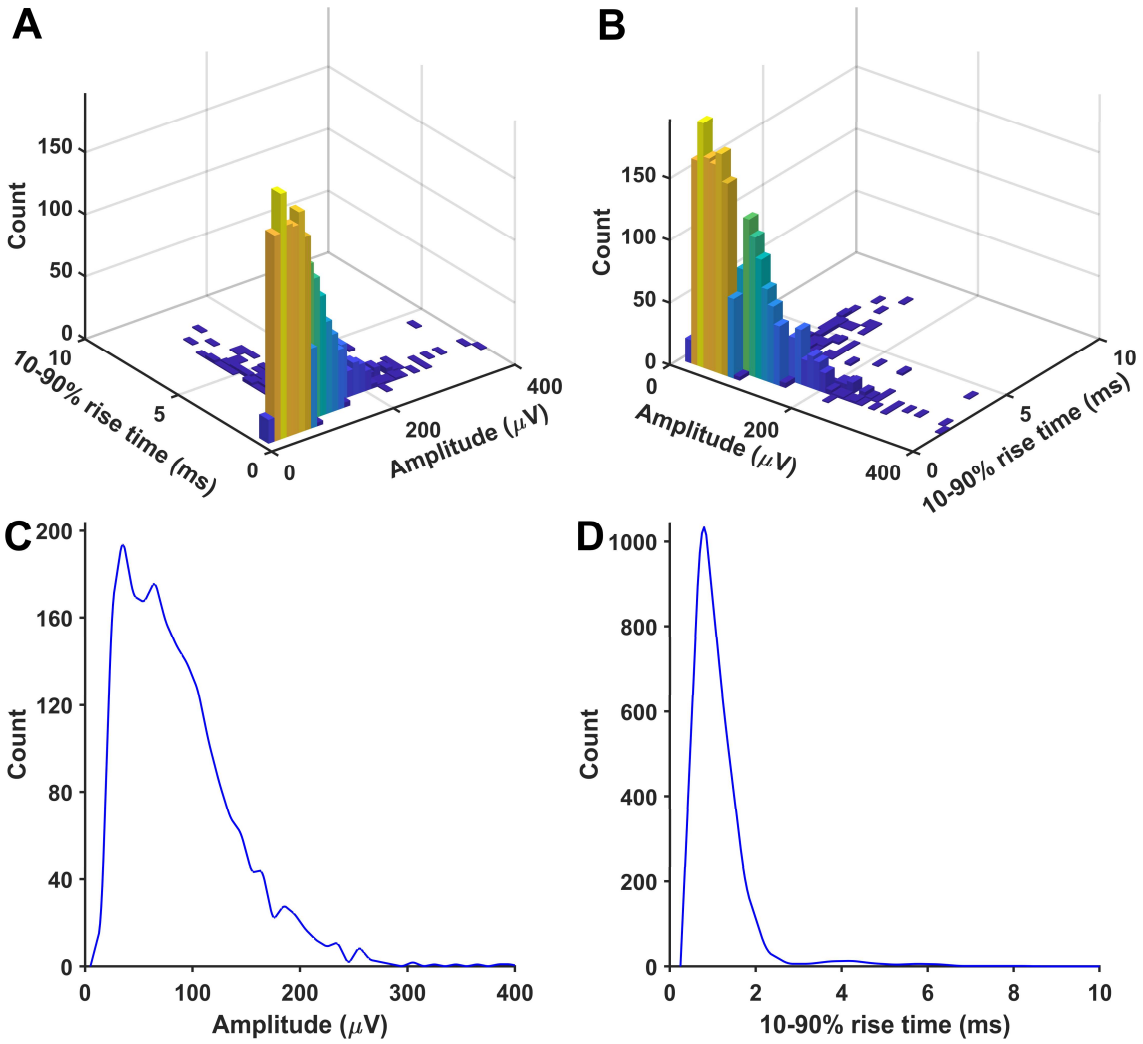

Supplementary figure 30: An example of simulated minis distribution that was used to produce a close match between distributions of detected minis-like events in a 'noise with simulated minis' voltage trace and in a 'noise with real minis' recording for a cell p108b of cortical layer 5. The meaning of different figure panels is explained in Supplementary figure 27.

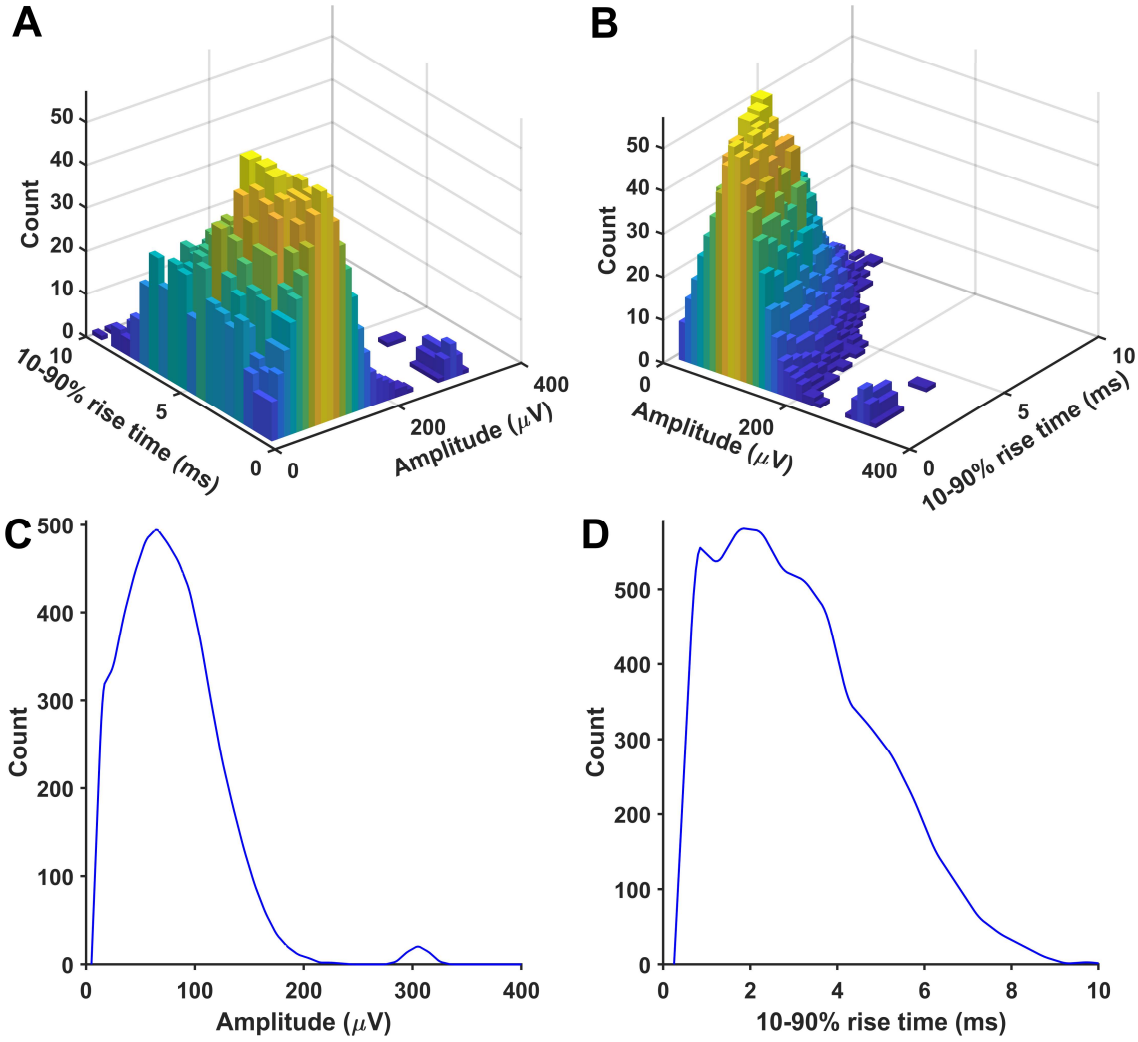

Supplementary figure 31: An example of simulated minis distribution that was used to produce a close match between distributions of detected minis-like events in a ’noise with simulated minis’ voltage trace and in a ’noise with real minis’ recording for a cell p108c of cortical layer 5. The meaning of different figure panels is explained in Supplementary figure 27.

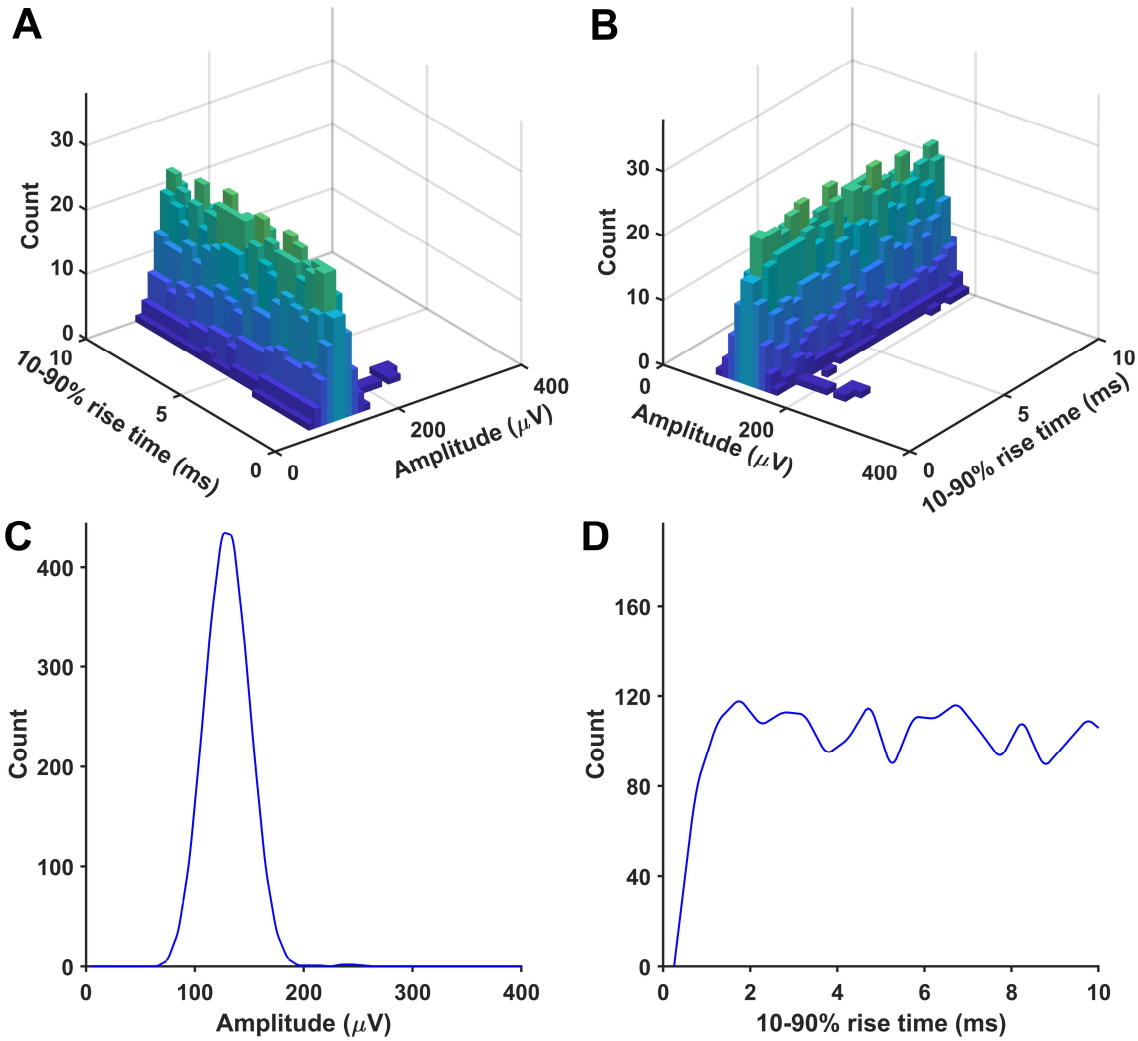

Supplementary figure 32: An example of simulated minis distribution that was used to produce a close match between distributions of detected minis-like events in a 'noise with simulated minis' voltage trace and in a 'noise with real minis' recording for a cell p120b of cortical layer 2/3. The meaning of different figure panels is explained in Supplementary figure 27.

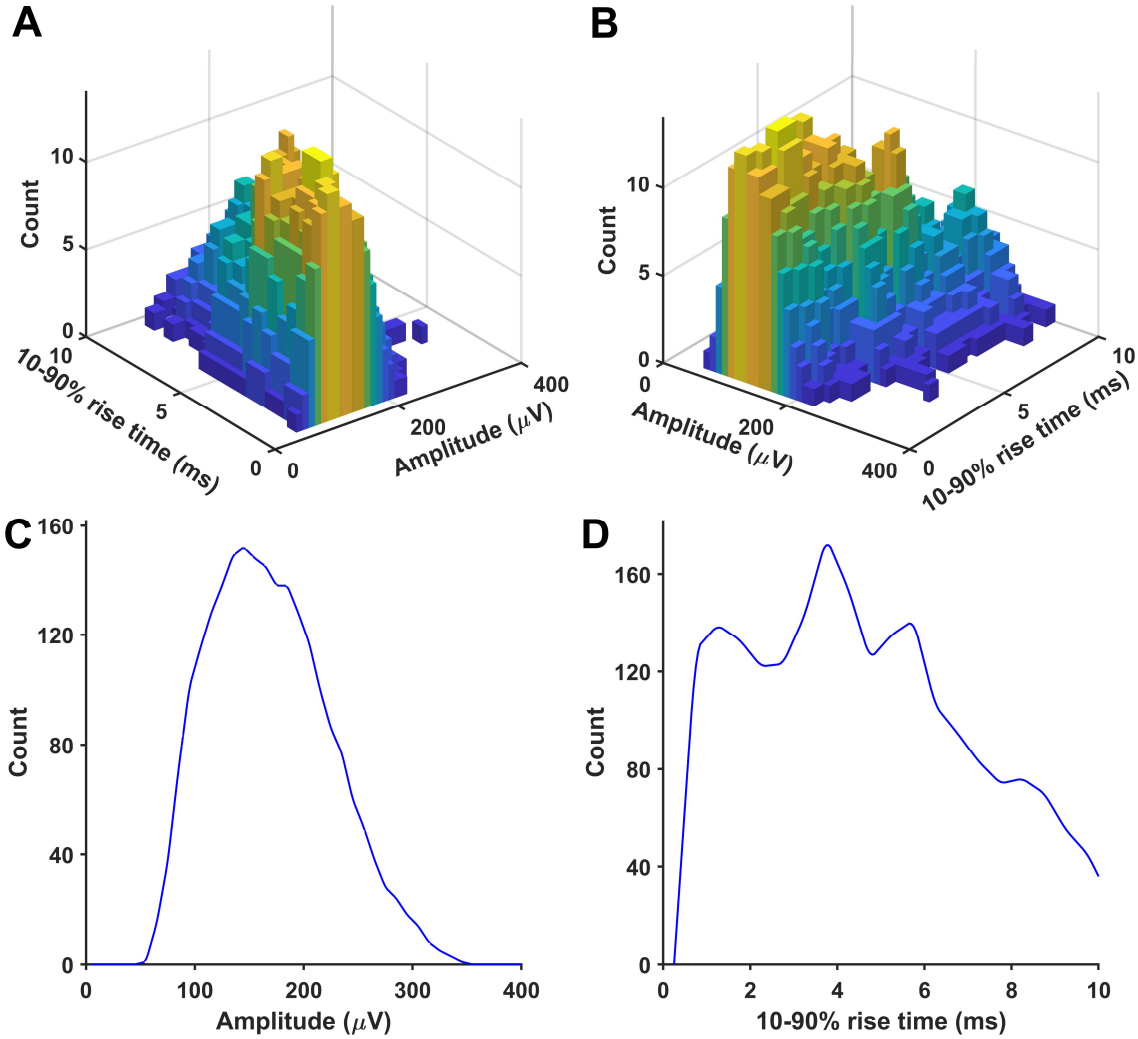

Supplementary figure 33: An example of simulated minis distribution that was used to produce a close match between distributions of detected minis-like events in a 'noise with simulated minis' voltage trace and in a 'noise with real minis' recording for a cell p122a of cortical layer 2/3. The meaning of different figure panels is explained in Supplementary figure 27.

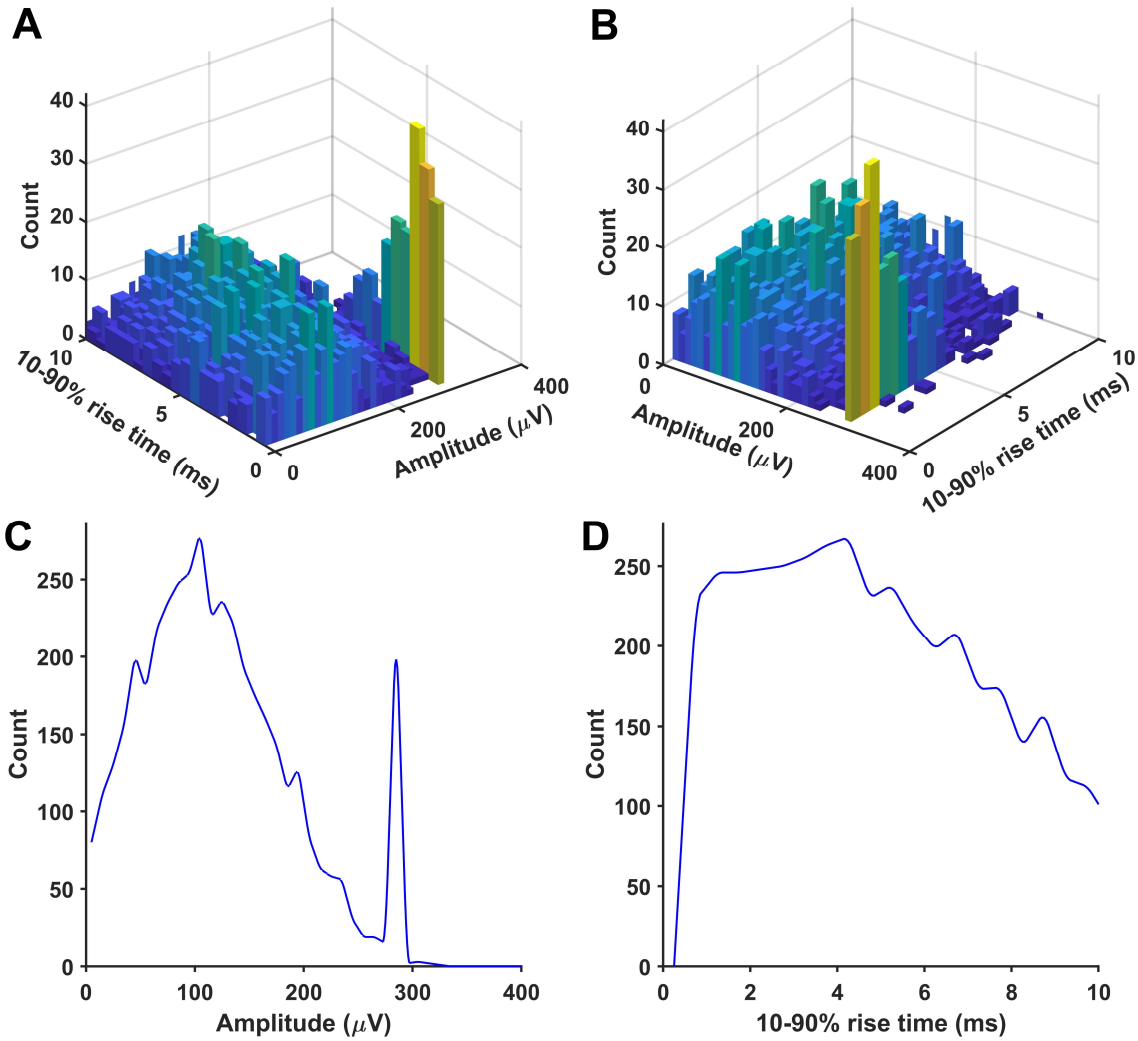

Supplementary figure 34: An example of simulated minis distribution that was used to produce a close match between distributions of detected minis-like events in a 'noise with simulated minis' voltage trace and in a 'noise with real minis' recording for a cell p124b of cortical layer 5. The meaning of different figure panels is explained in Supplementary figure 27.

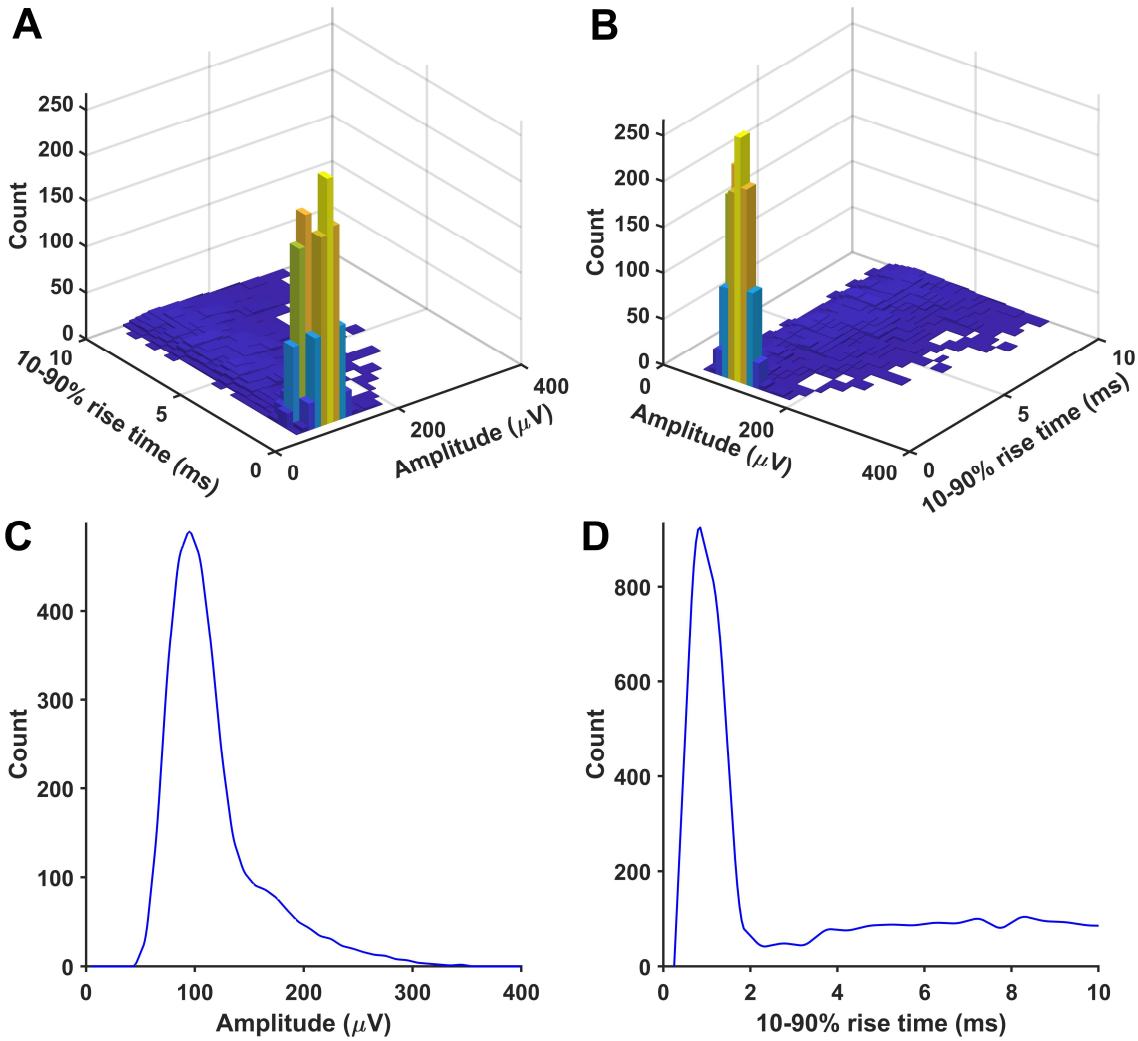

Supplementary figure 35: An example of simulated minis distribution that was used to produce a close match between distributions of detected minis-like events in a 'noise with simulated minis' voltage trace and in a 'noise with real minis' recording for a cell p125a of cortical layer 2/3. The meaning of different figure panels is explained in Supplementary figure 27.

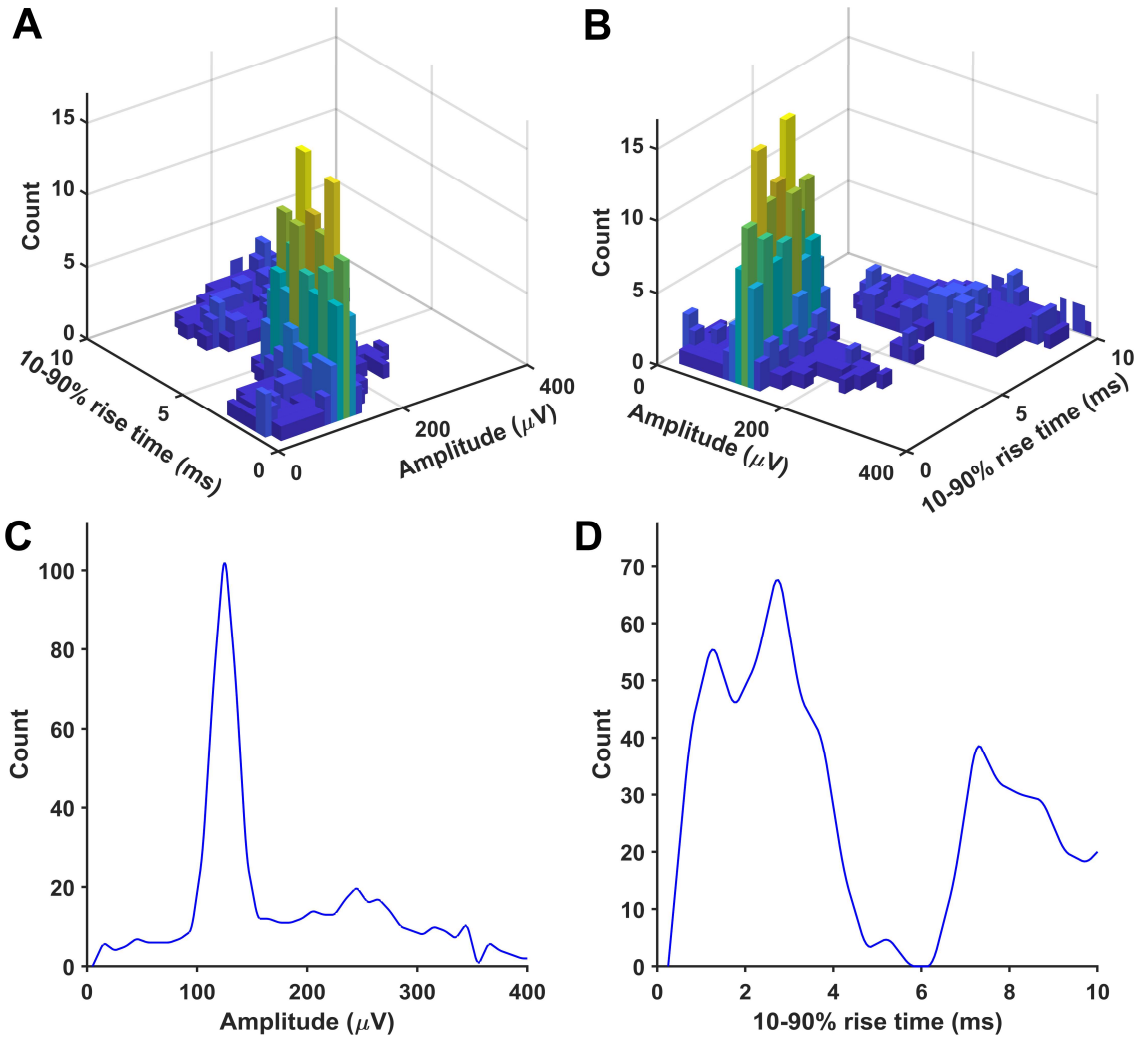

Supplementary figure 36: An example of simulated minis distribution that was used to produce a close match between distributions of detected minis-like events in a 'noise with simulated minis' voltage trace and in a 'noise with real minis' recording for a cell p127c of cortical layer 2/3. The meaning of different figure panels is explained in Supplementary figure 27.

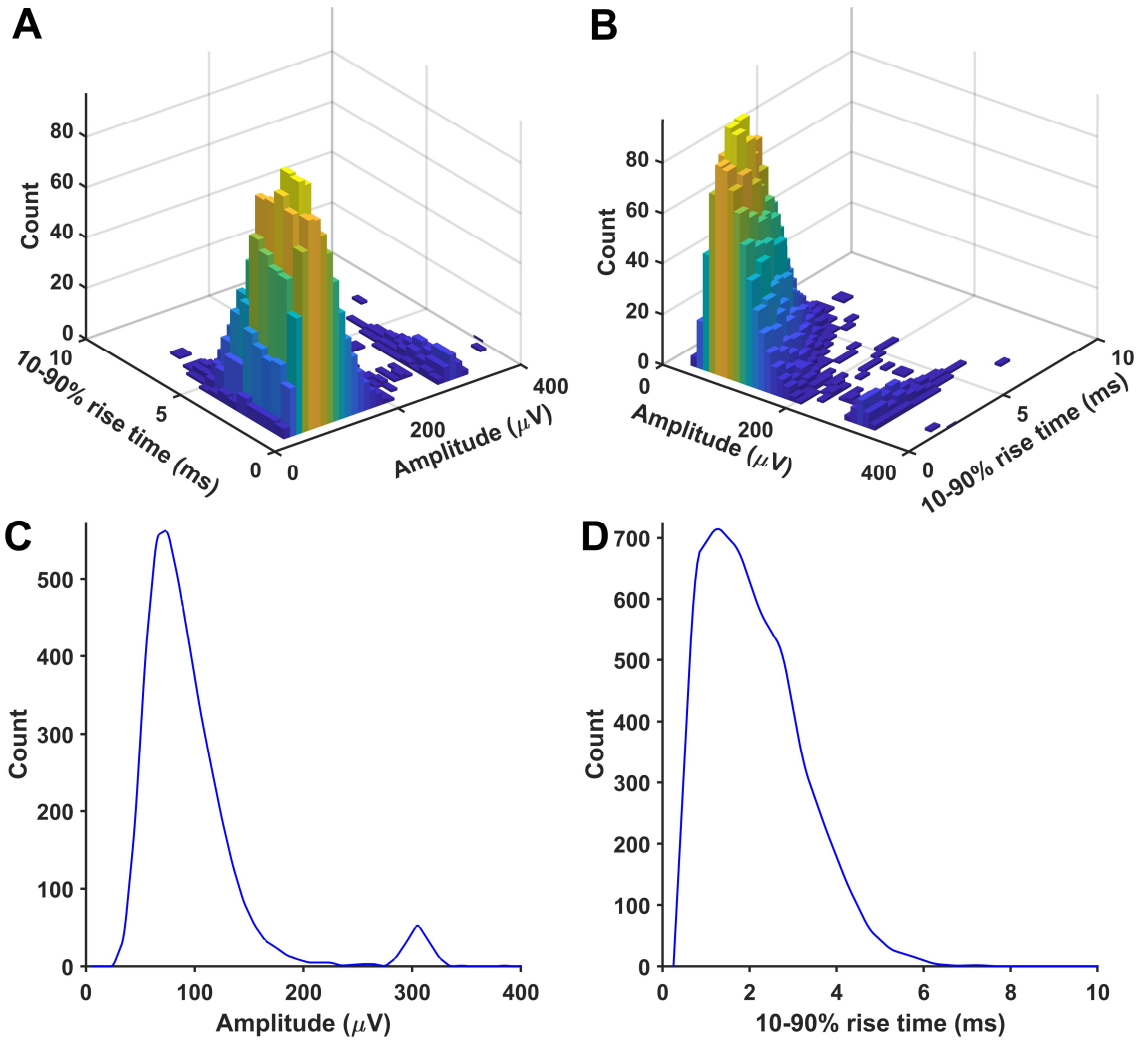

Supplementary figure 37: An example of simulated minis distribution that was used to produce a close match between distributions of detected minis-like events in a 'noise with simulated minis' voltage trace and in a 'noise with real minis' recording for a cell p128c of cortical layer 2/3. The meaning of different figure panels is explained in Supplementary figure 27.

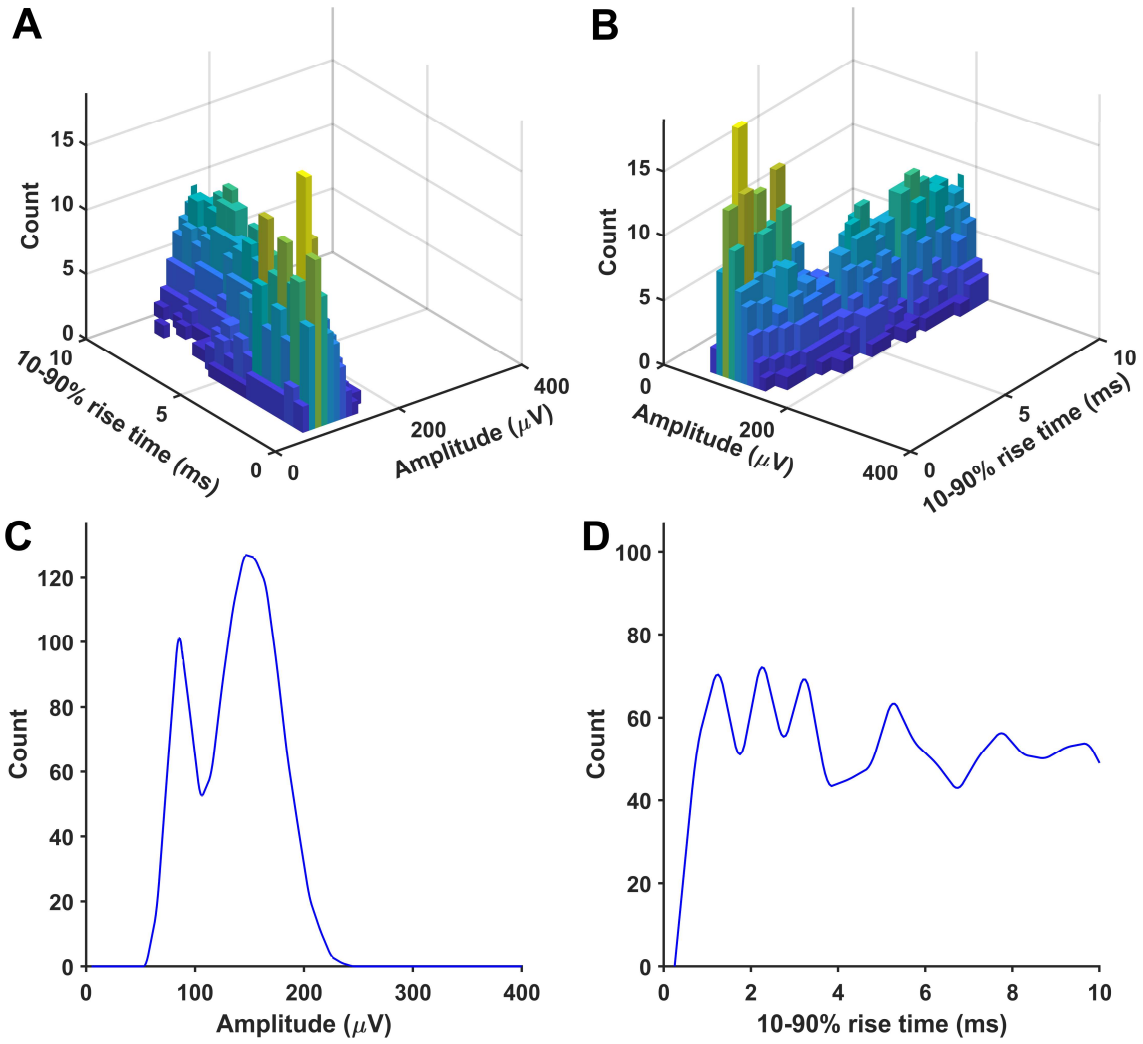

Supplementary figure 38: An example of simulated minis distribution that was used to produce a close match between distributions of detected minis-like events in a 'noise with simulated minis' voltage trace and in a 'noise with real minis' recording for a cell p129a of cortical layer 5. The meaning of different figure panels is explained in Supplementary figure 27.

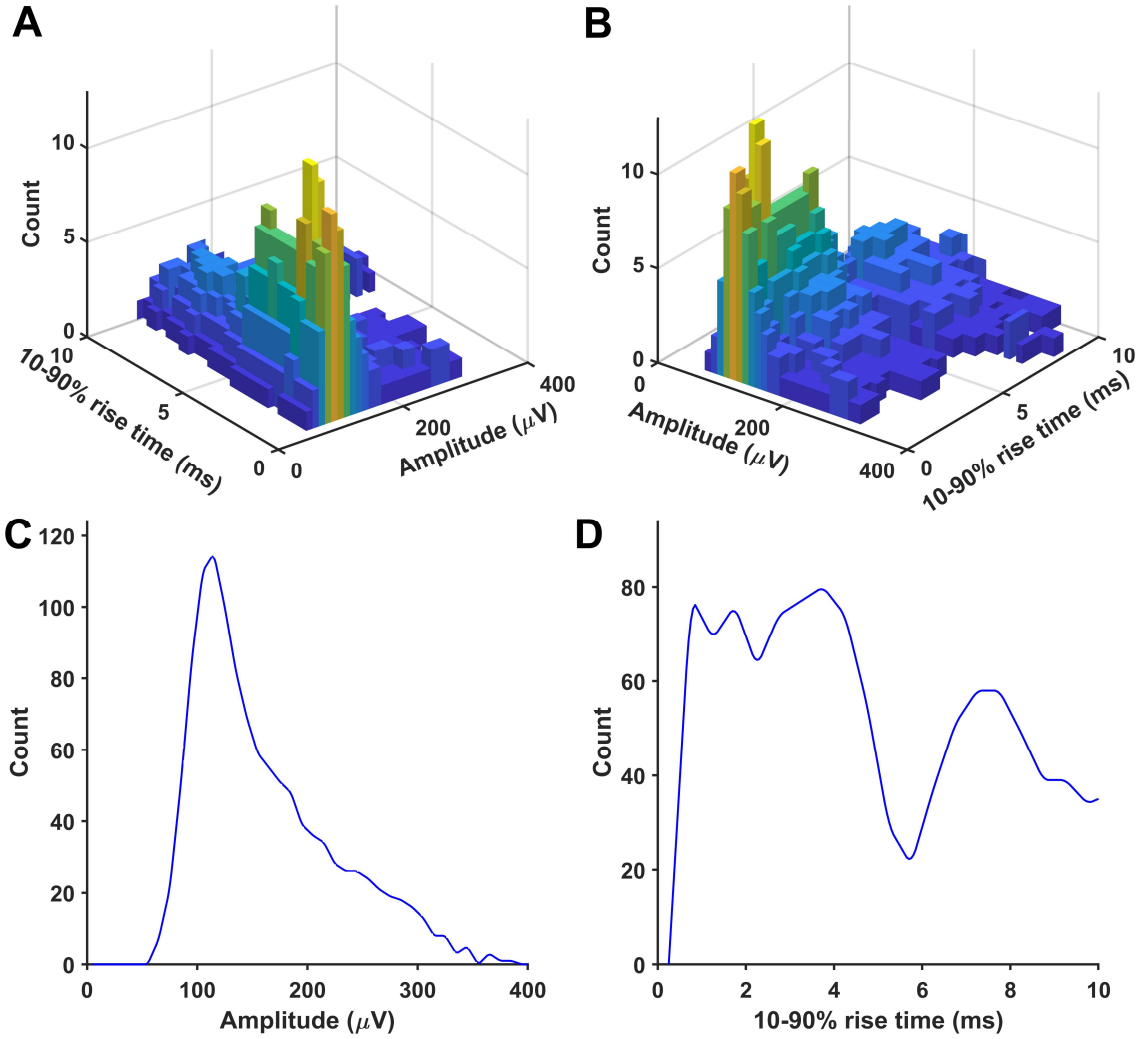

Supplementary figure 39: An example of simulated minis distribution that was used to produce a close match between distributions of detected minis-like events in a 'noise with simulated minis' voltage trace and in a 'noise with real minis' recording for a cell p131a of cortical layer 2/3. The meaning of different figure panels is explained in Supplementary figure 27.